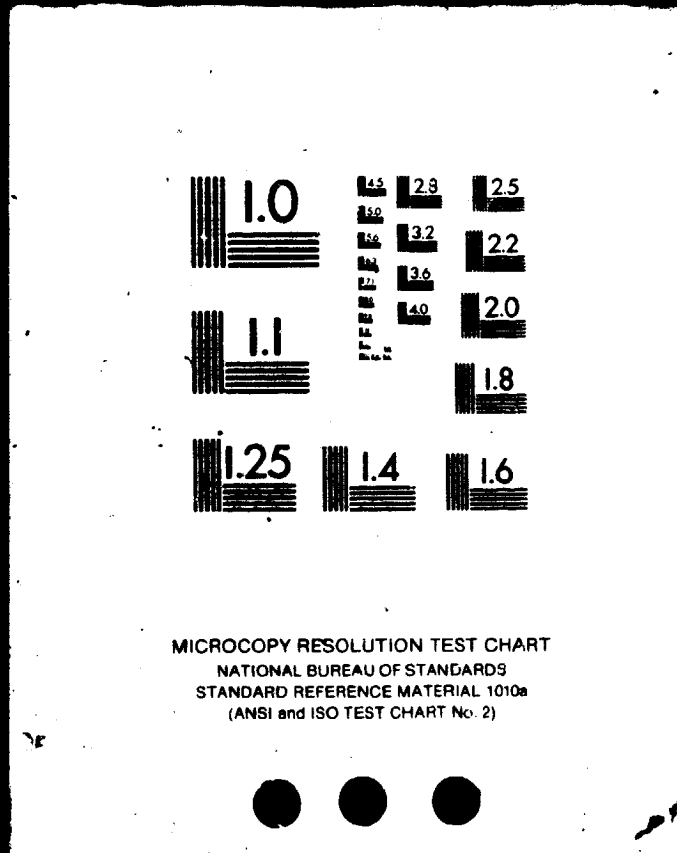


1 OF 2

N86-27186

UNCLAS



9184

9-11-84

9985 149 pages

NASA Contractor Report 174758

Experimental and Analytical Investigation of a Freezing Point Depressant Fluid Ice Protection System

Alan E. Albright

University of Kansas  
Lawrence, Kansas

KF 651154

(NASA-CR-174758) EXPERIMENTAL AND  
ANALYTICAL INVESTIGATION OF A FREEZING POINT  
DEPRESSANT FLUID ICE PROTECTION SYSTEM M.S.  
Thesis. Final Report (Kansas Univ.) 149 p  
HC A07/MF A01

N86-27186

Unclas  
43121

CSC 01A G3/02

September 1984

Prepared for

NATIONAL AERONAUTICS AND SPACE ADMINISTRATION  
Lewis Research Center  
Under Grant NAG 3-273

## Table of Contents

	<u>Page</u>
List of Symbols . . . . .	iii
1.0 Introduction . . . . .	1
2.0 Description of Test Facilities and Equipment . . . . .	3
2.1 Icing Research Tunnel . . . . .	3
2.2 Wing Models . . . . .	6
2.3 Ice Protection System . . . . .	12
2.3.1 System Description . . . . .	12
2.3.2 Porous Leading Edge Panels . . . . .	13
2.3.2.1 Stainless Steel Mesh Panel . . . . .	14
2.3.2.2 Drilled Titanium Panel . . . . .	15
2.3.2.3 Composite Panel . . . . .	15
2.3.3 Freezing Point Depressant Solutions . . . . .	21
2.3.4 Fluid Supply Pump . . . . .	23
3.0 Test Techniques . . . . .	28
3.1 Tunnel Conditions . . . . .	28
3.2 Test Procedures and Method of Analysis . . . . .	34
3.2.1 Aerodynamic . . . . .	34
3.2.2 Anti-ice . . . . .	35
3.2.3 Deice . . . . .	37
4.0 Test Results and Discussions . . . . .	38
4.1 Aerodynamic . . . . .	38

4.2	Anti-ice . . . . .	58
4.2.1	Stainless Steel Mesh Panel . . . . .	61
4.2.2	Titanium Panel . . . . .	77
4.2.3	Composite Panel . . . . .	85
4.3	Deice . . . . .	86
4.4	Fluid Type Analysis . . . . .	91
5.0	Anti-ice Flow Rate Prediction Techniques . . . . .	92
5.1	ADS-4 Method . . . . .	92
5.2	Analytical Method . . . . .	97
5.3	Comparison with Experimental Data . . . . .	100
5.4	Sensitivity Analysis . . . . .	110
6.0	General Comments . . . . .	110
7.0	Conclusions . . . . .	113
8.0	Recommendations . . . . .	114
9.0	References . . . . .	116
	Appendix . . . . .	118
A.	Summary of Anti-Ice Wind Tunnel Results . . . . .	118
B.	Averaged Experimental and Predicted Anti-Ice Fluid Flow Rates . . . . .	128
C.	Water Droplet Impingement Efficiency Distributions . . . . .	132
D.	Computer Program Listing of Prediction Methods . . . . .	140

### List of Symbols

c	wing chord length, ft
$c_d$	section drag coefficient, dimensionless
$c_{do}$	clean wing drag coefficient, dimensionless
d	volume median water droplet diameter, microns
$E_m$	overall collection efficiency, dimensionless
G	glycol plus propanol mass fraction of final mixture, percent
h/c	ratio of projected airfoil height to chord, dimensionless
LWC	liquid water content, $g/m^3$
$M_w$	water catch rate on wing surface, $g/min\ cm^2$
S	final position of droplet trajectory, dimensionless
$S_u$	tangent trajectory impingement limit on upper surface, dimensionless
$S_l$	tangent trajectory impingement limit on lower surface, dimensionless
SFF	anti-ice specific fluid flow, $g/min\ cm^2$
$SFF_1$	anti-ice <sub>2</sub> specific fluid flow judged by observer 1, $g/min\ cm^2$
$SFF_2$	anti-ice <sub>2</sub> specific fluid flow judged by observer 2, $g/min\ cm^2$
$SFF_a$	analytically predicted fluid flow, $g/min\ cm^2$
$SFF_e$	ADS-4 predicted fluid flow, $g/min\ cm^2$
$SFF_x$	anti-ice <sub>2</sub> specific fluid flow using the AL5 fluid, $g/min\ cm^2$
$SFF_y$	anti-ice <sub>2</sub> specific fluid flow using the TKS80 fluid, $g/min\ cm^2$
T	total temperature, degrees F

$T_f$  glycol-water mixture freezing temperature, degrees F  
 $T_{ok}$  datum temperature, degrees F  
 $V$  free stream equivalent airspeed, knots  
 $WS$  wing station, inch  
 $X$  glycol plus propanol mass fraction of original mixture  
 $x,y$  airfoil position coordinate  
 $Y$  starting position of droplet trajectory, dimensionless  
 $\alpha$  angle of attack, degrees  
 $\beta$  local impingement efficiency, dimensionless  
 $\beta_{max}$  maximum local impingement efficiency, dimensionless

## 1.0 Introduction

During the past few years there has been an increasing interest in the effectiveness and efficiency of ice protection systems. To address these concerns, a grant from NASA Lewis Research Center (NASA LeRC) was awarded to the University of Kansas in May of 1980 entitled "An Assessment of General Aviation Deicing Systems on Contemporary Airfoils." Two ice protection systems were evaluated on two general aviation wing sections over a period of two years as part of this grant. The inflatable tube pneumatic boot was one of these systems. The second system, originated in England in the 1940s, was the fluid ice protection system. This system incorporates a porous leading edge panel through which a glycol-water solution exudes on to the wing to lower the freezing temperature of the resulting mixture with the impacting water. The results of the fluid system evaluation are presented in ref. 1.

As a result of these tests, the fluid ice protection system has rapidly increased in popularity with U.S. aircraft manufacturers. Today, for example, the Cessna Citation IISP is flying with the system as factory installed equipment. Beechcraft's Starship I and the Old Man's Aircraft Company OMAC-I will also be offering the system as standard equipment. Flight test and certification are now underway for a Supplemental Type Certificate (STC) on the Cessna 206. In Great Britain, the Beech Duchess, Piper Seminole, and the

Grumman American Cougar have already been approved for flight in known icing conditions with a fluid system. Tests are now underway in Great Britain for approval of the fluid system on the Beech Baron and the Partenavia P-68B.

With the increasing popularity of the fluid ice protection system, it has become necessary to establish a broad data base of anti-ice flow rates for a variety of icing conditions, wing sections, and types of porous panels. Also, there is a need for a verified method of predicting anti-icing flow rates. Such a method would reduce the necessity of expensive wind tunnel tests and would be a valuable tool for the airplane designer.

The research presented in this report was supported in full by a follow-on grant from NASA LeRC to the University of Kansas entitled "A Joint KU/NASA Graduate Research Study." The objectives of this research effort are as follows: first, to increase the experimental data base of minimum required anti-icing flow rates throughout a broad range of icing conditions on two different general aviation airfoils; second, to test the validity and reliability of two methods of predicting anti-ice flow rates; third, to test a new laser drilled titanium porous panel; and finally, to evaluate a composite porous panel.

This report is presented in four sections. The first section presents the test facility, test conditions, and the test procedures used. The second section is a brief discussion of the aerodynamic

effects associated with ice accretions. The third section presents the anti-ice flow rates obtained through wind tunnel tests in the NASA LeRC Icing Research Wind Tunnel. The final section is a presentation of the prediction methods, and a comparison between the predicted and actual flow rates.

## 2.0 Description of Test Facilities and Equipment

### 2.1 Icing Research Tunnel

The NASA Lewis Icing Research Tunnel (IRT) is a closed cycle, refrigerated wind tunnel with a rectangular test section 1.83m (6 ft) high by 2.74 m (9 ft) wide by 6.1 m (20 ft) long (Fig. 2.1). Maximum tunnel airspeed is approximately 134 m/s (300 mph). A natural icing cloud is simulated by injecting a water spray upstream of the test section from a multi-nozzle spray bar system.

The area of interest on a test model is confined to the region in the center of the test section, where the icing cloud is most uniform, covering a cross-sectional area of approximately 0.9 m (3 ft) high by 1.5 m (5 ft) wide. The liquid water content (LWC) of the cloud can be varied from about 0.5 to 2.4 g/m<sup>3</sup> with volume median droplet diameters (d) in the range from 10 to 20 microns. The tunnel total air temperature can be regulated from ambient to below -28.9 degrees C (-20 degrees F).

From outside the tunnel test section, steam and electrically heated windows allow visual observation and documentation of the test while in progress. Between icing sprays, tunnel operators and engineering test personnel, appropriately dressed with cold weather gear, are able to enter the tunnel test section. This access to the test model permits manual cleaning of ice and frost off the wing model, documentation of ice shapes, close-up photography, and modifications to the test model.

A translating wake-survey probe was used to measure the section drag coefficient,  $c_d$ , of the test model. The probe, which had a stagnation and static pressure orifice, could be retracted behind a wind screen. When the airfoil was exposed to the tunnel icing cloud, the probe was retracted. After the icing cloud was turned off, the probe was inserted into the airstream and the translating drag survey was made. The probe was located about one chord length downstream of the airfoil at midspan.

ORIGINAL PAGE IS  
OF POOR QUALITY

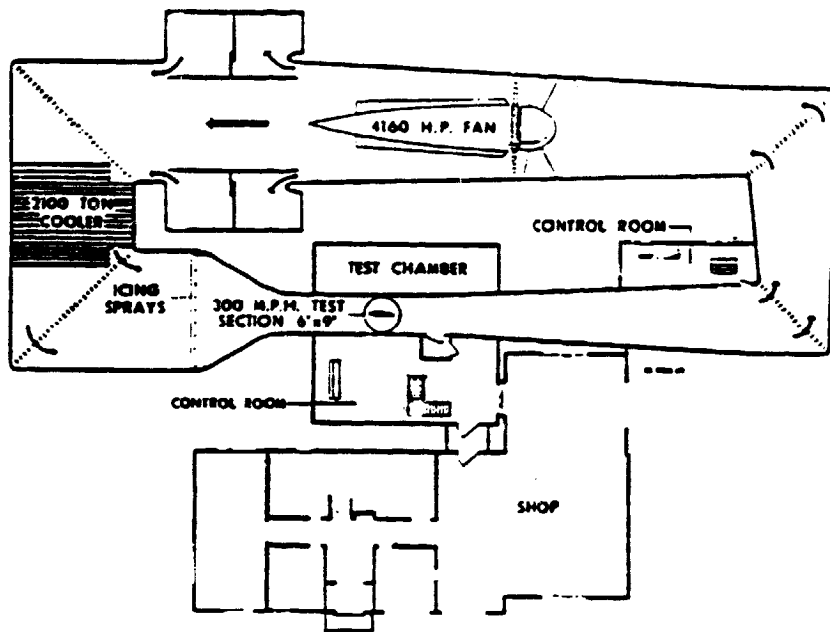


Figure 2.1. - Schematic Planform of Icing Research Tunnel.

## 2.2 Wing Models

This report contains results and analysis of tests conducted on two different general aviation wing models, designated as Wing Model A and Wing Model B. These wing models, having different airfoil sections, were tested independently. Results and conclusions obtained on one wing model cannot be generalized to other wings.

Wing Model A was an inboard section of a full scale wing taken from a single engine general aviation aircraft. The wing model had a constant chord length of 1.63 m (64.0 in) and a modified leading edge NACA 2412 airfoil as depicted in Fig. 2.2. Table I presents the coordinates for the airfoil. The model was not twisted or swept. The wing model was fastened to the tunnel floor turntable through brackets bolted to the primary internal wing structure. It was supported at the ceiling through a pivot. A clearance of 1/2 inch was allowed between the model and the ceiling of the 6 foot high test section.

Wing Model B also was a full scale wing taken from a single engine general aviation airplane. The original wing tapered from a NACA 64<sub>2</sub>A215 airfoil at the root (WS 0) to a NACA 64<sub>1</sub>A412 airfoil at the tip (WS 216). The wing incorporated a leading edge modification designed by Raymond Hicks (ref. 2,3). This modification increases the maximum lift coefficient and the lift/drag ratio. The thickness over the forward 30 percent of the upper surface and the leading

edge radius is increased as shown in Figure 2.3 on a NACA 64<sub>1</sub>A412 airfoil.

The wing section was fastened to the tunnel floor turntable using the spar fittings that are designed to attach the wing to the fuselage of the airplane. The centerline of the tunnel was at WS 58 of the original wing. Table II gives the airfoil coordinates at WS 58, where the chord is 1.61 m (63.25 in). The chord tapered 1.1 inches per foot of span, and the wing was twisted 0.167 degrees per foot of span (washout). Figure 2.4 shows Wing Model B in the IRT test section.

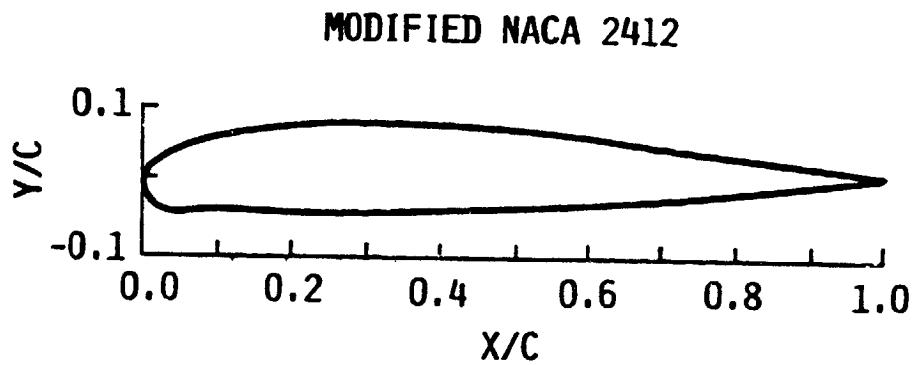


Figure 2.2. - Airfoil Section of Wing Model A

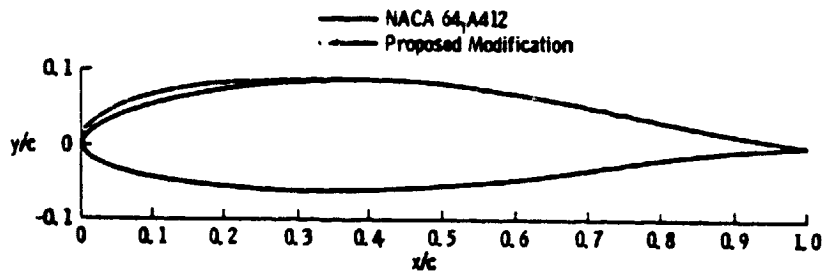


Figure 2.3. - Hicks Modification on a NACA 64, A412 Airfoil

Table I : Airfoil Coordinates of Wing Model A in  
Percent of Chord.

Upper Surface		Lower Surface	
%X/C	%Y/C	%X/C	%Y/C
----	----	----	----
0.00	0.00	0.00	0.00
1.25	2.03	1.25	-3.44
2.50	2.93	2.50	-4.06
5.00	4.06	5.00	-4.06
7.50	4.97	7.50	-4.02
10.00	5.64	10.00	-4.00
15.00	6.55	15.00	-4.06
20.00	7.36	20.00	-4.29
25.00	7.71	25.00	4.29
30.00	7.72	30.00	-4.18
40.00	7.90	40.00	-3.84
50.00	7.38	50.00	-3.39
60.00	6.41	60.00	-2.91
70.00	5.24	70.00	-2.23
80.00	4.02	80.00	-1.17
90.00	2.71	90.00	.09
95.00	2.08	95.00	.72
100.00	1.35	100.00	1.35

Table II : Airfoil Coordinates of Wing Model B at Centerline  
of Tunnel (WS 58) in Percent of Chord.

Upper Surface		Lower Surface	
%X/C	%Y/C	%X/C	%Y/C
----	----	----	----
.000	- .704	.000	- .704
.015	- .250	.335	-1.474
.648	.791	.723	-1.858
1.138	2.372	1.216	-2.193
2.055	3.477	2.451	-2.760
3.953	4.941	4.926	-3.545
6.324	6.008	7.407	-4.130
9.486	6.735	14.223	-5.371
11.352	7.036	19.197	-5.395
13.439	7.502	24.175	-6.359
22.024	7.565	29.157	-6.658
24.996	7.581	34.142	-6.816
30.126	7.597	39.129	-6.870
34.783	7.543	44.122	-6.718
39.428	7.426	49.115	-6.449
44.409	7.110	54.111	-6.114
49.387	6.591	99.741	-2.794
54.360	5.891		
59.331	5.047		
62.111	4.526		
99.744	-2.606		

ORIGINAL PAGE IS  
OF POOR QUALITY

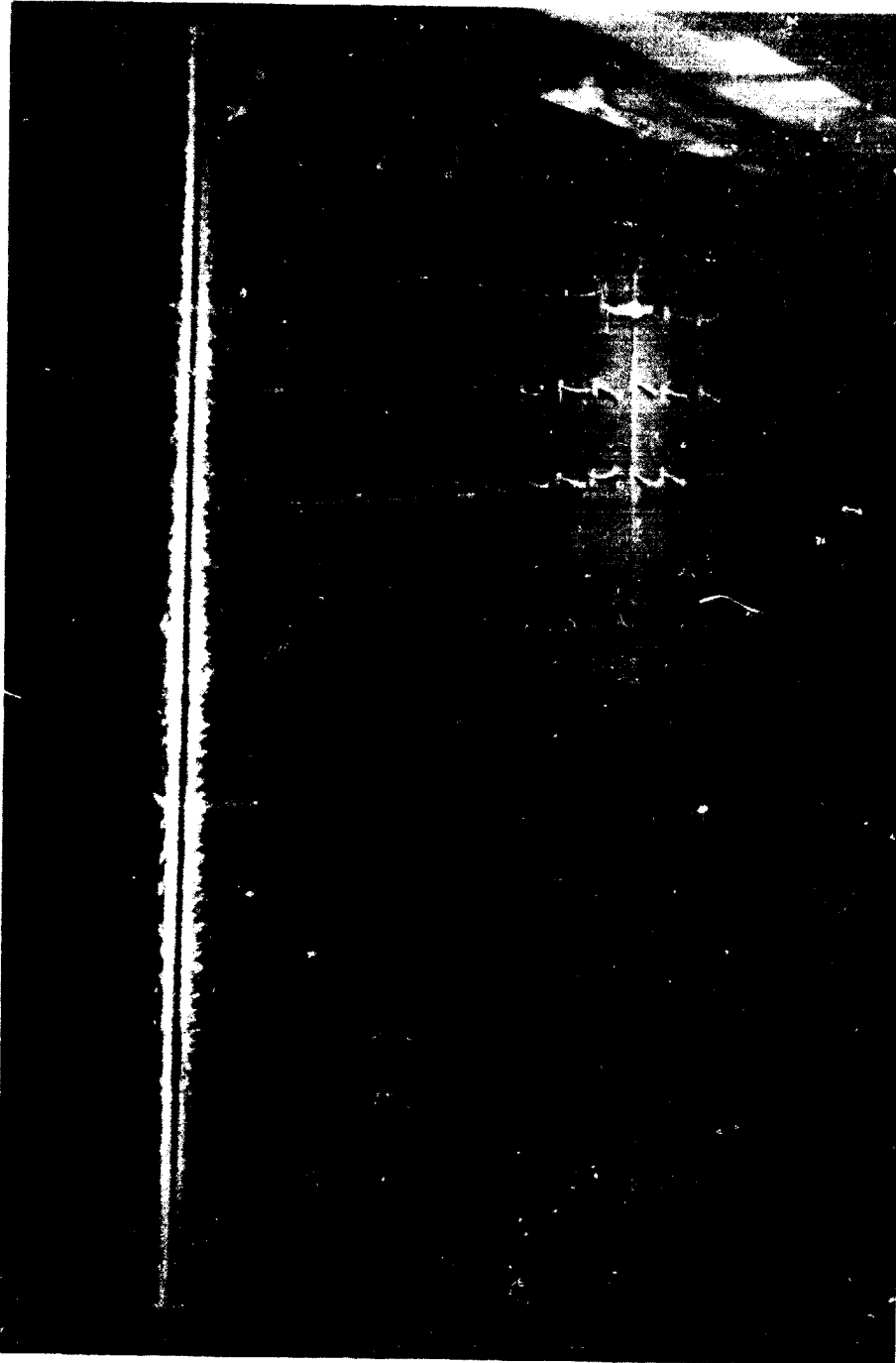


Figure 2.4. - Wing Model B Installed in Tunnel Test Section.

## 2.3 Ice Protection System

### 2.3.1 System Description

The fluid ice protection system tested consists of a porous panel attached to the leading edge of a wing, and a pumping system that distributes a glycol based freezing point depressant fluid from a tank to the panel. The rate of fluid exuding from the porous panel onto the surface of the wing and the severity of the icing encounter determines the type of ice protection possible. The system is capable of anti-icing by creating a mixture of the glycol fluid with the impacting water with a freezing temperature below the local temperature to prevent the formation of ice on the leading edge. The system is also capable of deicing by dissolving the bond between the accreted ice and the panel skin until aerodynamic forces carry the ice accretion downstream.

Most ice protection systems operate in either an anti-ice, or a deice mode. However, the fluid ice protection system is capable of operating in, what is often referred to as the natural-deice mode. In this mode the flow of glycol is lower than the anti-ice flow rate, but still high enough that no permanent ice accretions form on the wing leading edge. In the natural-deice cycle, temporary ice accretions ranging from small ice patches to narrow bars form near the stagnation point, before being carried downstream after several

seconds to a few minutes. This build-shed cycle then repeats, without forming any permanent accretions of ice.

A benefit of the fluid ice protection system is the runback of the glycol solution onto the upper and lower wing surfaces behind the leading edge panel. This runback is often sufficient to prevent, or remove, the formation of any aft frost which might exist on the wing surfaces.

### 2.3.2 Porous Leading Edge Panels

Three types of porous leading edge panels were tested; stainless steel mesh, laser drilled titanium, and composite. The stainless steel type panels were tested on both wing models. The titanium panel was tested only on Wing Model A. The composite panel was tested only on Wing Model B. The stainless steel and composite panels were riveted onto the original wing leading edge skin. The titanium panel was attached with countersunk screws. Each of the panels tested were divided into three independent sections into which the flow rate of glycol could be controlled independently.

### 2.3.2.1 Stainless Steel Mesh Panel

The stainless steel mesh panel consisted of two layers of wire cloth that were rolled, sintered, and then finish-rolled. The wire cloth was manufactured from an 18-8 austenitic stainless steel and nominally has 110 by 20 wires per inch. The two layers of wire cloth are laid 90 degrees with respect to each other. Figures 2.5 a-c show a front view, back view, and a close-up view of the stainless steel mesh panel.

Inside the fluid reservoir, behind the stainless steel mesh skin, is a thin polyvinylchloride sheet. The purpose of this material, whose porosity is much lower than that of the stainless steel, is to increase the pressure in the reservoir sufficiently to distribute the glycol evenly over the entire active portion of the panel, regardless of the chordwise pressure distribution, which changes with angle of attack.

The maximum thickness of the leading edge panel was 3.2 mm. The panel contoured to Wing Model A section had an active porous width of 6.9 cm. The length of the inboard and outboard sections was 29.2 cm long, and the middle section was 40.6 cm long. The panel installed on Wing Model B had an active width of 8.7 cm, with the outboard and inboard sections 29.2 cm long, and the middle section 40.6 cm long.

#### 2.3.2.2 Drilled Titanium Panel

The titanium panel is similar to the stainless steel panel except for a laser drilled titanium outer skin perforated with microscopic holes through which the glycol fluid passes. The holes are nominally .0025 inches in diameter, with .035 inch separation between centers. This yields approximately 800 holes per square inch. The panel had an active width of 7.6 cm. The inboard and outboard sections were 29.9 cm long, and the middle section was 41.3 cm long. Figures 6 a and b show a back view and a side view of the drilled titanium panel tested on Wing Model A.

#### 2.3.2.3 Composite Panel

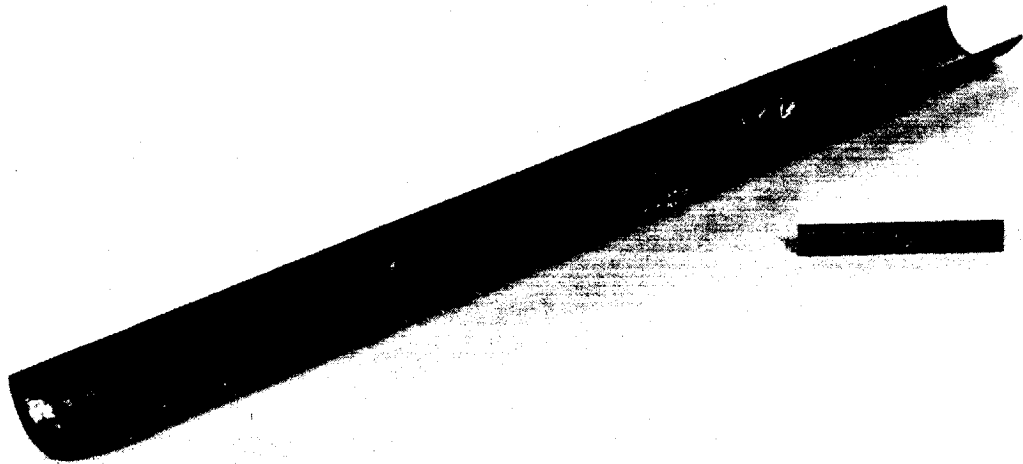
The porous composite panel, tested only on Wing Model B, had an outer skin made with a resin starved matrix laminate with successive layers of Kevlar49 - 3D woven Eglass - Kevlar49. Inside the fluid cavity were layers of polyvinyl fluoride, which is intended to distribute the flow of glycol uniformly chordwise regardless of the pressure distribution changes that occur as angle of attack changes. The original panel tested in 1981 (ref. 4) contained only 1 layer of the polyvinyl fluoride material. The second composite panel, discussed in this report, contained an additional layer of this filter material. The backing plate was constructed of an ordinary

boat glass epoxy layup. The width of the porous region was 8.7 cm. The inboard and outboard section were 29.2 cm long and the middle section was 40.6 cm long. The maximum thickness of the panel was 3.2 mm. Figures 2.7 a and b show the front view and back view of one of the three sections of the composite panel. The front view illustrates the distribution of fluid exuding out of the panel during a static test.

ORIGINAL PAGE IS  
OF POOR QUALITY

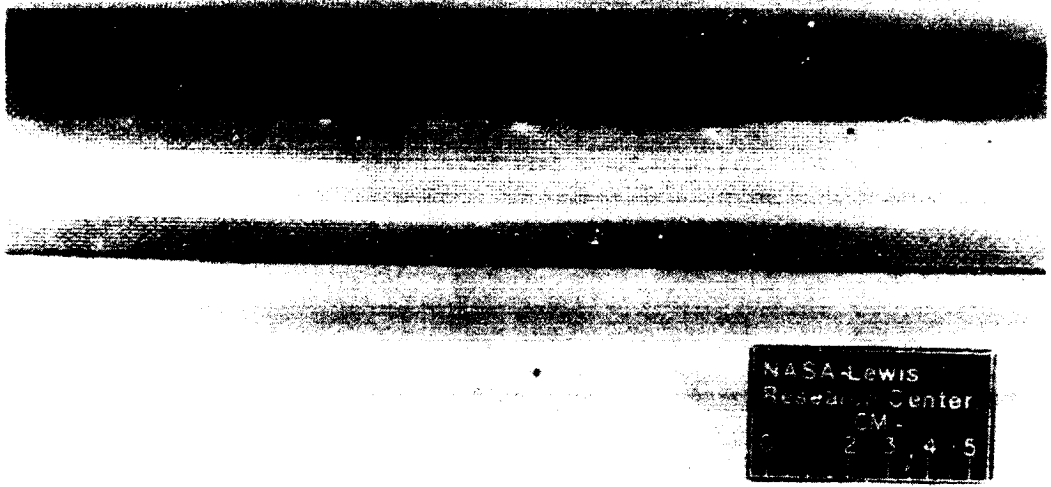


(a) Front View



(b) Back View

Figure 2.5. - Stainless Steel Mesh Porous Leading Edge Panel.



(c) Close Up

Figure 2.5. (Continued.)



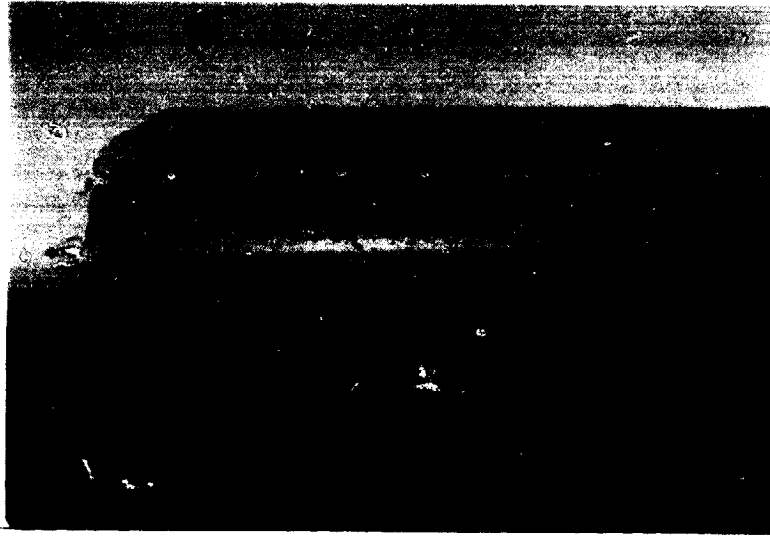
CECIMA, J. M. T. (1980) [Illegible]

(a) Back View

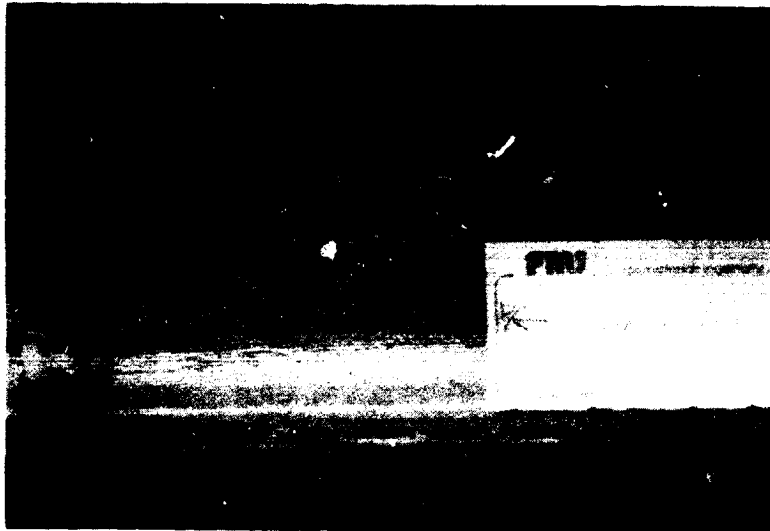


(b) Side View

Figure 2.6. - Drilled Titanium Porous Leading Edge Panel.



(a) Front View



(b) Back View

Figure 2.7. - Composite Porous Leading Edge Panel.

### 2.3.3 Freezing Point Depressant Solutions

Two glycol based fluids were used during the tests presented in this report. The first fluid's composition (TKS80), as determined by the NASA Lewis Chemical Laboratory, was 18.8% de-ionized water and 81.2% mono-ethylene glycol. The second fluid's composition (AL5) was determined to be 12.2% de-ionized water, 3.1% isopropanol, and 84.7% mono-ethylene glycol. Both fluids have specific gravities of  $1.09 \text{ g/cm}^3$ .

The tests reported in reference 1 were conducted using only the TKS80 fluid. All the tests presented in this report used the AL5 fluid. In addition, the TKS80 fluid was used during the stainless steel panel test on Wing Model A to determine any differences in performance between the two fluids. Figure 2.8 presents the freezing temperatures ( $T_f$ ) of the solutions as they are diluted with water. The temperatures are plotted against the mass fraction of glycol plus propanol, G, in the mixture. At mass fractions between approximately 65 and 80 percent the mixture turns to a gel instead of a solid as it is chilled.

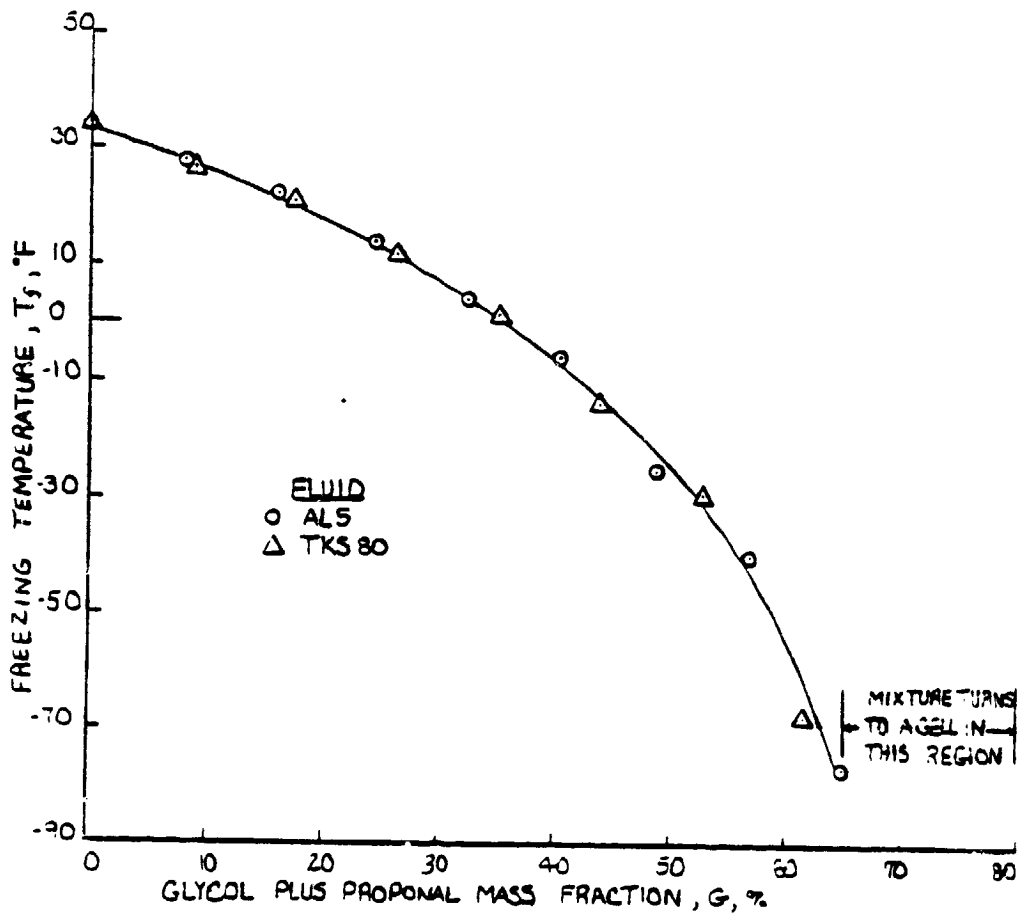


Figure 2.8. - Freezing Temperature Profile of Two Glycol - Water Solutions.

#### 2.3.4 Fluid Supply Pump

The flow rate to each of the three sections of a porous leading edge panel was controlled and metered independently by a flight-worthy pumping system with three variable positive displacement pumps. The overall pumping package as shown in the schematic of Figure 2.9 consisted of a transfer pump, fluid filter, air filter, fluid tank, control panel (not shown), and the main metering pump. Figure 2.10 shows the actual pump system apparatus used during the wind tunnel tests.

The main fluid tank is filled using a transfer pump which pumps the fluid from the original container through a filter and into the tank. The tank outlet is connected to a small air filter to prevent the ingress of dirt. A float type contents transmitter is installed in the tank. The control panel provides control of and indicates all pump functions along with an indication of the level of fluid in the tank.

The main metering pump consists of three separate pumping cells, driven by a 28 volt DC motor through a toothed belt reduction drive train. Each cell consisted of a piston actuated by an eccentric cam. A stroke limiting device, connected to a digital position readout is used to provide an adjustable flow rate. Pressure relief valves, bolted on the outlet of each cell, are set to open at approximately 95 lbs/sq. inch to protect the porous panel from exces-

sive pressures. A solenoid valve connected to each pump cell provides a means of selectively turning each outlet on or off as required.

The fluid ice protection system, including the stainless steel and titanium panels, TKS80 fluid, and the pumping system were developed and manufactured by T.K.S. (Aircraft De-Icing) Limited, of Great Britain. The North American representative of T.K.S. is Kohlman Aviation Corporation in Lawrence, Kansas. The composite porous panel was developed and manufactured by Fiber Materials Incorporated in Biddeford, Maine. The ALS fluid, marketed in the United States and approved for use by T.K.S., was supplied by Canyon Industries of Phoenix, Arizona.

# FLUID CIRCUIT SCHEMATIC

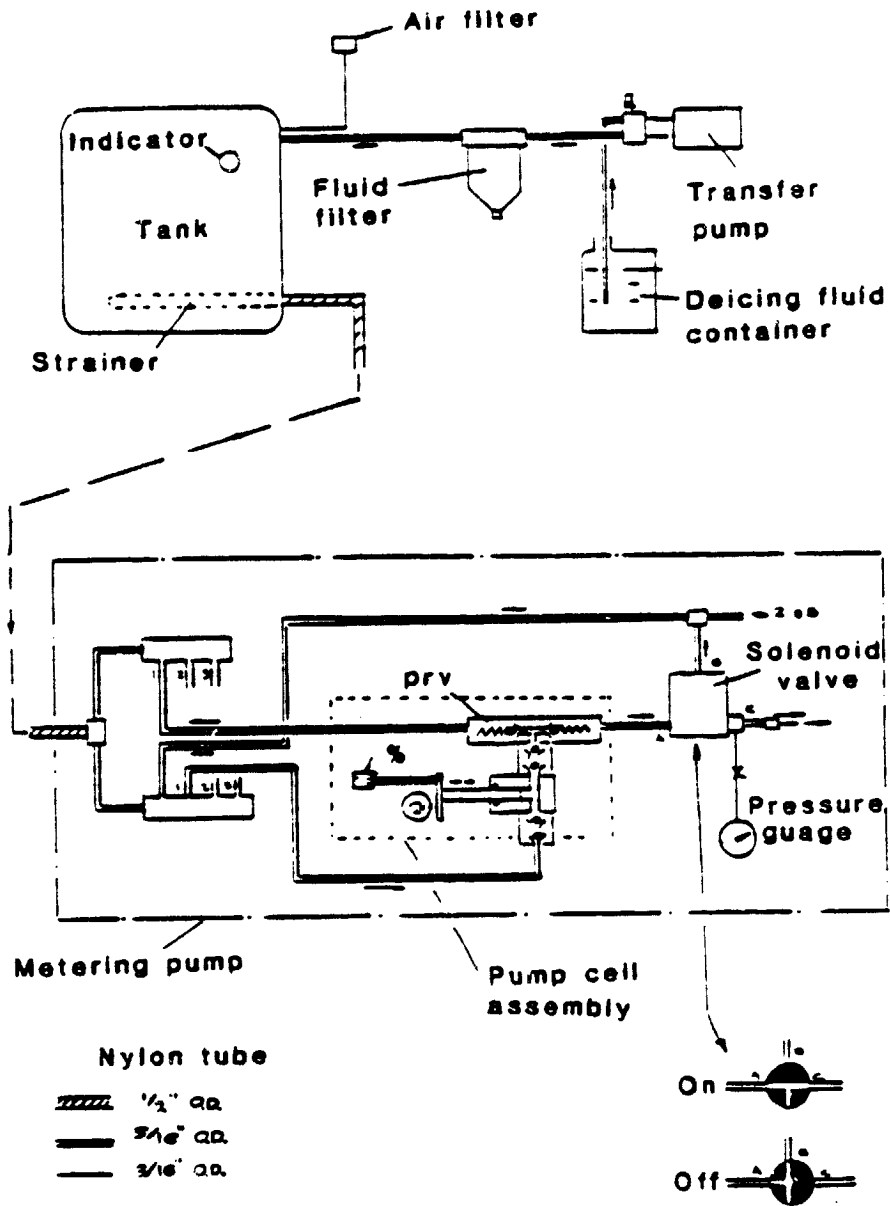
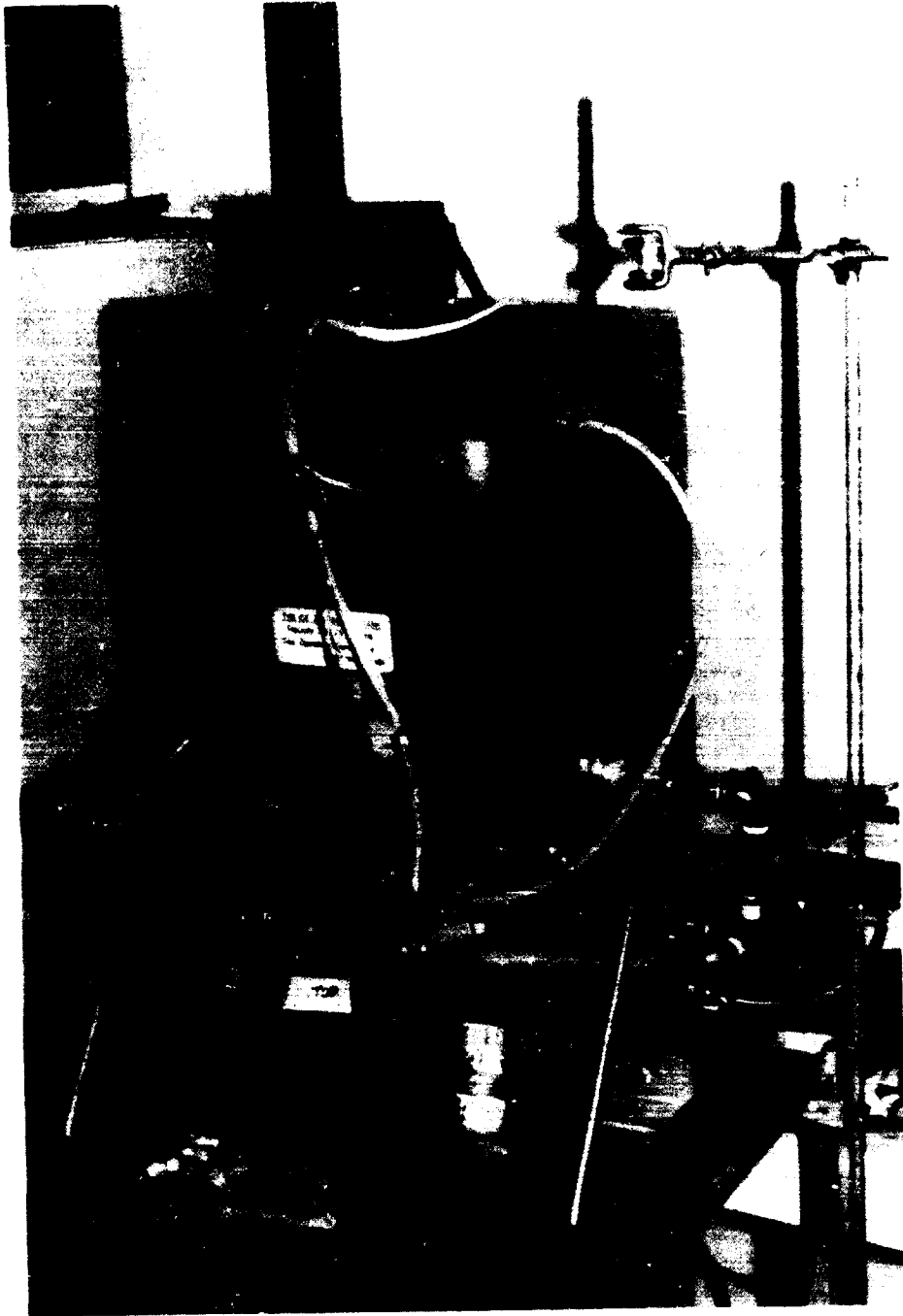


Figure 2.9. - Schematic of Fluid Supply Pump System.

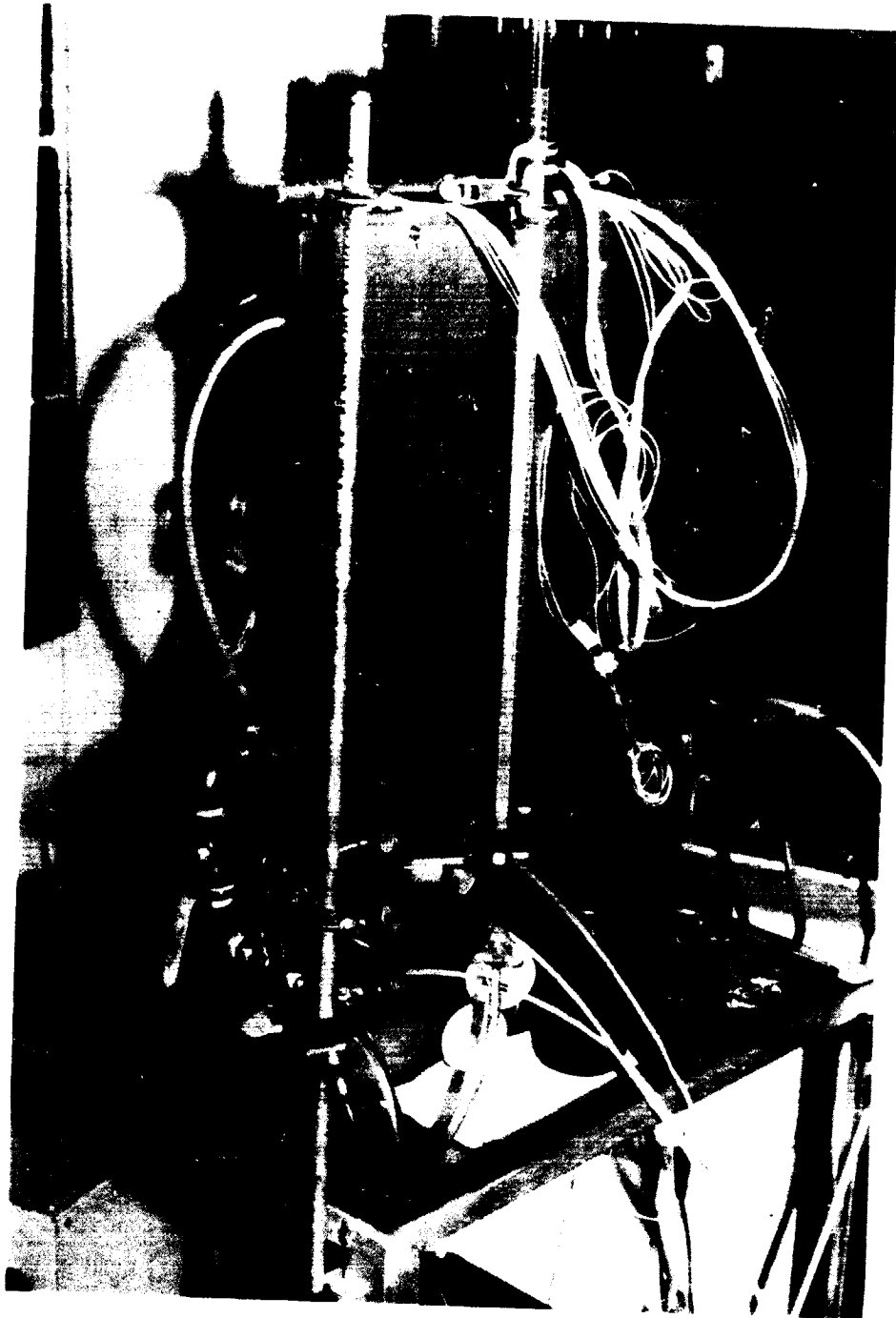
ORIGINAL PAGE IS  
OF POOR QUALITY



(a) Front View

Figure 2.10. - Fluid Pump System Apparatus Used During  
Tunnel Tests.

ORIGINAL PAGE IS  
OF POOR QUALITY



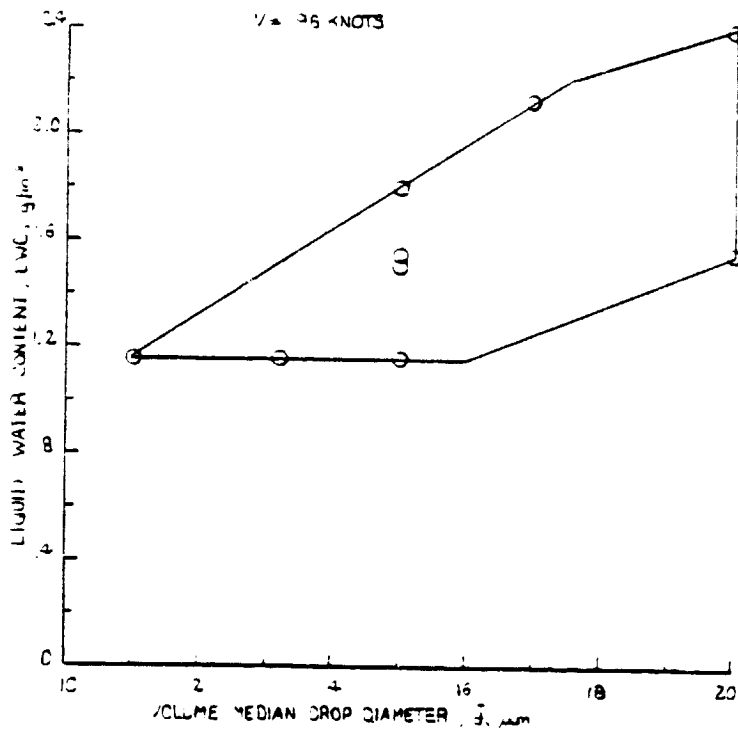
(b) Back View

Figure 2.10. - (Continued)

### 3.0 Test Techniques

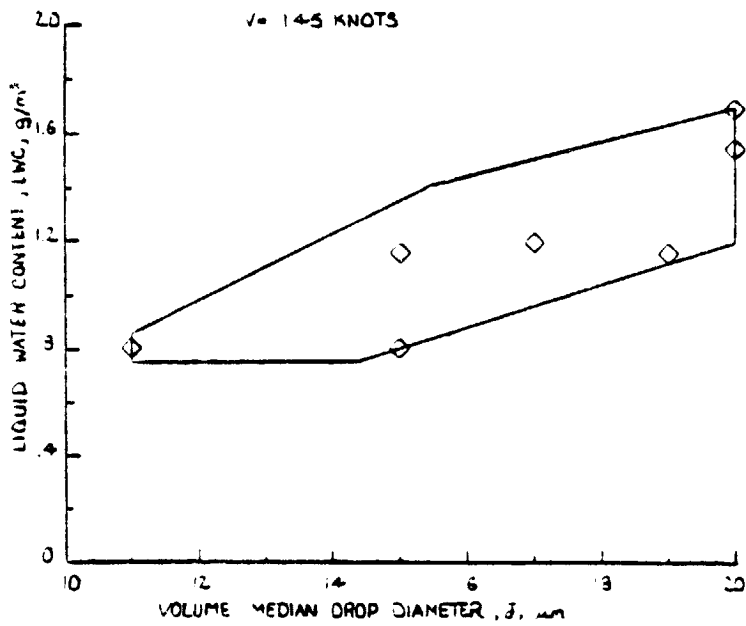
#### 3.1 Tunnel Conditions

Test airspeed conditions of 49.2 m/s (96 knots), 74.6 m/s (145 knots), and 90.2 m/s (175 knots) were selected based on the best climb and cruise speeds of aircraft on which the airfoil sections tested are used. Operating envelopes of liquid water content and drop size, dependent upon tunnel airspeed, were plotted for the airspeeds chosen. From these tunnel operating envelopes several combinations of LWC and drop size were chosen for testing, including the least and worst icing severity conditions of each envelope, as plotted on Figures 3.1 and 3.2. The type of ice (i.e. glaze, rime) that formed on the wing model depended primarily on the tunnel total air temperature (T). To accrete primarily glaze ice, the air temperature was set at -3.9 degrees C (25 degrees F); and to accrete primarily rime ice, it was set at -15.0 degrees C (5 degrees F), or at -23.3 degrees C (-10 degrees F). Figures 3.2 and 3.3 present the continuous maximum and intermittent maximum icing condition curves specified in Federal Aviation Regulations, Part 25 (ref. 5). Figures 3.4 and 3.5 overlay the IRT operating envelopes at 96, 145, and 175 knots with the continuous and intermittent maximum envelopes.

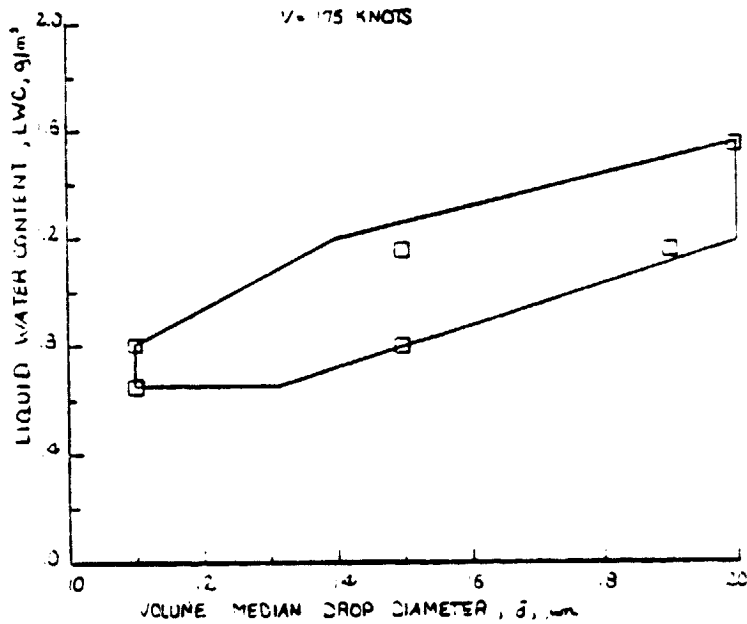


(a) V = 96 knots

Figure 3.1. - IRT Operating Envelopes and Test Points



(b) V = 145 Knots



(c) V = 175 Knots

Figure 3.1. - (Continued.)

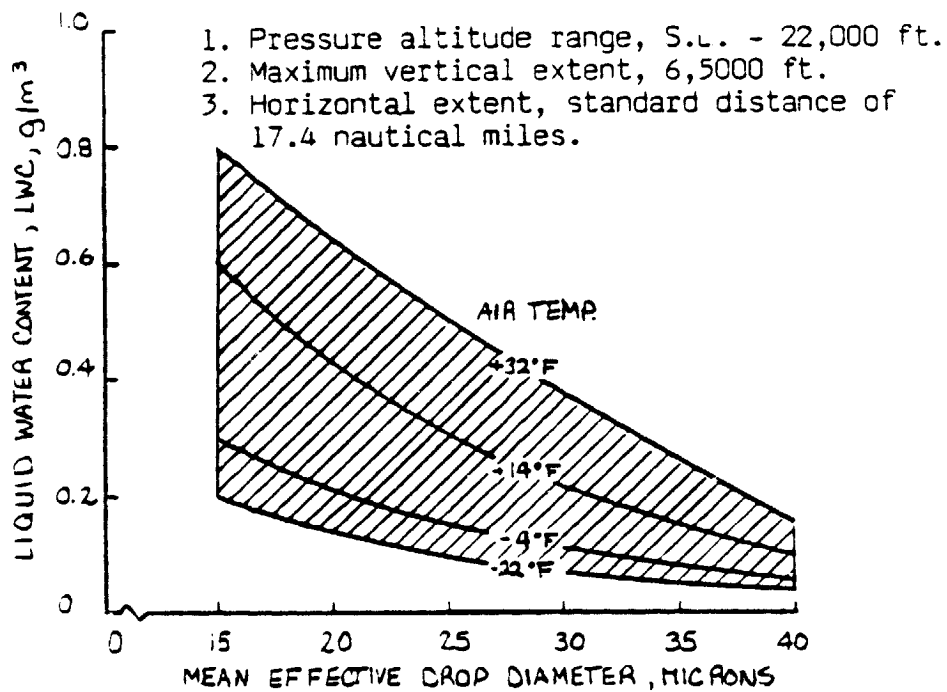


Figure 3.2. - Federal Aviation Regulations Part 25 (ref. 5)  
 Continuous Maximum Icing Conditions.

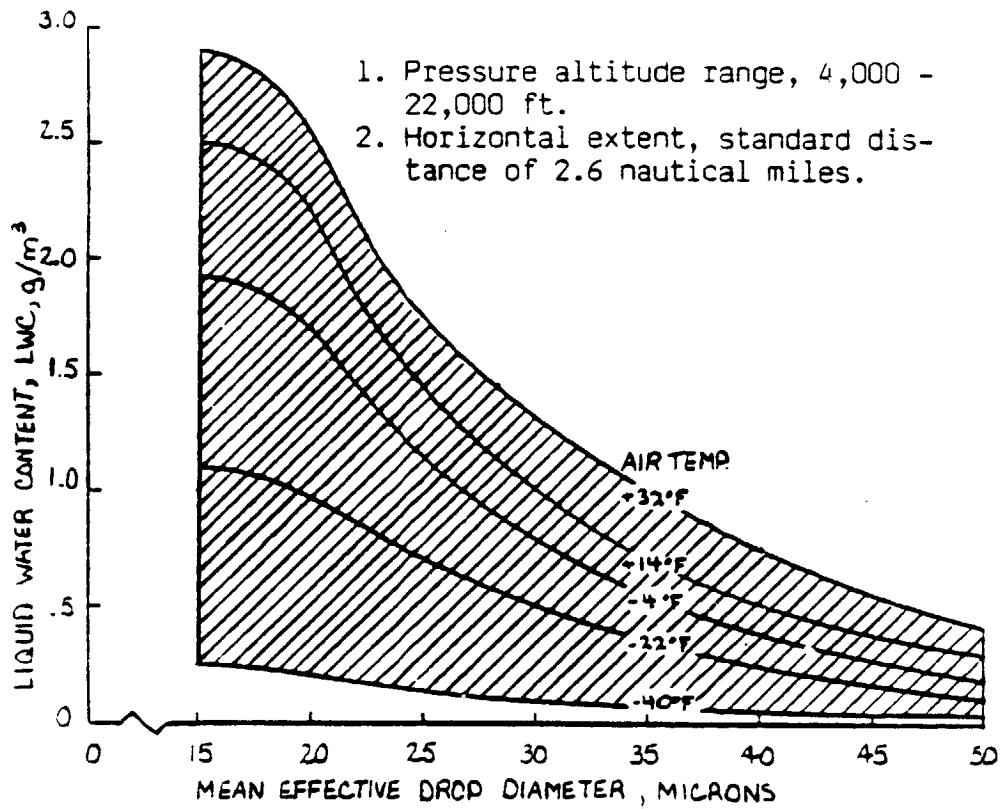


Figure 3.3. - Federal Aviation Regulations Part 25 (ref. 5 )  
 Intermittent Maximum Icing Conditions.

ORIGINAL PAGE IS  
OF POOR QUALITY

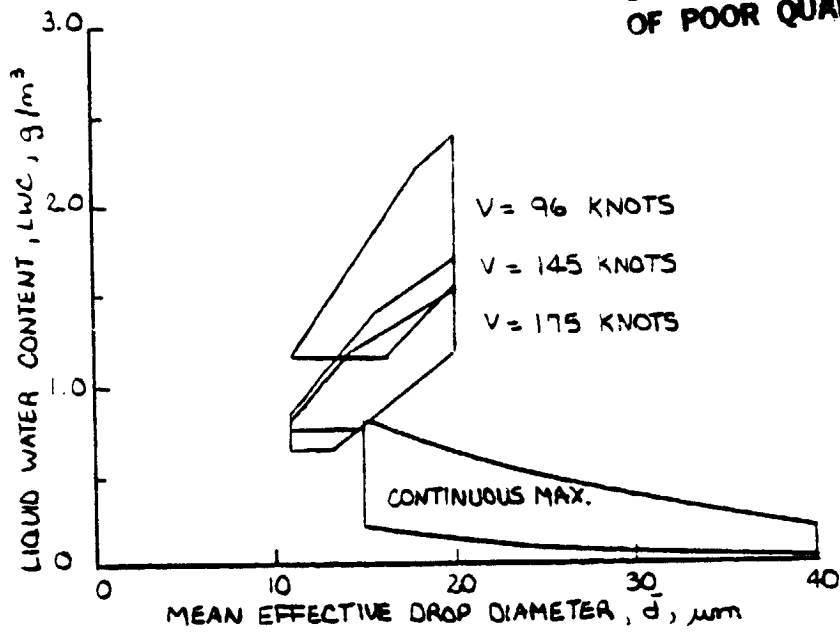


Figure 3.4. - Continuous Maximum Icing Conditions (ref. 5) and IRT Operating Envelopes.

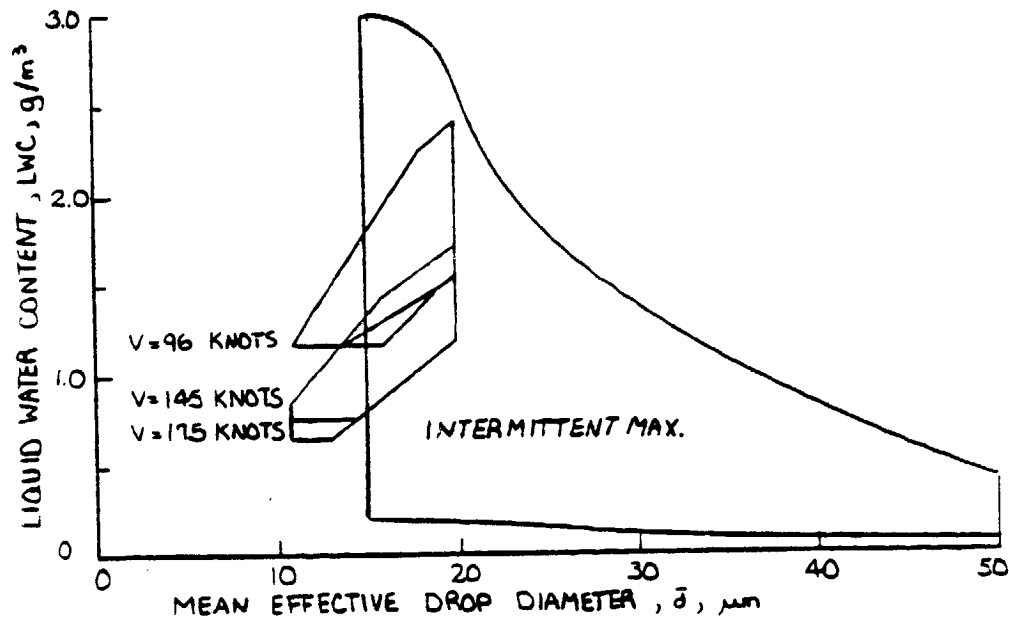


Figure 3.5. - Intermittent Maximum Icing Conditions (ref. 5) and IRT Operating Envelopes.

## 3.2 Test Procedures and Analysis

### 3.2.1 Aerodynamic

Aerodynamic data were recorded for Wing Model A in a clean condition (no ice or frost) and with ice on the wing. The clean wing test consisted of determining the location of stagnation points about the leading edge of the airfoil throughout a broad range of angles of attack. This was accomplished with the porous panel by placing 18 static ports on strip-a-tube laid chordwise at 1/2 inch intervals. The strip-a-tube was attached to the wing surface with adhesive tape. After stabilizing at the appropriate tunnel air-speed, the peak surface static pressures were recorded at each angle of attack.

The second type of aerodynamic test was performed with the ice protection system turned off, allowing ice to accrete. The procedure for this test was as follows.

- a) start with an ice and frost free wing
- b) set velocity, angle of attack, and temperature
- c) set icing cloud conditions, LWC and d
- d) turn on icing cloud
- e) after desired icing encounter, turn cloud off
- f) take drag wake survey

- g) wipe off any surface frost behind primary ice formation
- h) take a second drag wake survey
- i) clean off ice in preparation for next run

### 3.2.2 Anti-Ice

The procedure for obtaining minimum required anti-ice fluid flow rates was as follows.

- a) set velocity, angle of attack, and temperature
- b) set icing cloud conditions, LWC and d
- c) turn on glycol flow rate to center panel at  
a rate in excess of that required for anti-icing
- d) turn on icing spray
- e) slowly reduce glycol flow rate until  
minimum anti-icing is achieved
- f) turn icing spray off and prepare for next run

Initially at a given flight condition, the glycol fluid flow rate was set to be well above that required for anti-icing. The flow rate was then reduced in steps, allowing about 20 seconds for the system to stabilize, until small flecks of ice began to appear on the leading edge in the vicinity of the stagnation point. At the anti-ice flow rate small ice flecks would just begin to form before

being swept downstream in only a few seconds. A glycol flow rate slightly lower would cause the ice flecks to persist, gradually growing into larger patches before being shed from the wing. Often the first sign of ice would be a small fleck on a rivet head in the porous region of the panel near the stagnation location.

The center sections of the porous panels, in the middle of the tunnel icing cloud, were used to obtain the minimum anti-icing fluid flow rates. However, several aspects made it difficult to obtain these flow rates with a high degree of accuracy.

First, at a given glycol flow rate, regions of the center panel would be anti-icing, while at a different spanwise location, the panel would be operating closer to the natural-deice mode. It was difficult to determine the appropriate anti-ice flow rate that was characteristic of the entire center panel. Second, on many of the icing conditions, the transition from anti-icing to deicing was subtle, as it occurred over a broad range of glycol flow rates. It was therefore difficult to determine the unique minimum anti-ice flow rate. Finally, it was difficult to observe the small ice particles forming and shedding on the wing from a distance of five feet, while looking through an icing cloud. This problem was partially alleviated by sighting through a short range telescope with a field of view of approximately 4 inches in diameter on the leading edge.

Because of the subjectiveness involved in determining the anti-ice flow rates, each unique icing condition was tested from one to five times. An average flow rate at each icing condition was then calculated. It is believed that this average value is more representative of the true anti-ice flow rate, than a single test point. Because of the subjectiveness involved in obtaining these flow rates, a second observer, a NASA engineer in the Aircraft Icing Research Section, independently judged flow rates during the test series on Wing Model B with the stainless steel panel. Equal weight was given to the two observations in determining the average flow rate.

### 3.2.3 Deice

The test procedure for determining the time required to shed an ice accretion at various icing conditions and glycol flow rates was as follows:

- a) set velocity, angle of attack, and temperature
- b) set glycol flow to inboard and outboard panels  
sufficient for anti-icing
- c) set icing conditions, LWC and d
- d) turn spray on to accrete ice on center panel
- e) turn spray off after desired icing encounter

- f) turn glycol flow on to center panel
- g) record elapsed time after beginning glycol flow to center panel until ice cap sheds
- h) clean ice and frost off wing in preparation for next run.

#### 4.0 Test Results and Discussions

##### 4.1 Aerodynamic

Figures 4.1.1 and 4.1.2 present the stagnation point locations for angles of attack ranging from -2 to 12 degrees on Wing Model A and B, respectively. Stagnation locations for angles ranging from 0 to 11 degrees fall within the porous region of the leading edge panel installed on Wing Model A. On Wing Model B, stagnation locations for angles from approximately -1.5 to over 12 degrees fall within the porous region.

As reported in reference 1, the installation of the stainless steel porous panel on Wing Model B adds less than .001 to the section drag of the wing, within the uncertainty band of the drag measuring system.

In order to obtain an understanding of the aerodynamic penalties associated with ice accretions on a wing leading edge, a brief test was conducted on Wing Model A with the ice protection system

inoperative. The test runs were conducted at a velocity of 145 knots and an angle of attack of 2.1 degrees.

Glaze ice, accreted at 25 degrees F, is characterized by the typical double horn ice formation. As a result, the drag penalties associated with an extended glaze icing encounter can be severe. Figures 4.1.3 a and b illustrate the percent increase in drag coefficient above the clean wing drag,  $c_{do}$ , for glaze icing at two liquid water contents. Figures 4.1.4 and 4.1.5 present pictures of the corresponding ice shapes.

Rime ice, accreted at 5 degrees F, conforms more to the original airfoil contour as the impinging water droplets freeze on impact. The resulting drag increases associated with rime icing are presented in Figures 4.1.6 a and b. The pictures of the corresponding ice accretions are given in Figures 4.1.7 and 4.1.8.

After a 15 minute glaze icing encounter at a LWC of  $1.16 \text{ g/m}^3$  and drop diameter of 15 microns, the percent increase in drag from the ice cap alone was 74 %. However, a rime ice accretion increased the drag only 22 %. This higher drag penalty associated with glaze icing also occurs at the higher liquid water content of  $1.55 \text{ g/m}^3$  where a 15 minute glaze icing encounter increased the drag by 176 %. However, a rime ice accretion increased the drag only 73 % .

Also plotted in Figures 4.1.3 and 4.1.6 are the percent increases in drag from surface frost. This frost, which often forms on the upper and lower surfaces of a wing section in the IRT, may

not occur during a natural icing encounter. It is interesting to note the large increases in drag associated with the frost layer alone. After a 15 minute icing encounter, the additional percent of drag increase ranged from 50 to 100 percent above that from the ice cap alone.

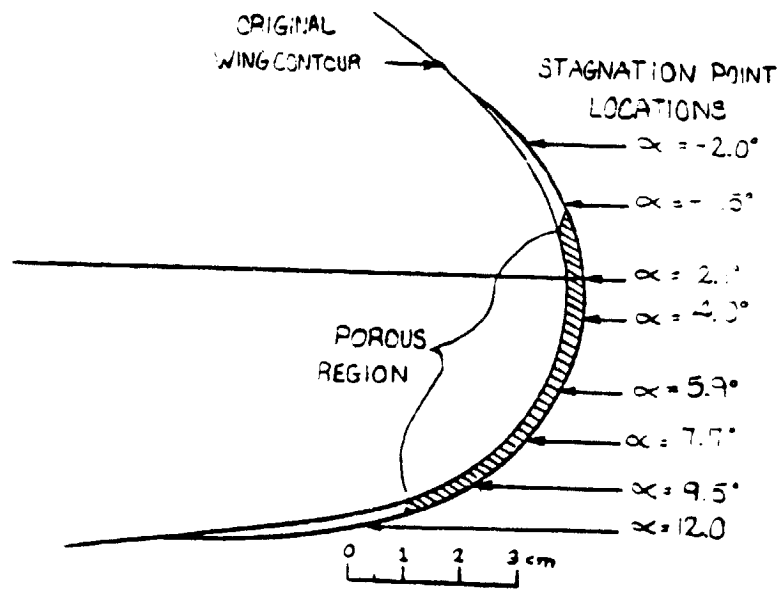


Figure 4.1.1. - Stagnation Point Locations on Wing Model A.

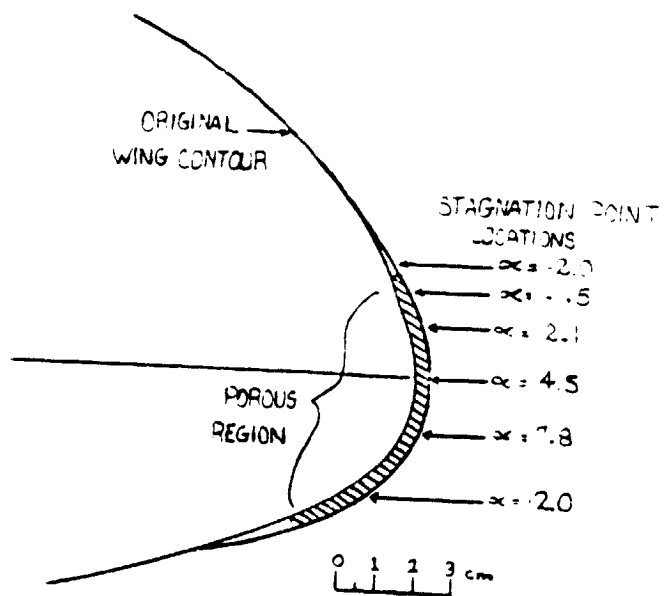
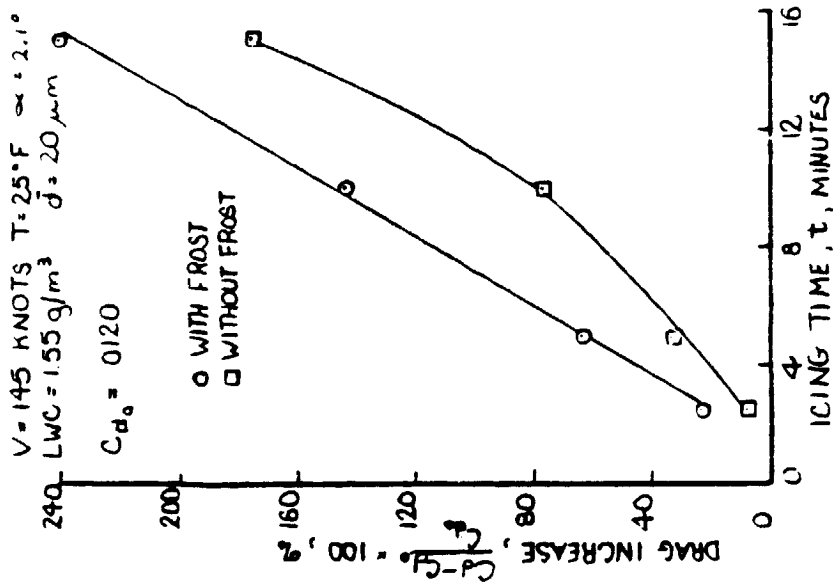
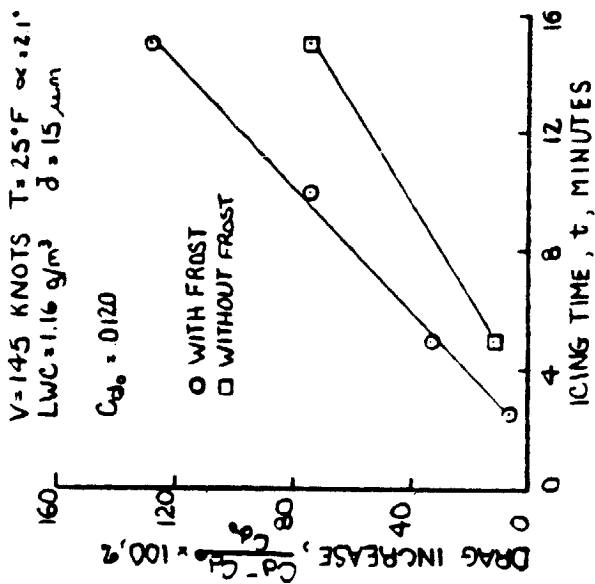


Figure 4.1.2. - Stagnation Point Locations on Wing Model B.

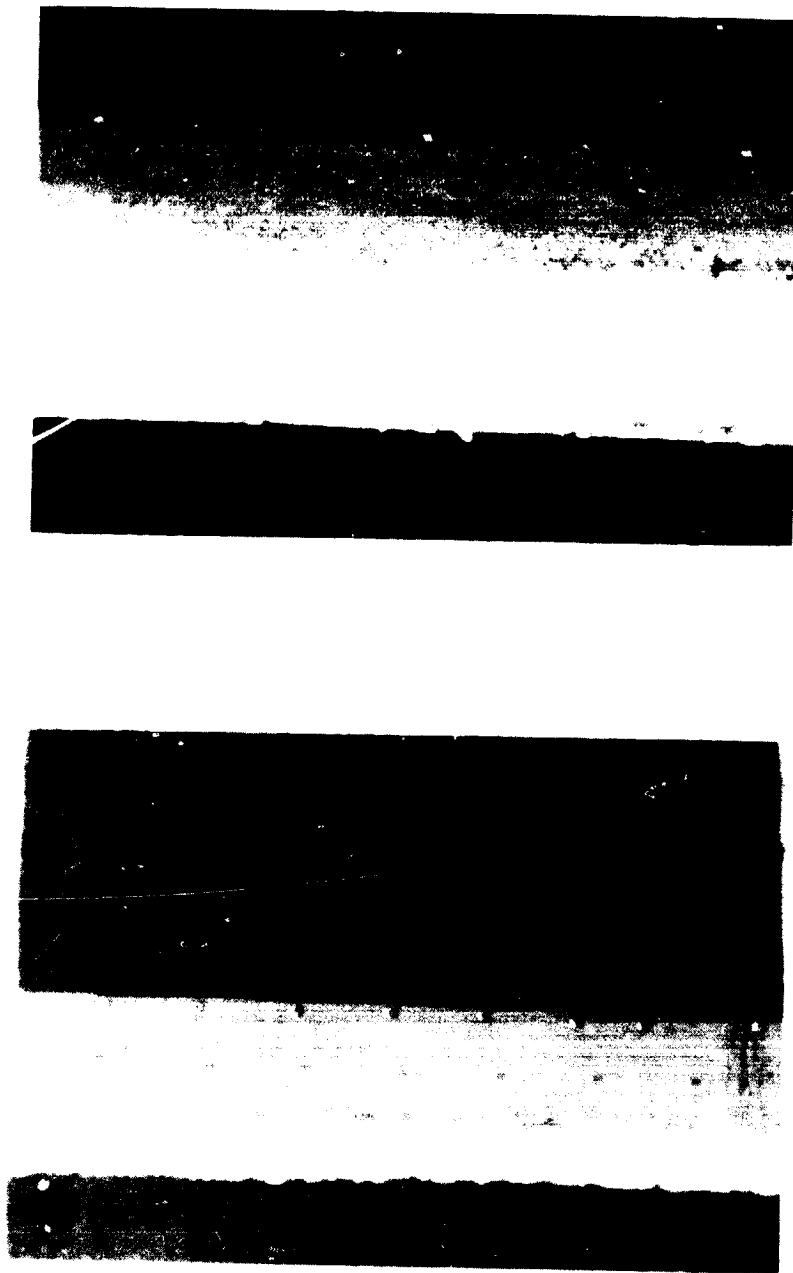


(b)  $LWC = 1.55 \text{ g/m}^3$ ,  $d = 20$  microns



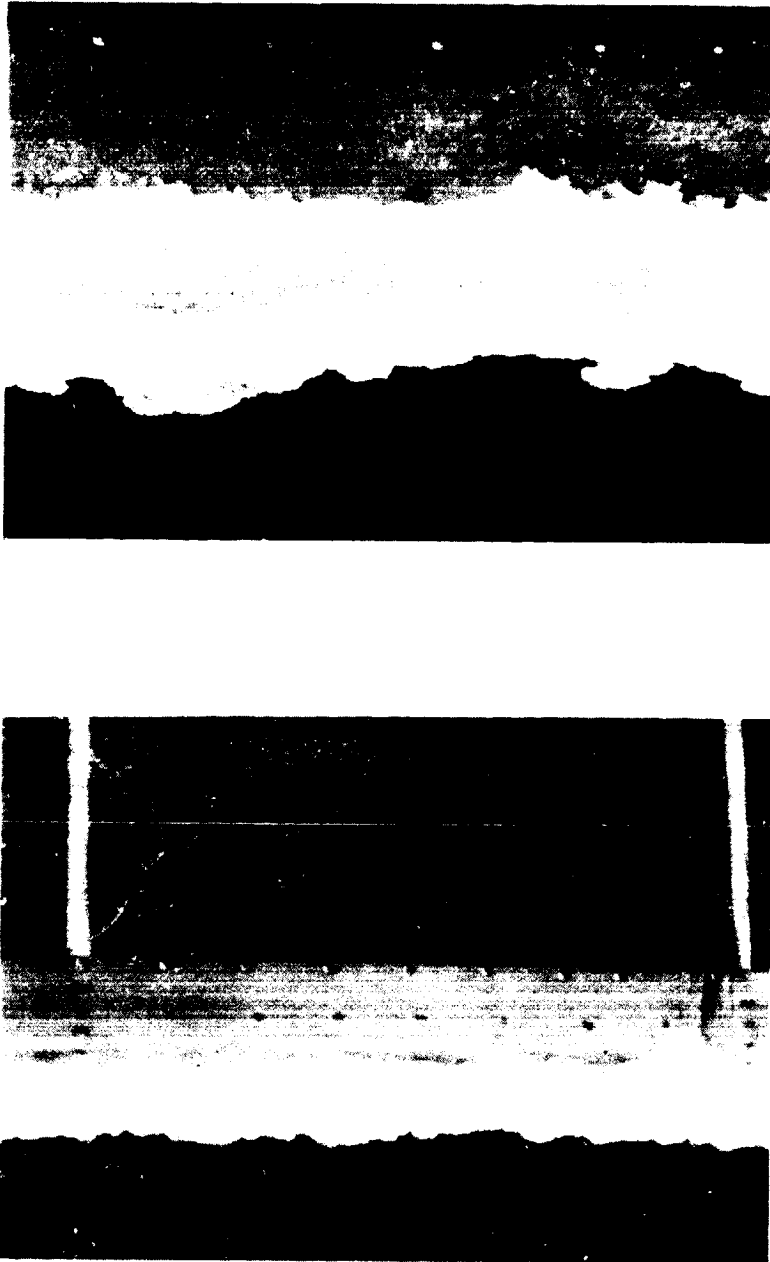
(a)  $LWC = 1.16 \text{ g/m}^3$ ,  $d = 15$  microns

Figure 4.1.3. - Drag Increase as a Result of a Glaze Icing Encounter at  $V = 145$  Knots,  $T = 25^\circ\text{F}$ , and Angle of Attack =  $2.1^\circ$ .



(a) 2.5 Minute Icing Spray

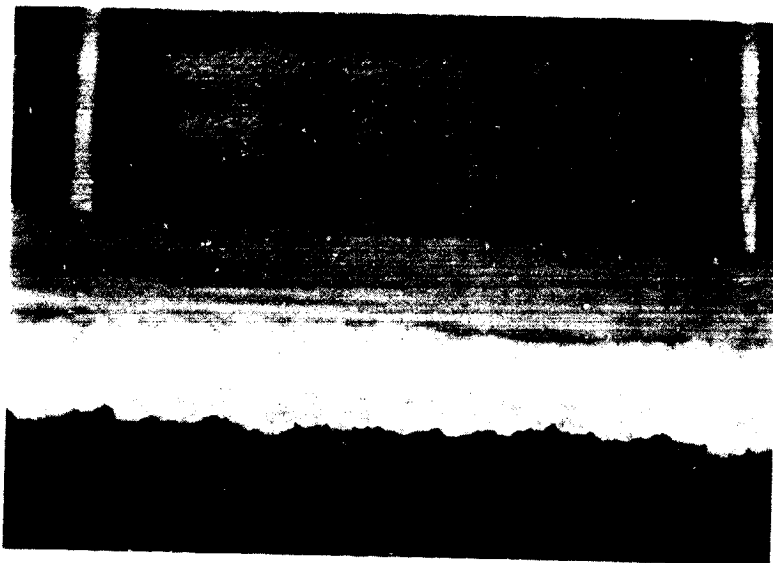
Figure 4.1.4. - Glaze Ice Accreted at  $V = 145$  Knots,  $T = 25^\circ$  F, Angle of Attack =  $2.1^\circ$ ,  
LWC =  $1.16 \text{ g/m}^3$ , and  $d = 15$  microns.



(b) 10. Minute Icing Spray

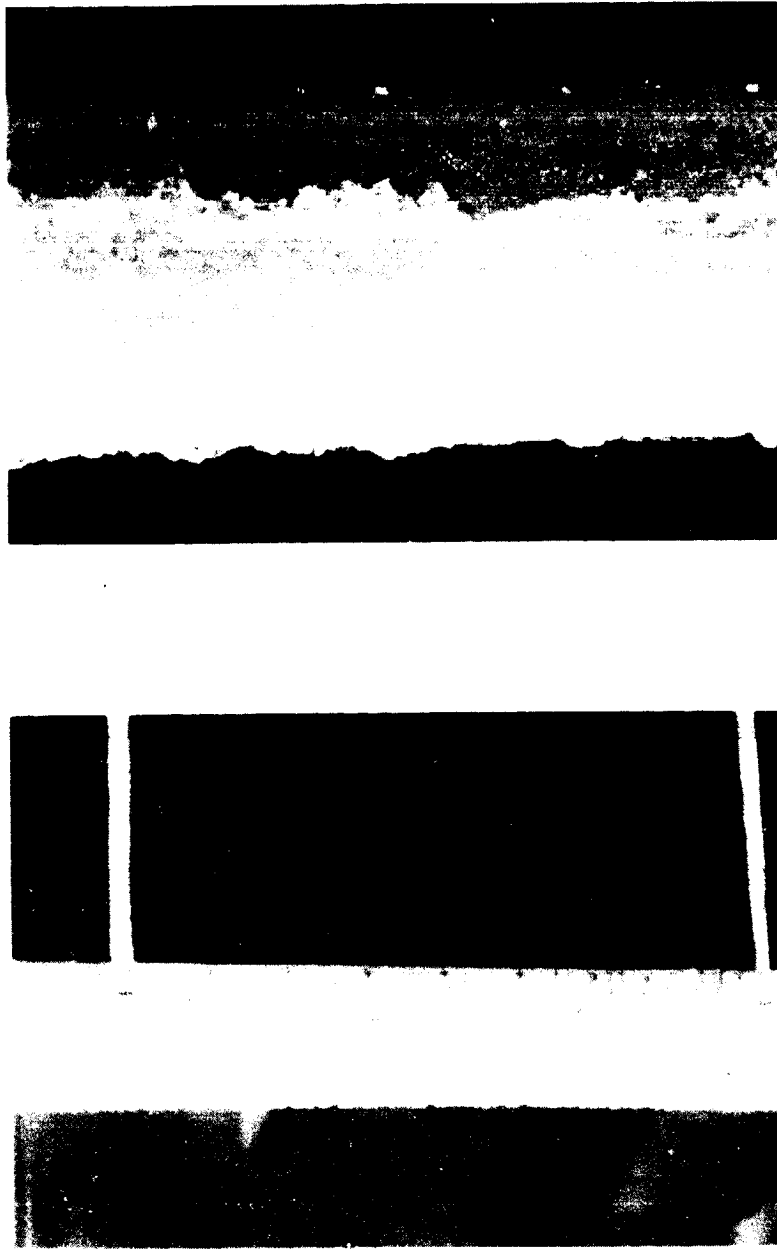
Figure 4.1.4. - (Continued.)

ORIGINAL PAGE IS  
OF POOR QUALITY



(c) 15. Minute Icing Spray

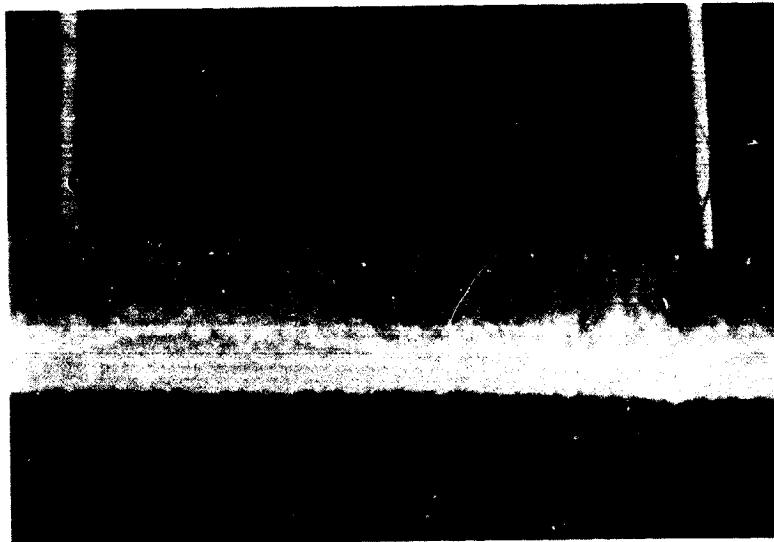
Figure 4.1.4. - (Continued.)



(a) 2.5 Minute Icing Spray

Figure 4.1.5. - Glaze Ice Accreted at  $V = 145$  Knots,  $T = 25^\circ$  F, Angle of Attack =  $2.1^\circ$ ,  
LWC =  $1.55 \text{ g/m}^3$ , and  $d = 20$  microns.

ORIGINAL PAGE IS  
OF POOR QUALITY



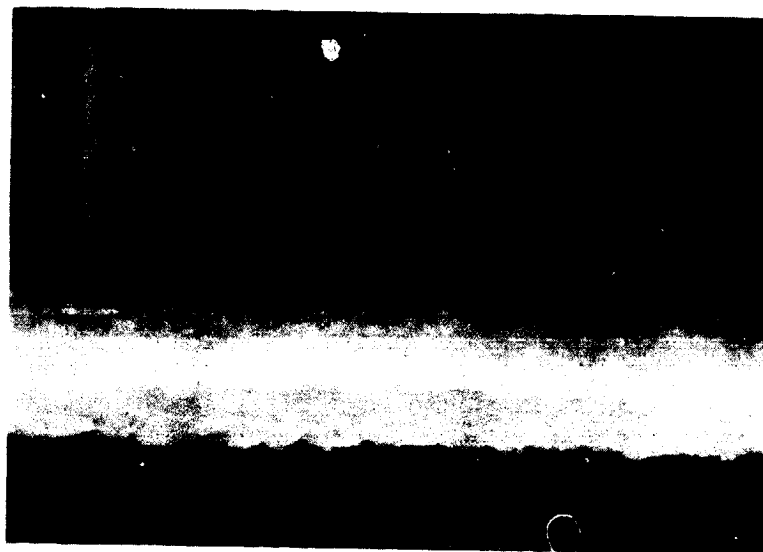
(b) 5.0 Minute Icing Spray

Figure 4.1.5. - (Continued.)

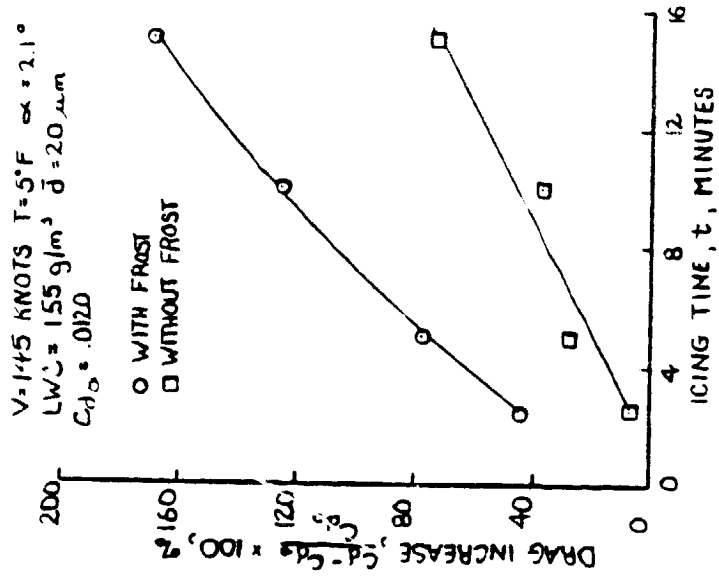


(c) 10. Minute Icing Spray  
Figure 4.1.5\* - (Continued.)

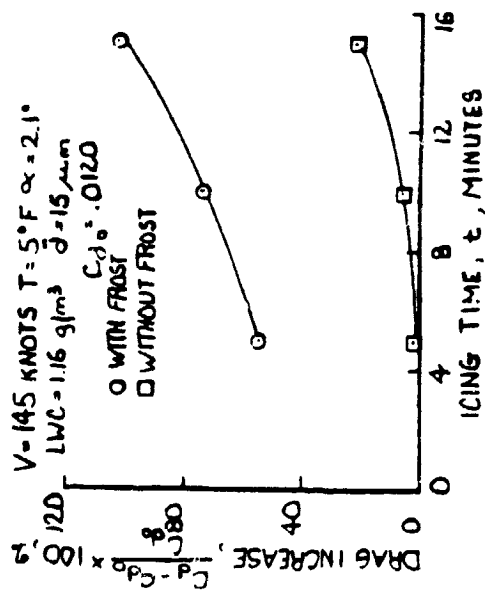
ORIGINAL PAGE IS  
OF POOR QUALITY



(d) 15. Minute Icing Spray  
Figure 4.1.5. (Continued.)

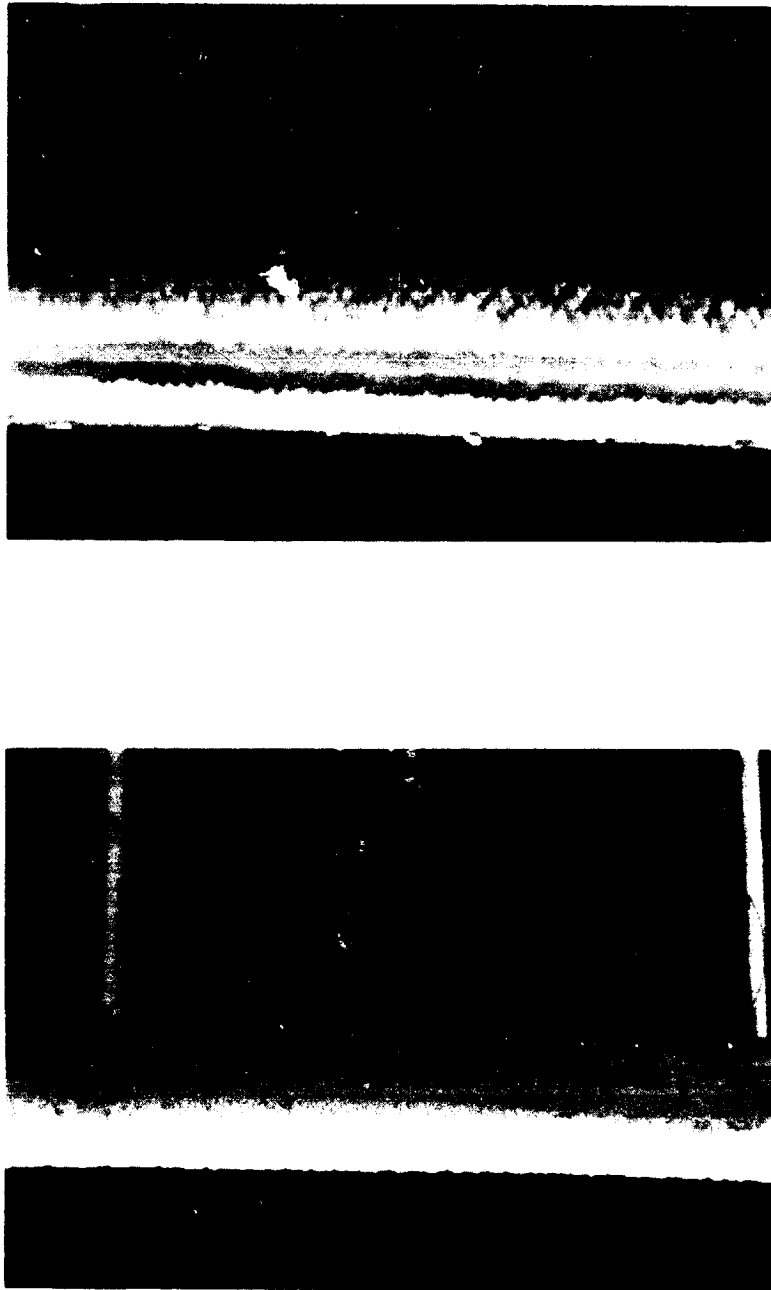


(b)  $LWC = 1.55 \text{ g/m}^3$ ,  $d = 20 \text{ microns}$



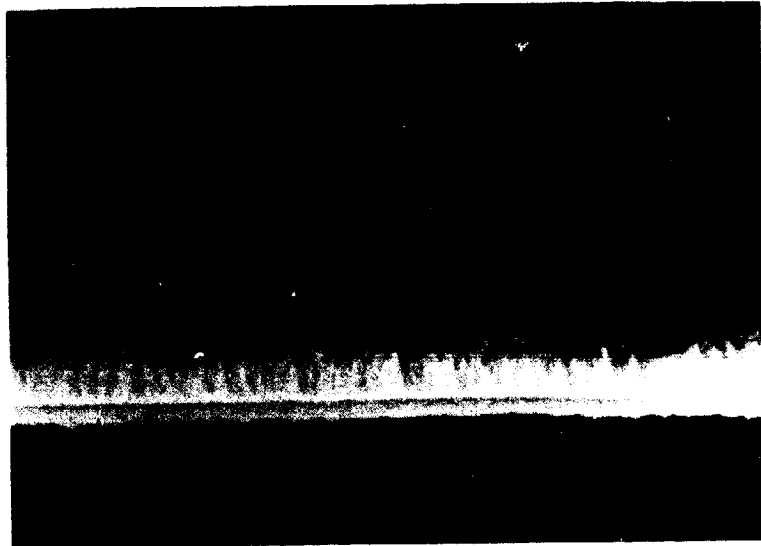
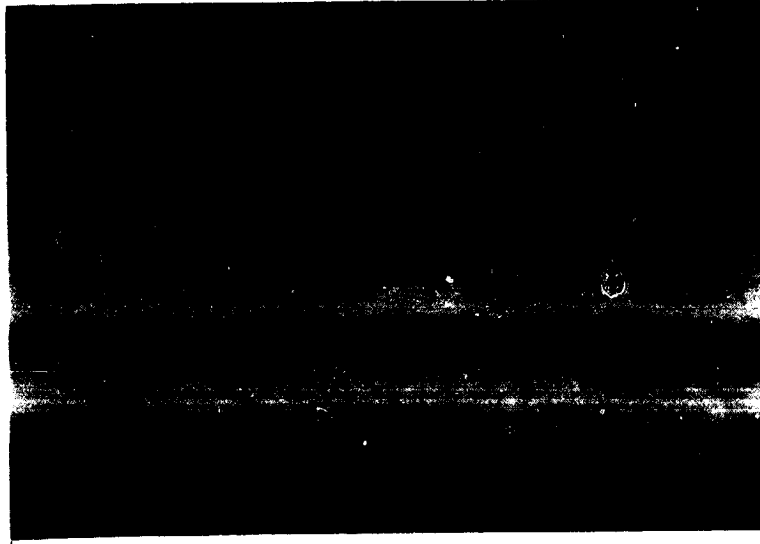
(a)  $LWC = 1.16 \text{ g/m}^3$ ,  $d = 15 \text{ microns}$

Figure 4.1.6. - Drag Increase as a Result of a Rime Icing Encounter at  $V = 145$  Knots,  $T = 25^\circ\text{F}$ , and Angle of Attack =  $2.1^\circ$ .



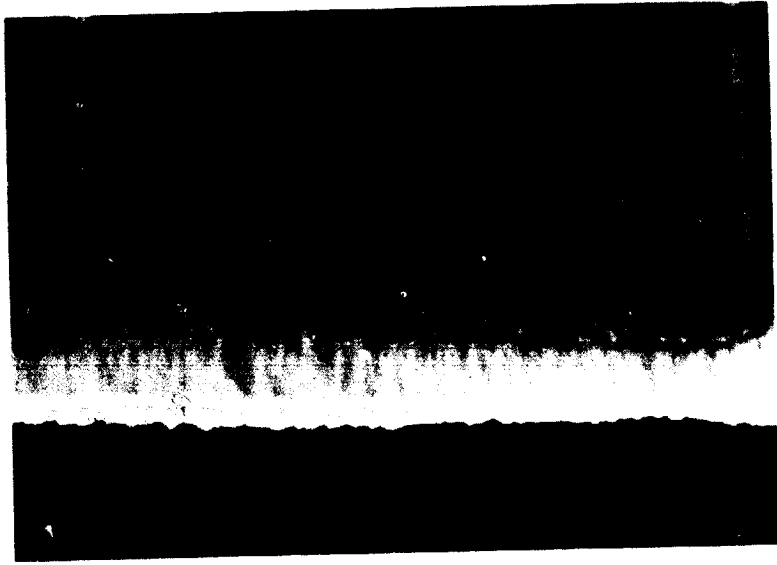
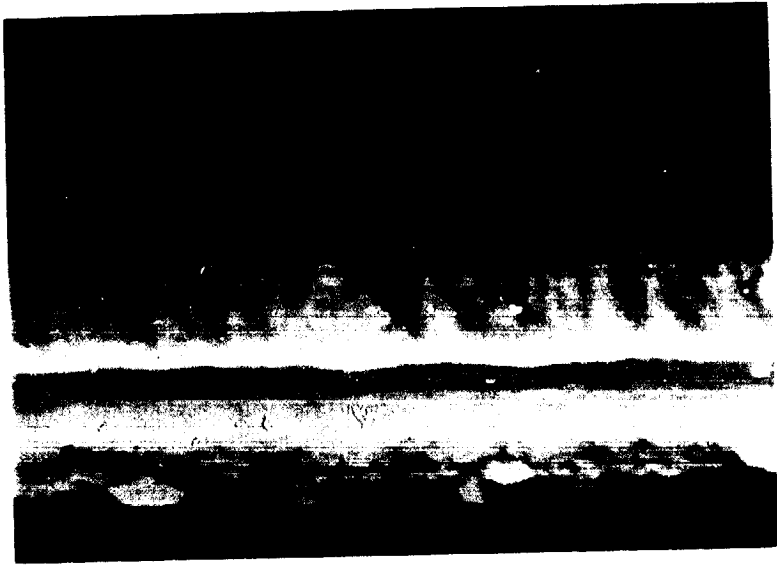
(a) 5.0 Minute Icing Spray

Figure 4.1.1.7. - Rime Ice Accreted at  $V = 145$  Knots,  $T = 5^{\circ} F$ , Angle of Attack =  $2.1^{\circ}$ ,  
LWC =  $1.16 \text{ g/m}^3$ , and  $d = 15$  microns.

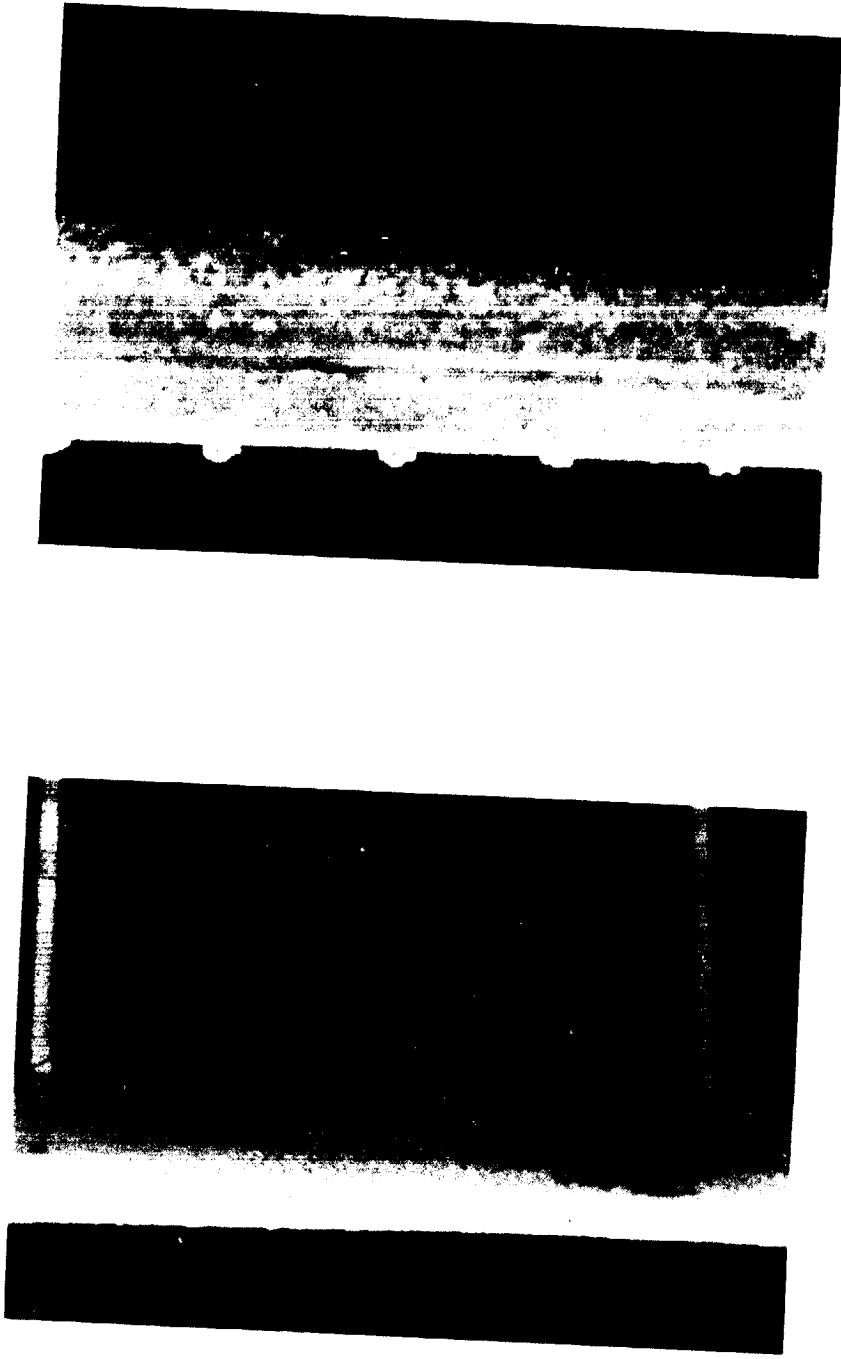


(b) 10. Minute Icing Spray  
Figure 4.1.7. - (Continued.)

ORIGINAL PAGE IS  
OF POOR QUALITY



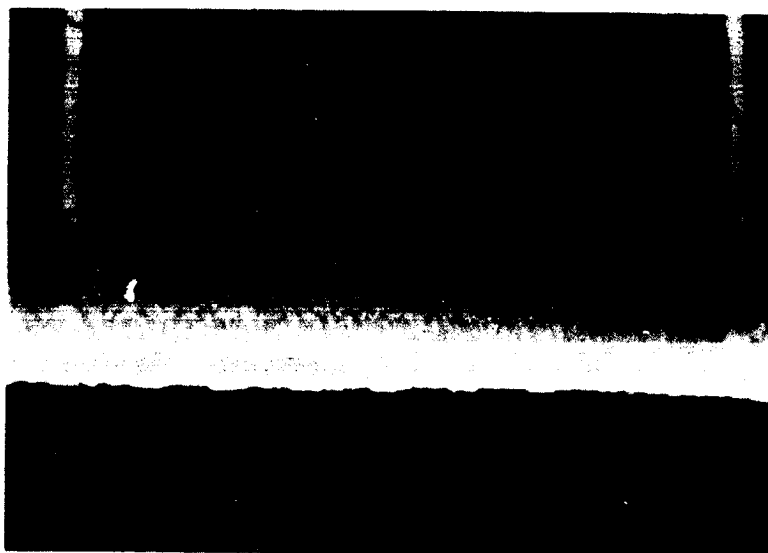
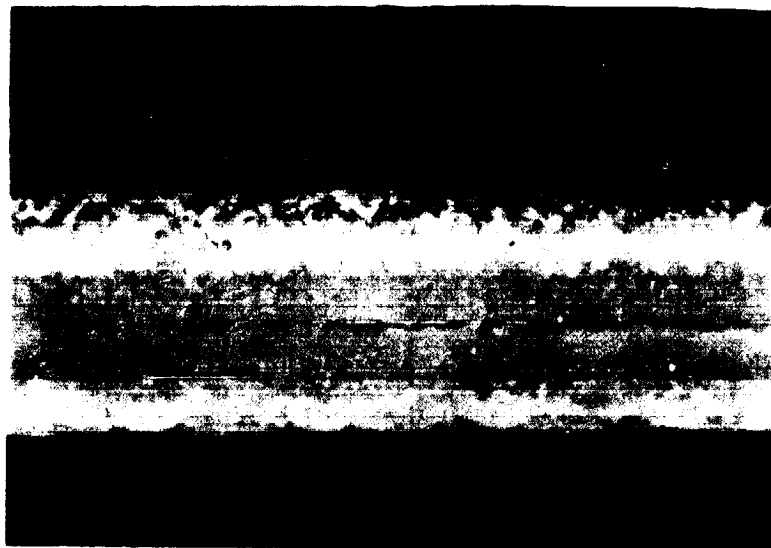
(c) 15. Minute Icing Spray  
Figure 4.1.7. - (Continued.)



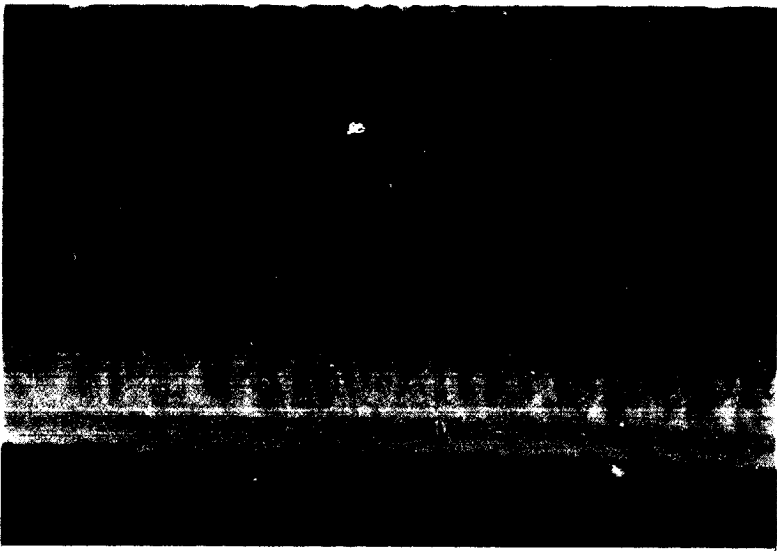
(a) 2.5 Minute Icing Spray

Figure 4.1.1.8. - Rime Ice Accreted at  $V = 145$  Knots,  $T = 5^\circ F$ , Angle of Attack =  $2.1^\circ$ ,  
LWC =  $1.55 \text{ g/m}^3$ ,  $d = 20$  microns.

ORIGINAL PAGE IS  
OF POOR QUALITY

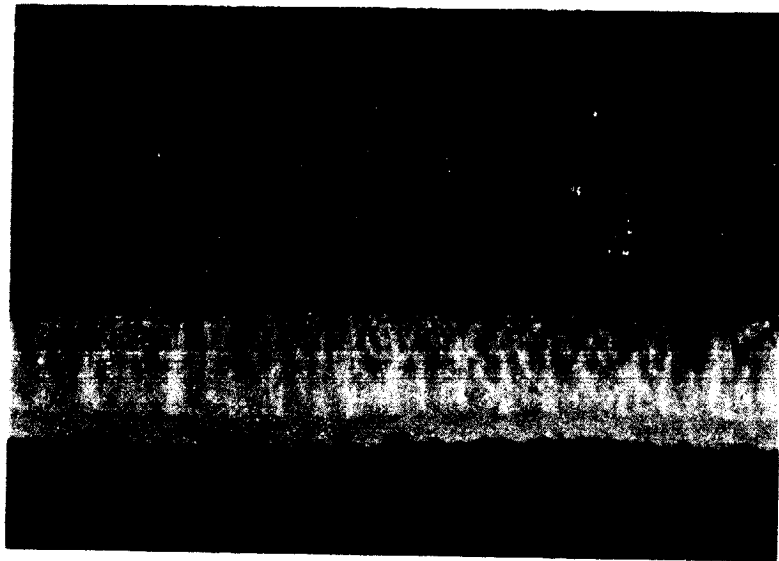


(b) 5.0 Minute Icing Spray  
Figure 4.1.8. - (Continued.)



(c) 10. Minute Icing Spray  
Figure 4.1.1.8. - (Continued.)

ORIGINAL PAGE IS  
OF POOR QUALITY



(d) 15. Minute Icing Spray  
Figure 4.1.8. - (Continued.)

## 4.2 Anti-Ice

Normal operation of the fluid ice protection system is in the anti-ice mode (Fig. 4.2.1); that is, the glycol flow rate is sufficient to prevent ice from forming on the leading edge of the wing. This is possible as long as the glycol-water mixture at the leading edge maintains a freezing temperature below the ambient air temperature. The freezing temperature of the mixture increases as the ratio of the water catch rate to the glycol flow rate increases. A series of runs was conducted in the NASA LeRC IRT to determine the minimum fluid flow rate at which anti-icing could be maintained as a function of angle of attack, liquid water content, and drop diameter on the following wing-panel configurations.

- Wing Model A, Stainless Steel Mesh Panel
- Wing Model B, Stainless Steel Mesh Panel
- Wing Model A, Drilled Titanium Panel

The anti-ice flow rates are presented in terms of specific fluid flow; grams of glycol fluid per square centimeter of active panel per minute. Tables A.1 through A.6 in Appendix A present the complete summary of the wind tunnel results on the three configurations. A significant portion of these results is presented in Figures 4.2.2 through 4.2.11. The symbols represent the actual

recorded data as listed in Appendix A. The solid and dashed lines connect the average fluid flow values calculated at each icing condition.

ORIGINAL PAGE IS  
OF POOR QUALITY

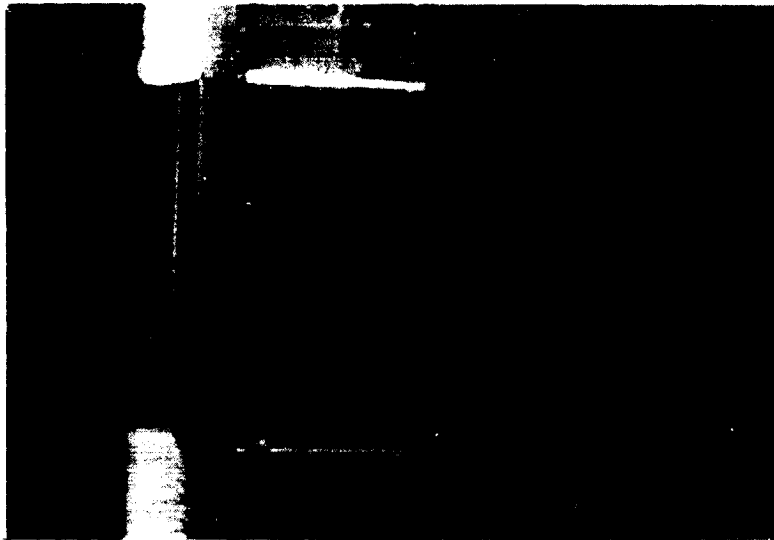


Figure 4.2.1. - Anti-Iced Center Section of Stainless Steel Mesh Panel and Wing Model.

#### 4.2.1 Stainless Steel Mesh Panel

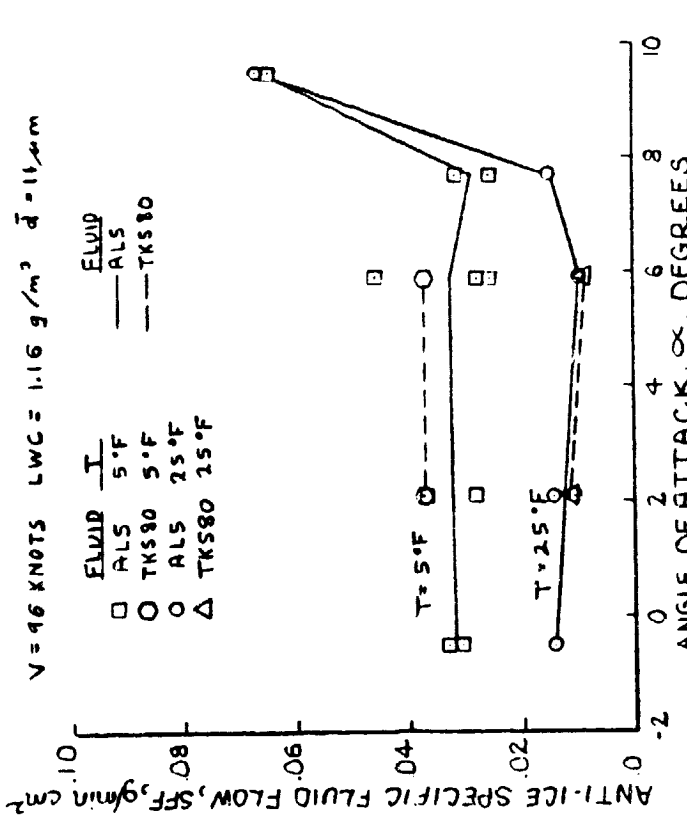
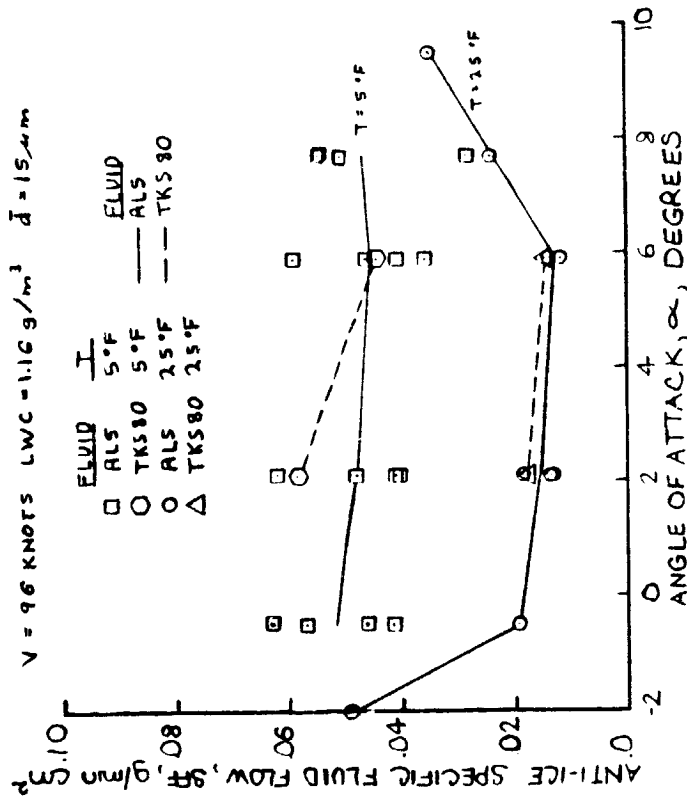
Tables A.1 and A.2 present the anti-ice flow rates determined on the Wing Model A with the stainless steel panel. Table A.1 lists the runs using the AL5 fluid. Table A.2 lists the runs using the TKS80 fluid. From these Tables, Figures 4.2.2, 4.2.3, and 4.2.4 were plotted showing the anti-ice fluid flow versus angle of attack, liquid water content, and volume median drop diameter respectively.

A few general observations can be made concerning the results. First, the minimum anti-ice fluid flow rate increases as the stagnation location comes close to an edge of the porous region. This increase is noticed at both high and low angles of attack. At a high angle of attack, for example, the majority of the water droplets impact on the lower surface, while most of the glycol solution flows over the upper surface. As expected, the anti-ice fluid flow increases with liquid water content. Also, a noticeable increase in required flow rate occurs as the drop diameter is increased from 11 to 15 microns.

Tables A.3 and A.4 present the anti-ice flow rates determined on Wing Model B with the stainless steel panel. Table A.3 lists the runs judged by Observer 1. Table A.4 lists the runs judged by Observer 2. From these Tables, Figures 4.2.5, 4.2.6, 4.2.7, and 4.2.8 were plotted showing the anti-ice fluid flow versus angle of attack, liquid water content, volume median drop diameter, and tunnel air-

speed.

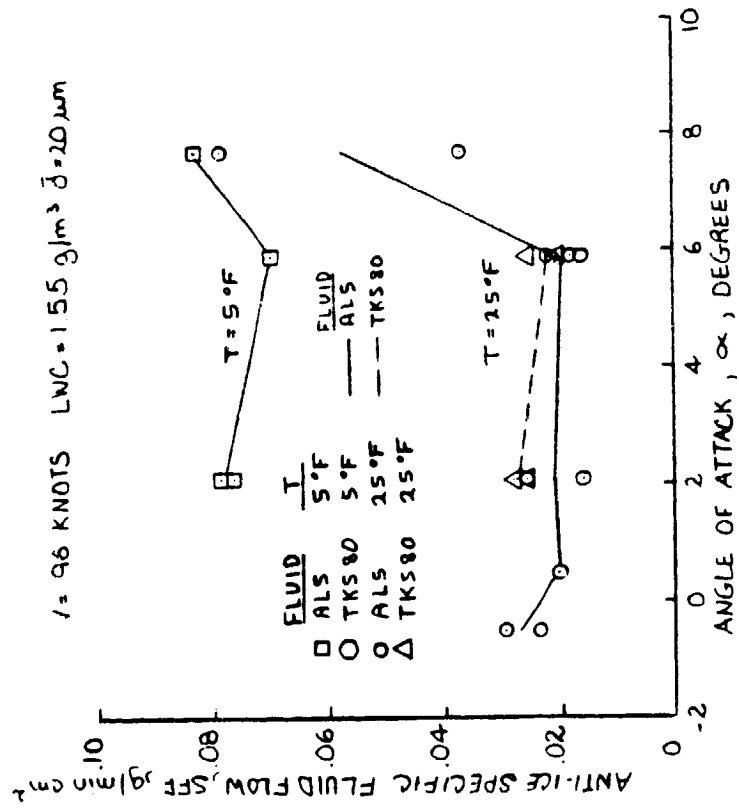
On this configuration, the anti-ice specific fluid flow does not appear to be as strongly affected by angle of attack. This is verified by referring back to Figure 4.1.2, showing that the porous region of the panel encompasses a broader range of stagnation point locations.



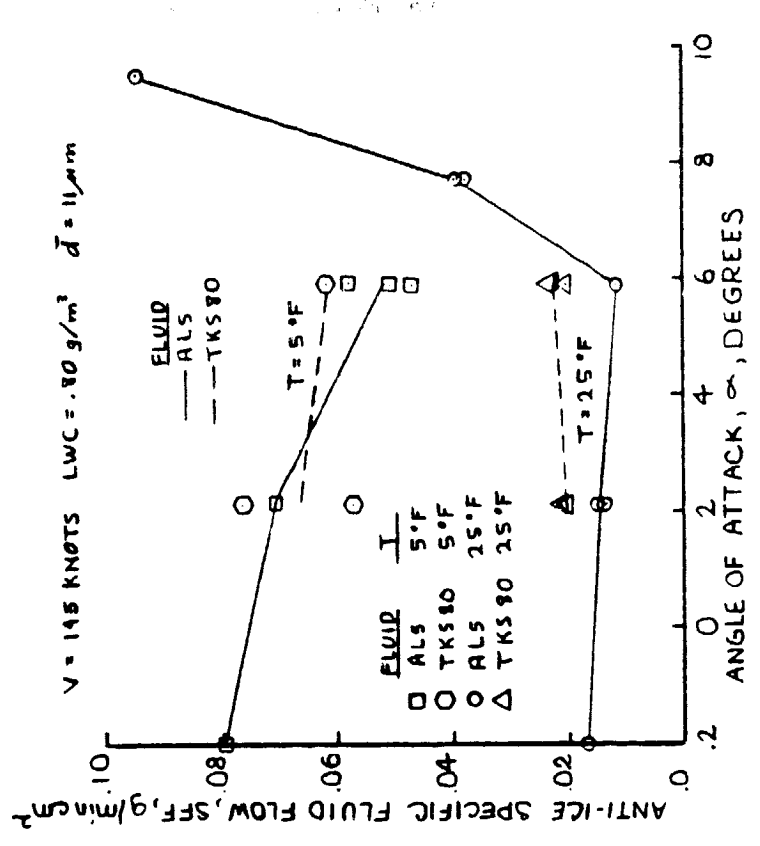
(a) V = 96 knots, LWC = 1.16 g/m<sup>3</sup>, d = 15 microns

(b) V = 96 knots, LWC = 1.16 g/m<sup>3</sup>, d = 11 microns

Figure 4.2.2. - Minimum Anti-Ice Fluid Flow Rates Versus Angle of Attack on Wing Model A with Stainless Steel Mesh Panel.

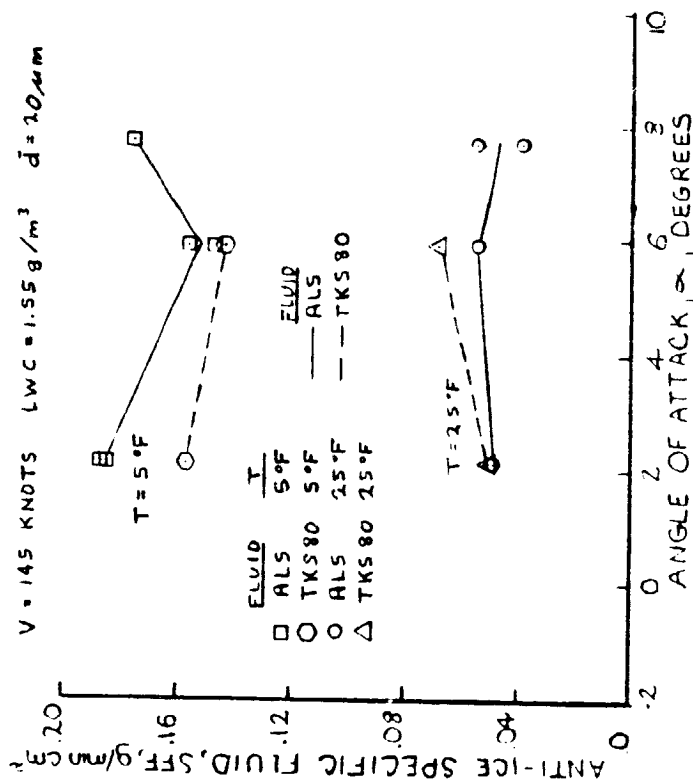
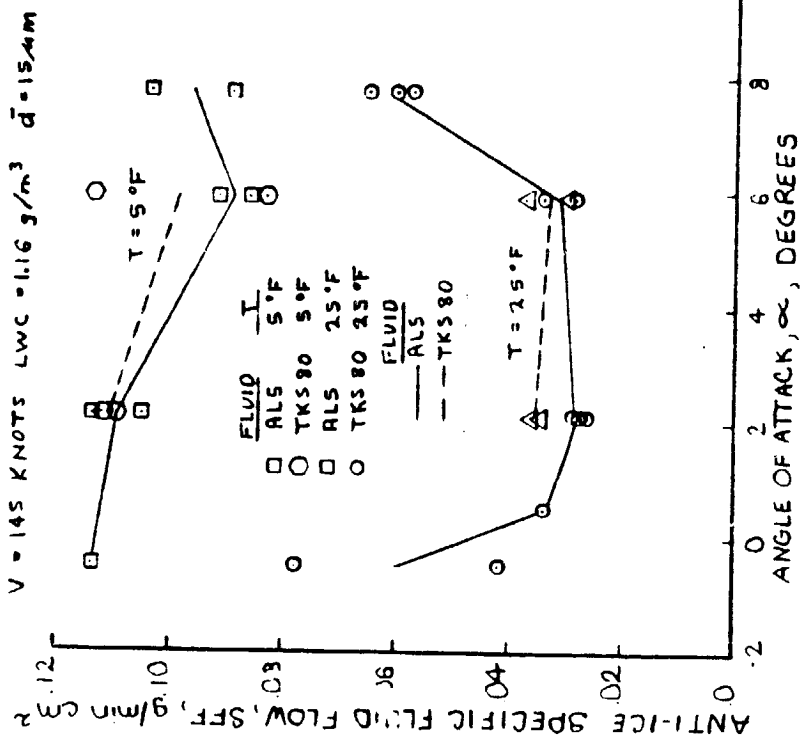


(c) V = 96 Knots, LWC = 1.55 g/m<sup>3</sup>, d = 20 microns



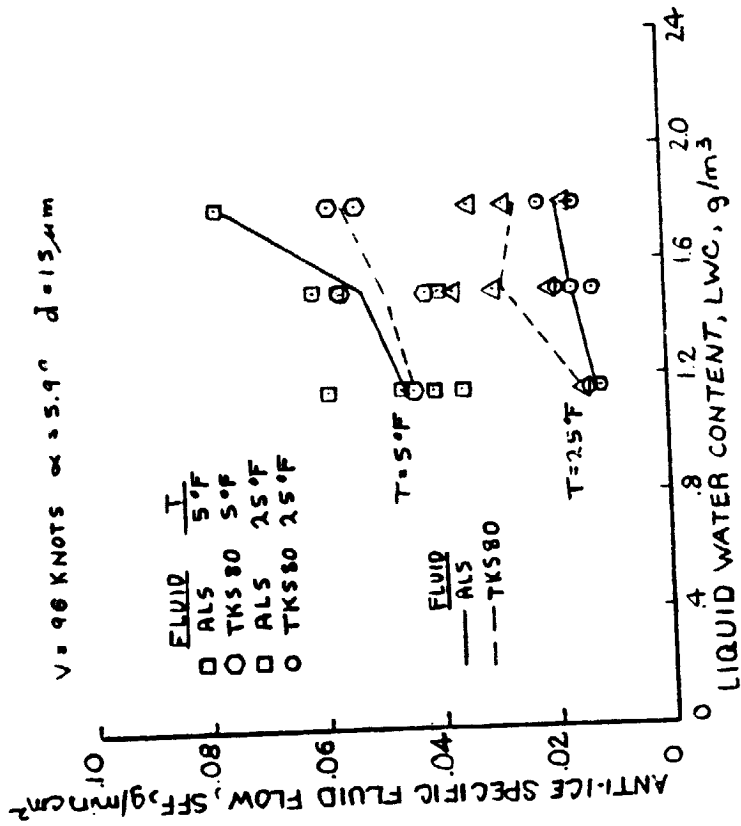
(d) V = 145 Knots, LWC = 0.80 g/m<sup>3</sup>, d = 11 microns

Figure 4.2.2. - (Continued.)

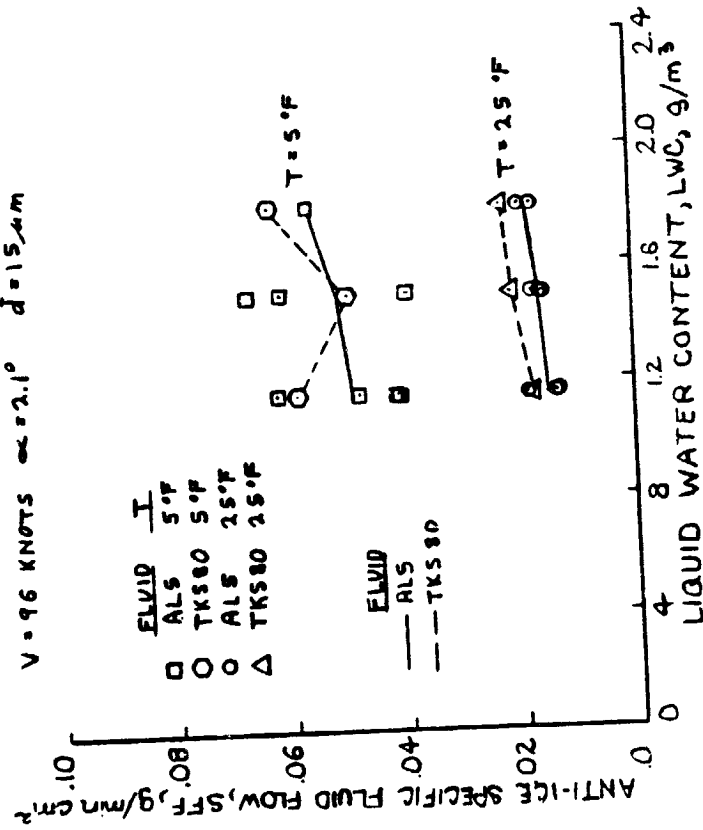


(e) V = 145 Knots, LWC = 1.16 g/m<sup>3</sup>, d = 15 microns (f) V = 145 Knots, LWC = 1.55 g/m<sup>3</sup>, d = 20 microns

Figure 4.2.2. - (Continued.)

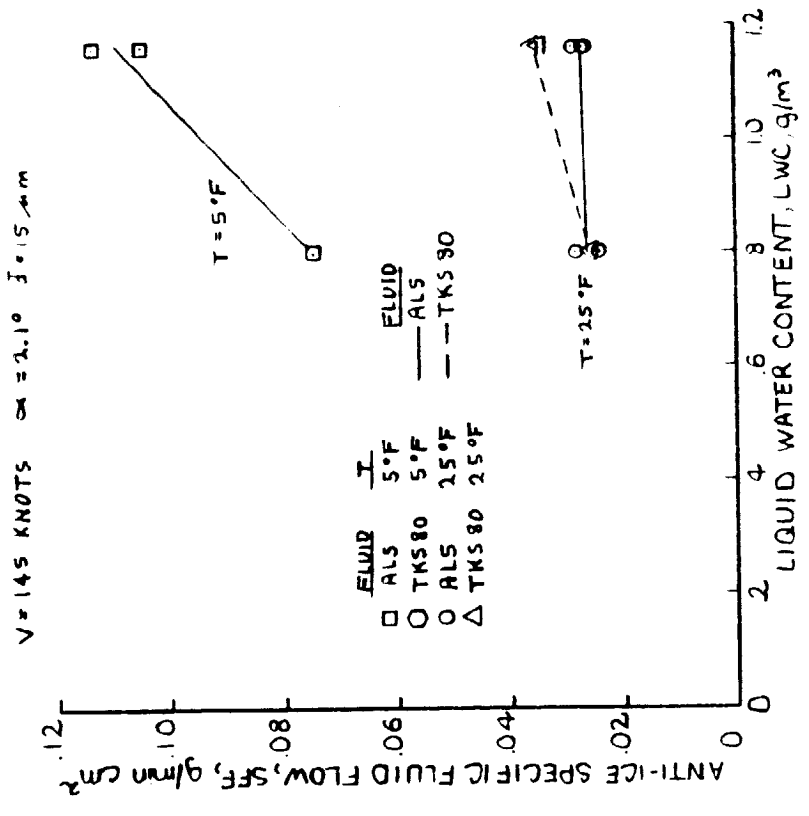


(b) V = 96 Knots, Angle of Attack = 5.9°, d = 15 microns

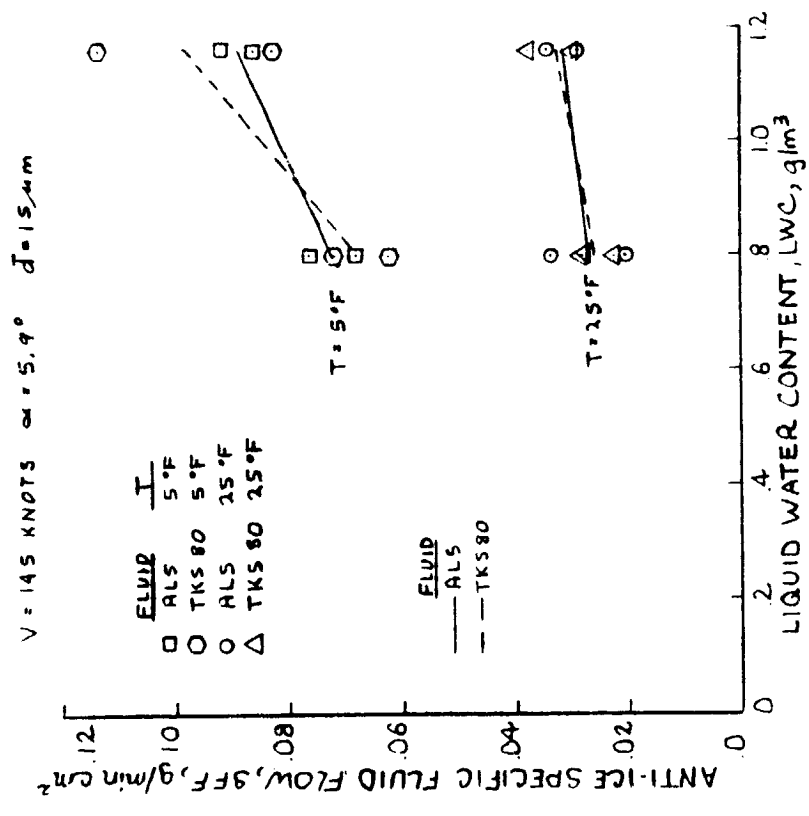


(a) V = 96 Knots, Angle of Attack = 2.1°, d = 15 microns

Figure 4.2.3. - Minimum Anti-Ice Fluid Flow Rates Versus Liquid Water Content on Wing Model A with Stainless Steel Mesh Panel.

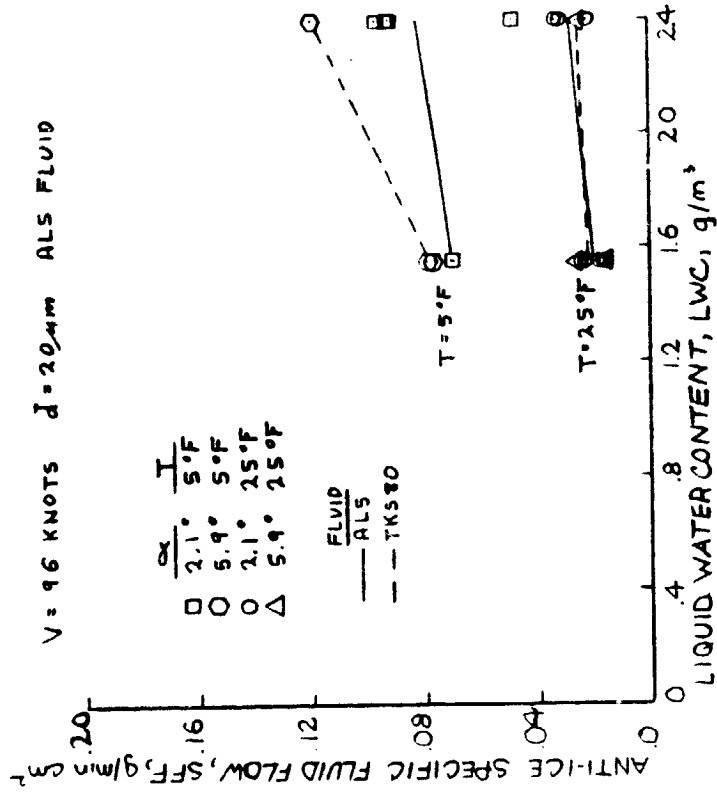


(d) V = 145 Knots, Angle of Attack, 2.1°,  
d = 15 microns



(c) V = 145 Knots, Angle of Attack = 5.9°,  
d = 15 microns

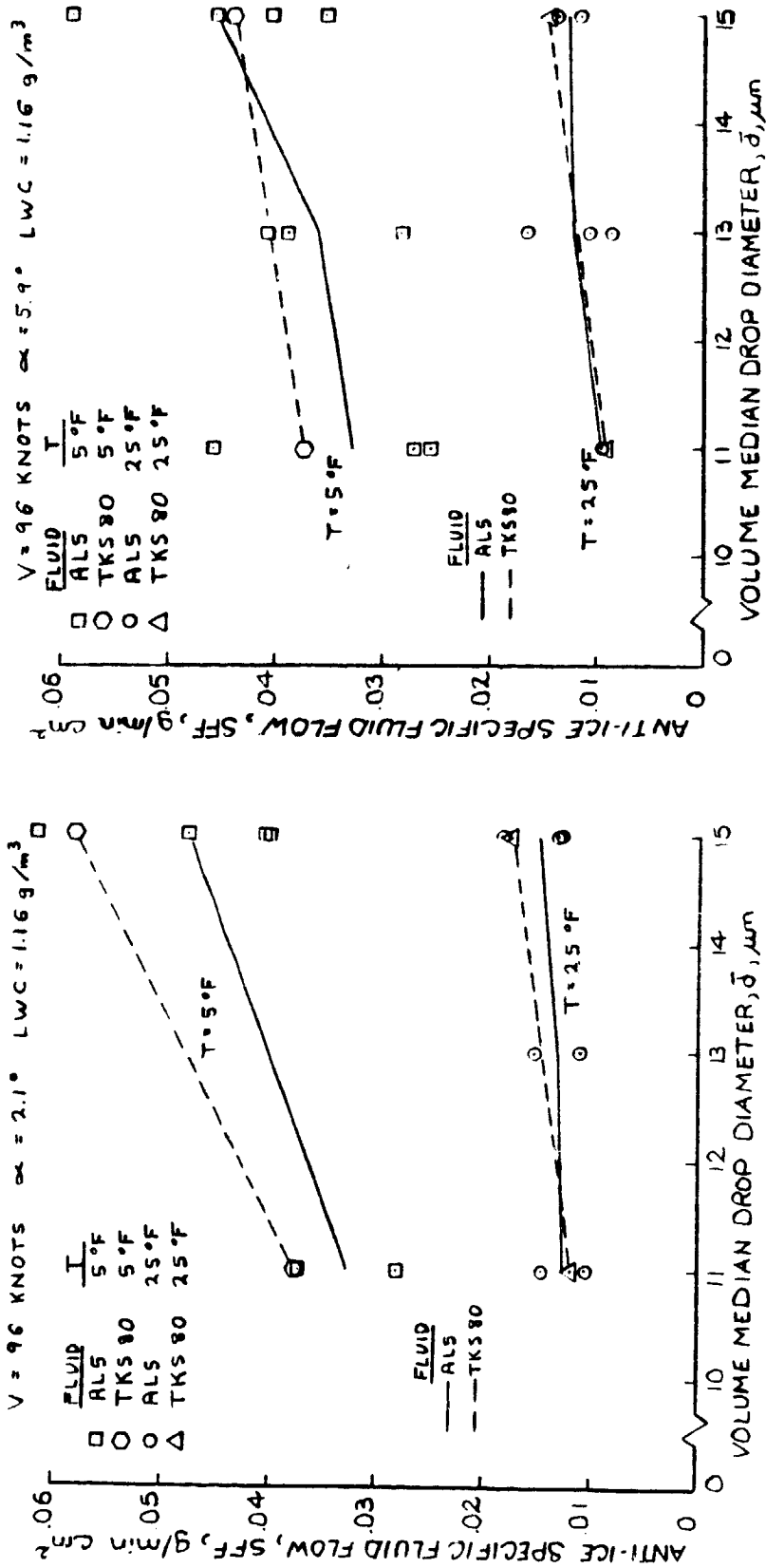
Figure 4.2.3. - (Continued.)



(e) V = 96 Knots, d = 20 Microns, ALS Fluid

Figure 4.2.3. - (Continued.)

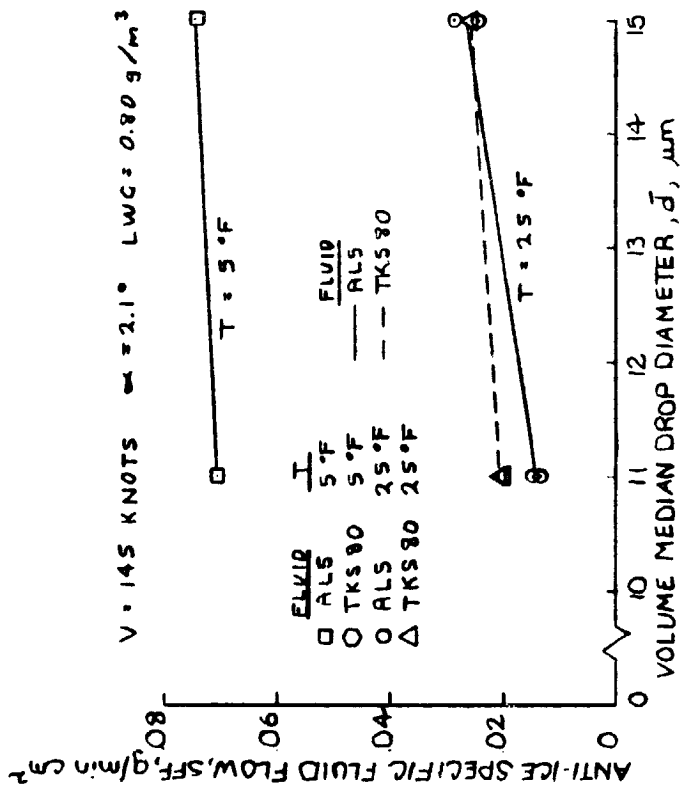
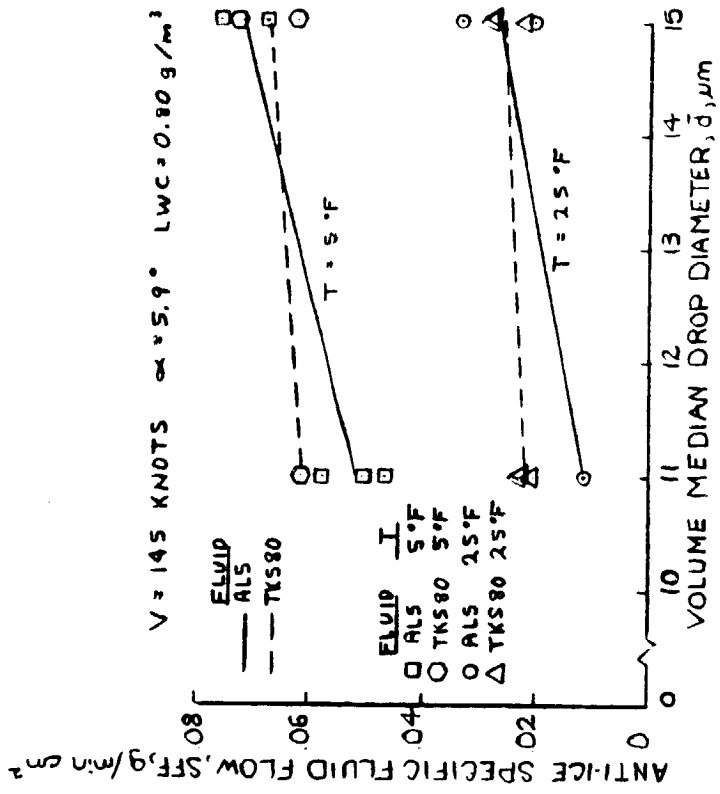
ORIGINAL PAGE IS  
OF POOR QUALITY



(a)  $V = 96$  Knots, Angle of Attack =  $2.1^\circ$ , LWC =  $1.16$  g/m<sup>3</sup>

(b)  $V = 96$  Knots, Angle of Attack =  $5.9^\circ$ , LWC =  $1.16$  g/m<sup>3</sup>

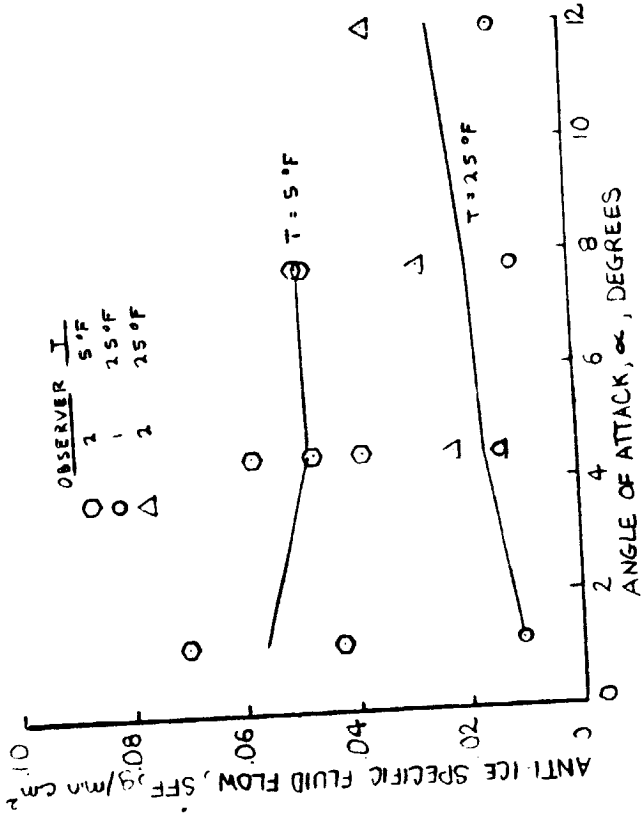
Figure 4.2.4. - Minimum Anti-Ice Fluid Flow Rates Versus Volume Median Drop Diameter on wing Model A with Stainless Steel Mesh Panel.



(c) V = 145 knots, Angle of Attack = 2.1°, LWC = 0.80 g/m<sup>3</sup>  
 (d) V = 145 knots, Angle of Attack = 5.9°, LWC = 0.80 g/m<sup>3</sup>

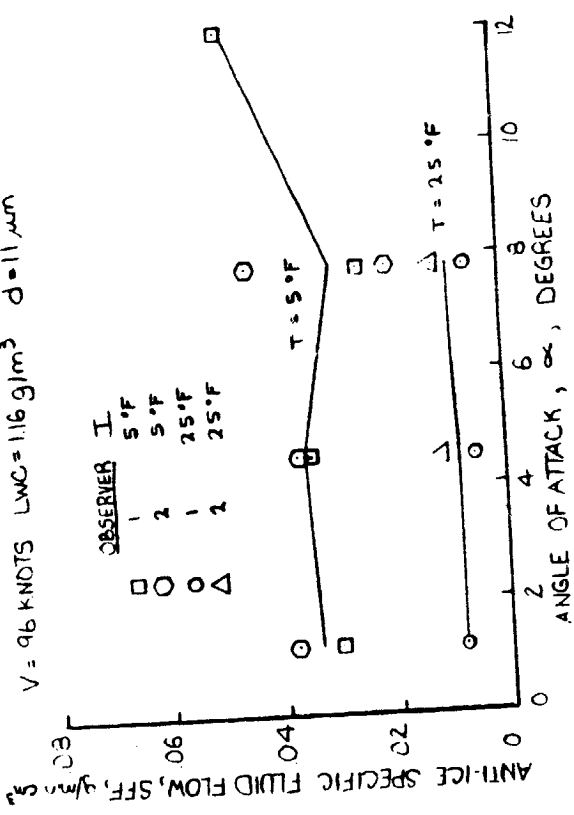
Figure 4.2.4. - (Continued.)

V = 96 KNOTS LWC = 116 g/m<sup>3</sup>  $\bar{d}$  = 15  $\mu$ m



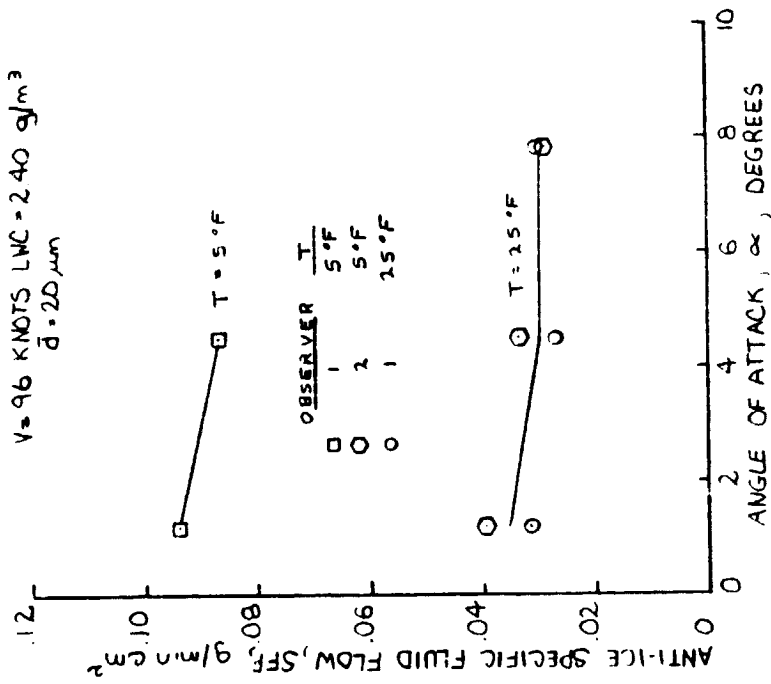
(b) V = 96 Knots, LWC = 1.16 g/m<sup>3</sup>, d = 15 microns

V = 96 KNOTS LWC = 116 g/m<sup>3</sup> d = 11  $\mu$ m

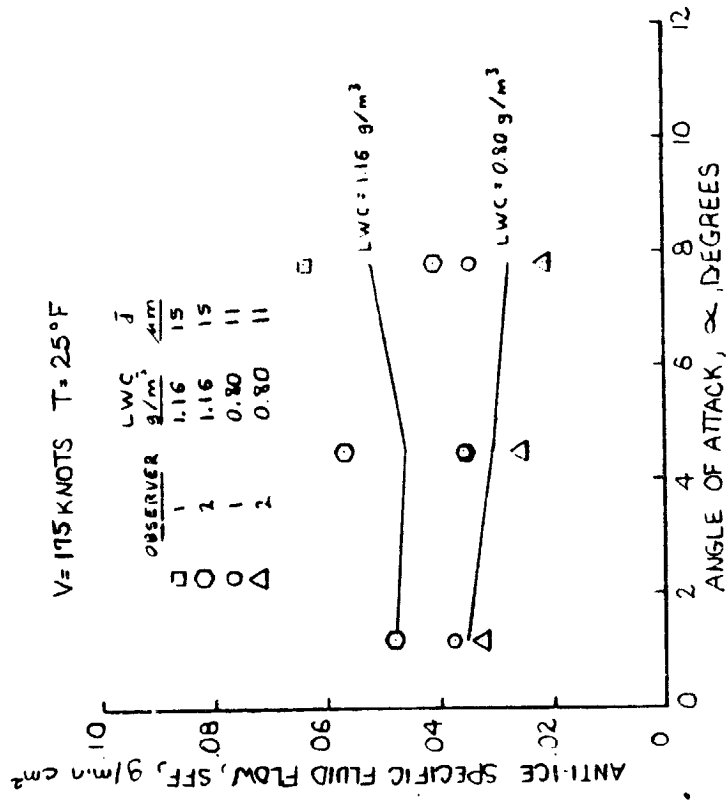


(a) V = 96 Knots, LWC = 1.16 g/m<sup>3</sup>, d = 11 microns

Figure 4.2.5. - Minimum Anti-Ice Fluid Flow Rates Versus Angle of Attack on Wing Panel Model B with Stainless Steel Mesh Panel.

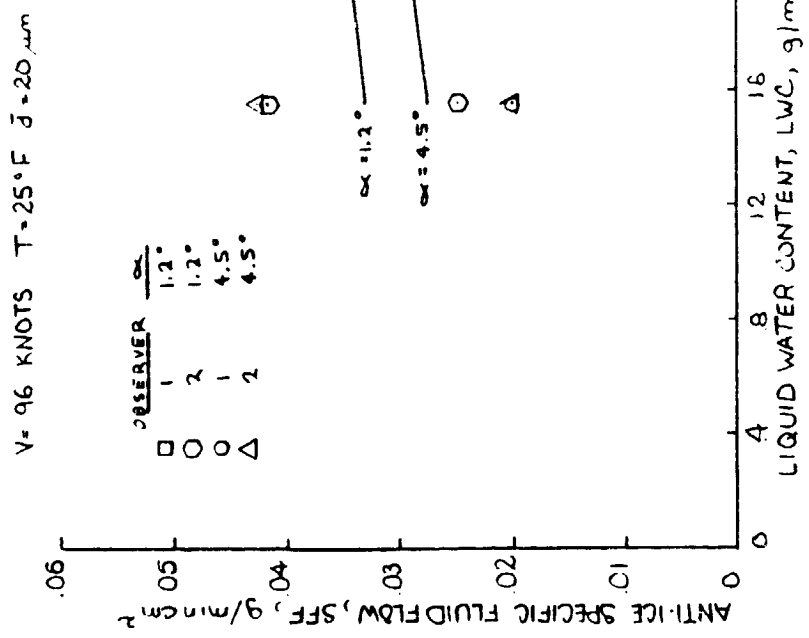


(c) V = 96 Knots, LWC = 2.40 g/m<sup>3</sup>, d = 20 microns

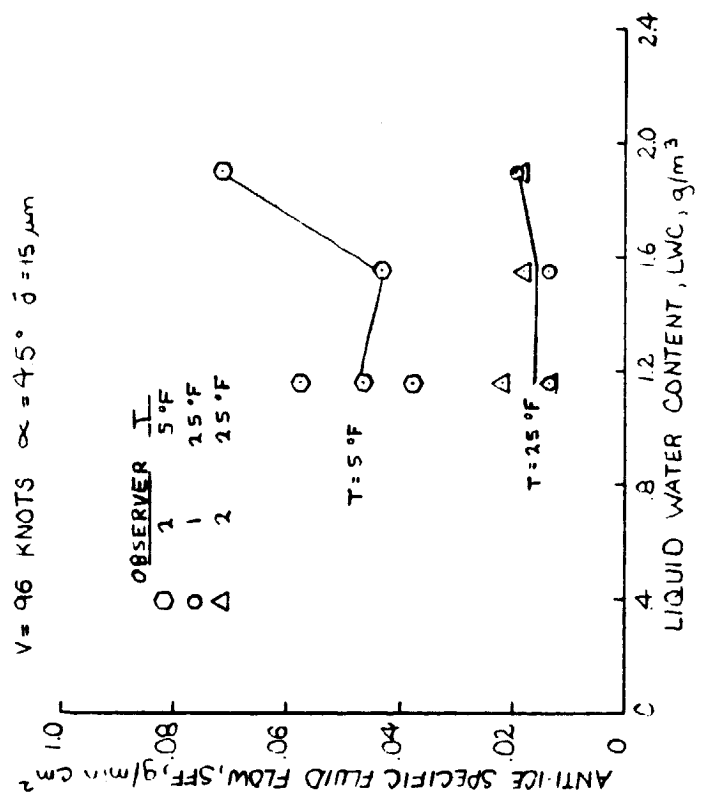


(d) V = 175 Knots, T = 25° F

Figure 4.2.5. - (Continued.)

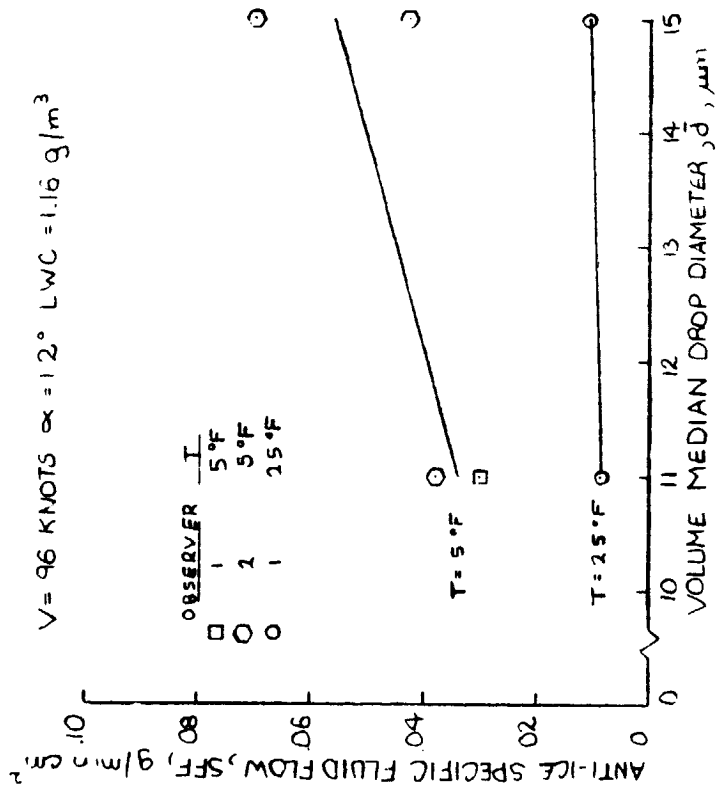


(a) V = 96 Knots, T = 25° F, d = 20 microns

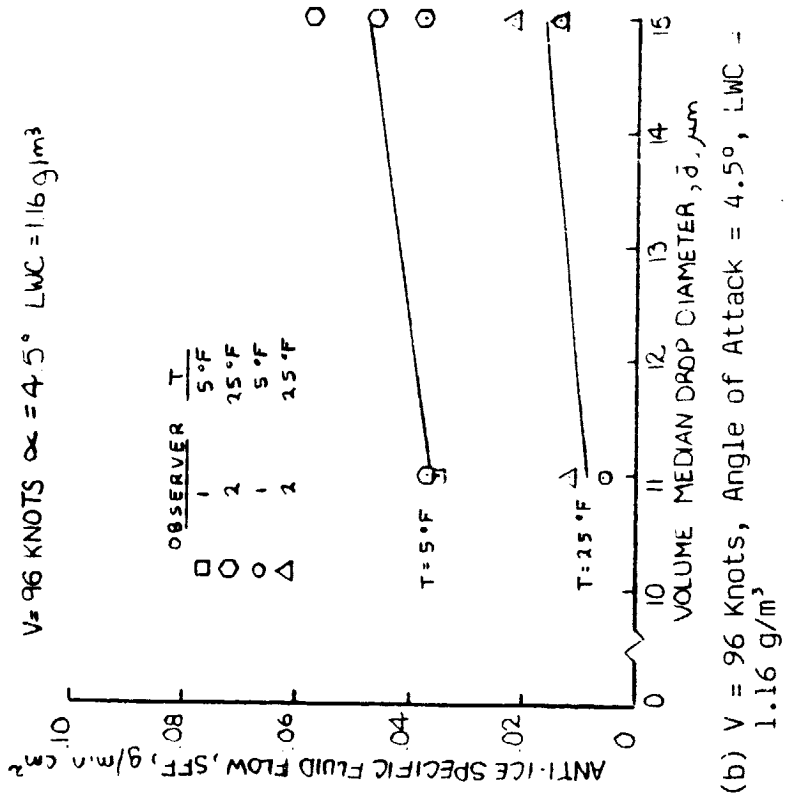


(b) V = 96 Knots, Angle of Attack = 4.5°, d = 15 microns

Figure 4.2.6. - Minimum Anti-Ice Fluid Flow Rates Versus Liquid Water Content on Wing Model B with Stainless Steel Mesh Panel.

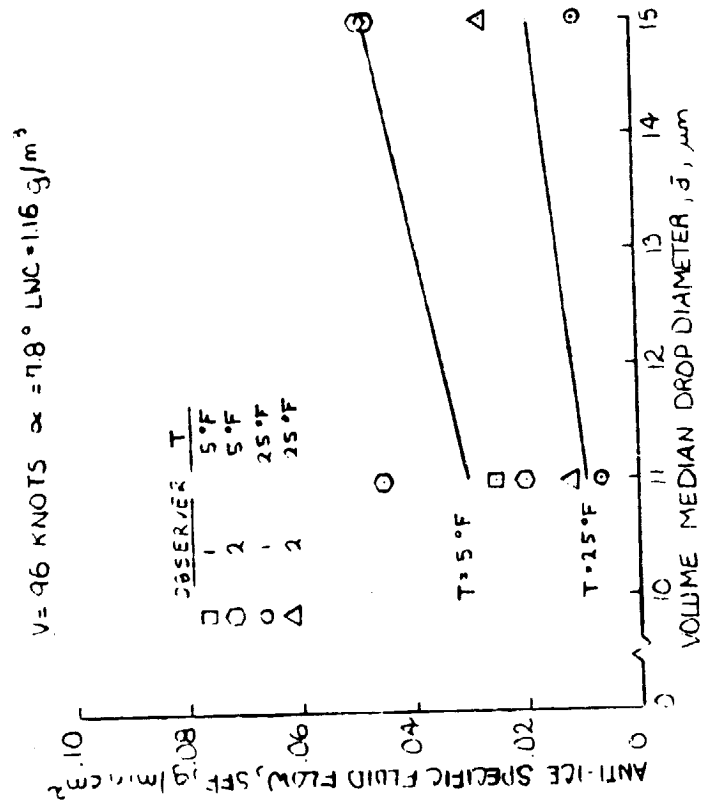
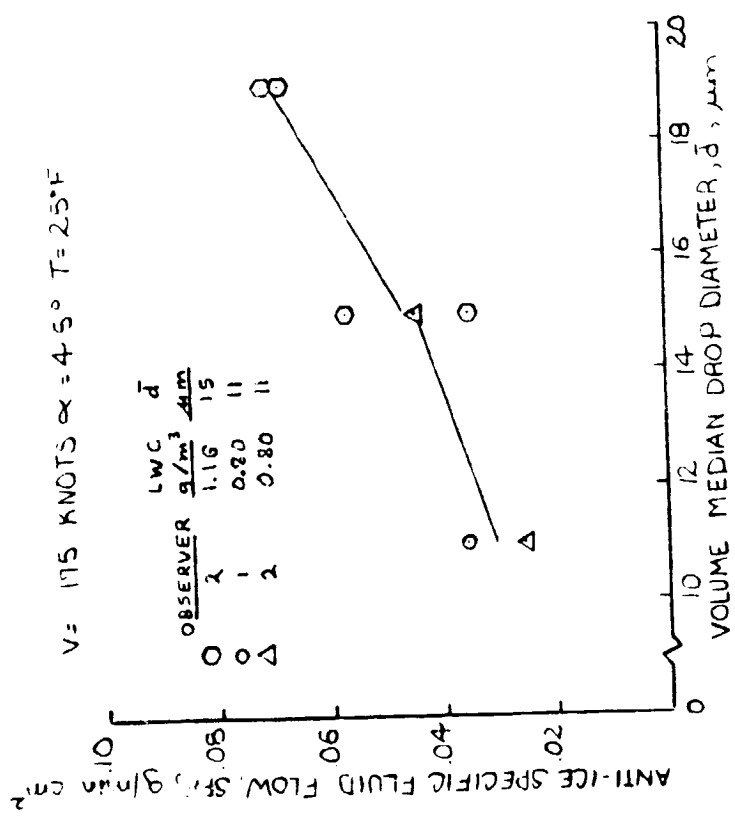


(a) V = 96 knots, Angle of Attack = 1.2°, LWC = 1.16 g/m<sup>3</sup>



(b) V = 96 knots, Angle of Attack = 4.5°, LWC = 1.16 g/m<sup>3</sup>

Figure 4.2.7. - Minimum Anti-Ice Fluid Flow Rates Versus Volume Median Drop Diameter on Wing Model B with Stainless Steel Mesh Panel.



(c) V = 96 knots, Angle of Attack = 7.8°, LWC = 1.16 g/m<sup>3</sup>  
 (d) V = 175 knots, Angle of Attack = 4.5°, T = 25° F

Figure 4.2.7. - (Continued.)

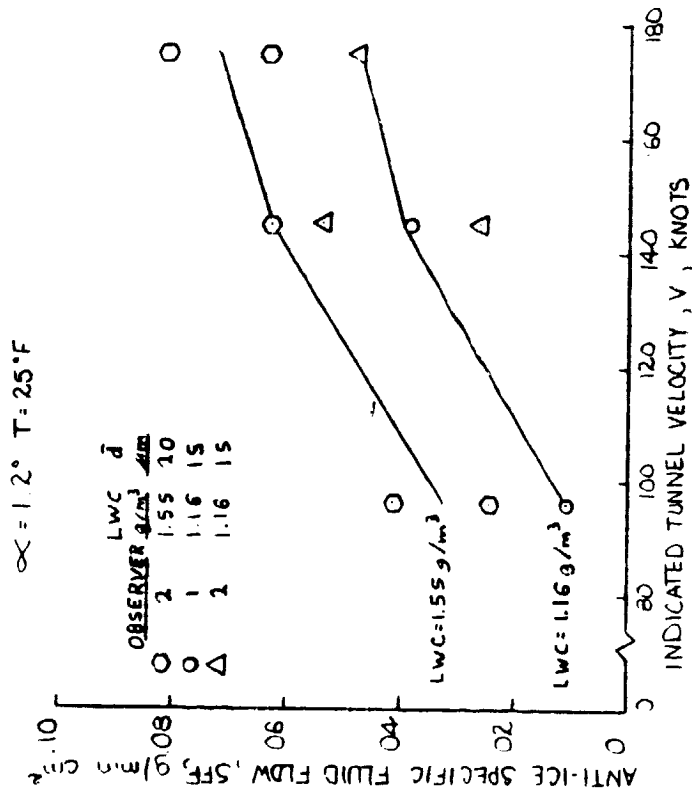
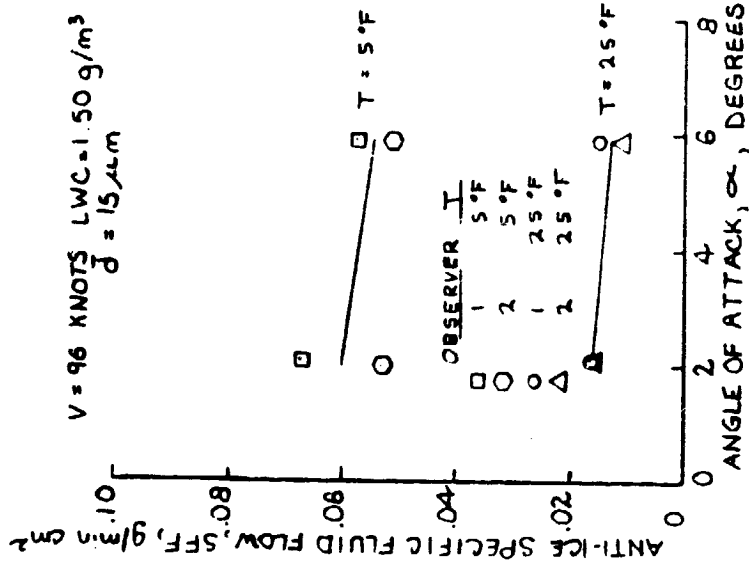


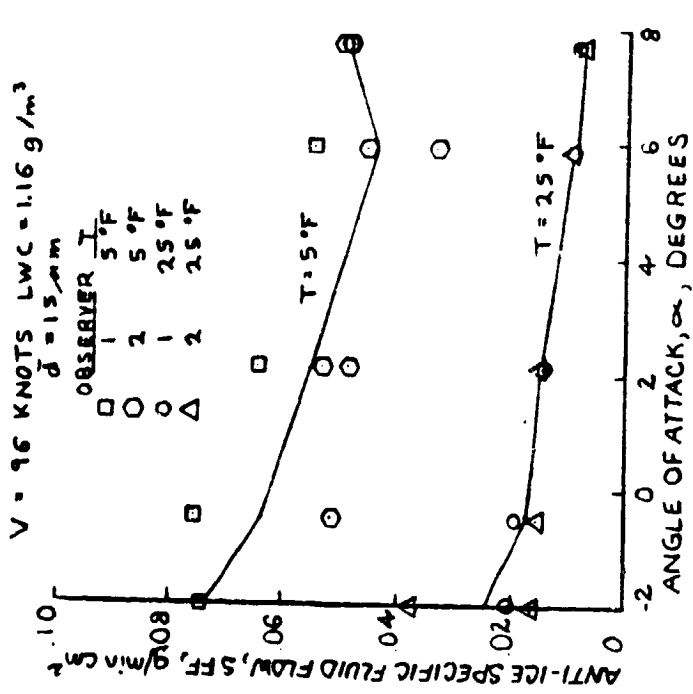
Figure 4.2.8. - Minimum Anti-Ice Fluid Flow Rates Versus Indicated Tunnel Velocity on Wing Model B with Stainless Steel Mesh Panel at an Angle of Attack =  $1.2^\circ$  and  $T = 25^\circ\text{F}$ .

#### 4.2.2 Titanium Panel

Tables A.4 and A.5 present the anti-ice flow rates determined with the new drilled titanium panel on Wing Model A. Table A.4 lists the runs determined by Observer 1. Table A.5 lists the runs determined by Observer 2. From these Tables, Figures 4.2.9, 4.2.10, and 4.2.11 were plotted showing the anti-ice fluid flow versus angle of attack, liquid water content, and volume median drop diameter. The anti-ice fluid flow is independent of angle of attack as long as the stagnation location is within the center 50 to 75 percent of the active porous region of the leading edge panel. Figure 4.2.12 presents a comparison of the required flow rate for anti-icing using the stainless steel panel with the flow rate required when using the titanium panel. There appears to be no significant difference in the required flow rate for anti-icing between the two panels. The points lying outside of the 25% boundary lines are an indication of the scatter in the experimental data.

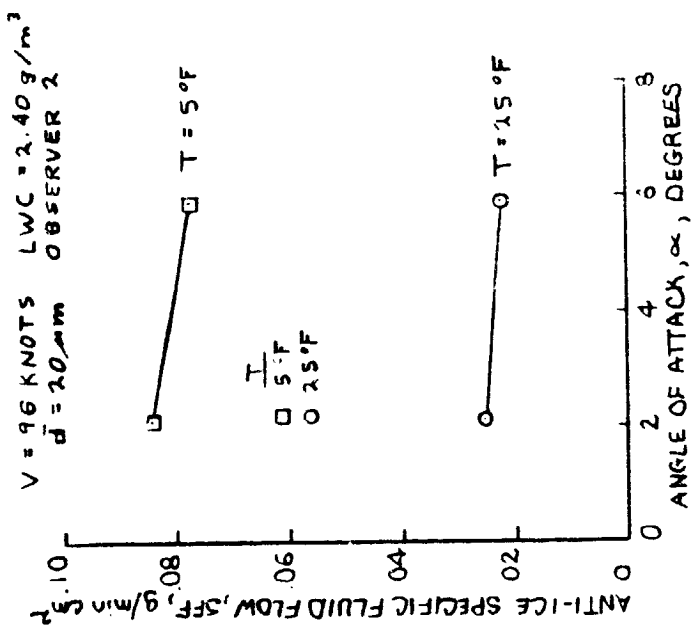


(b) V = 96 knots, LWC = 1.50 g/m<sup>3</sup>, d = 15 microns

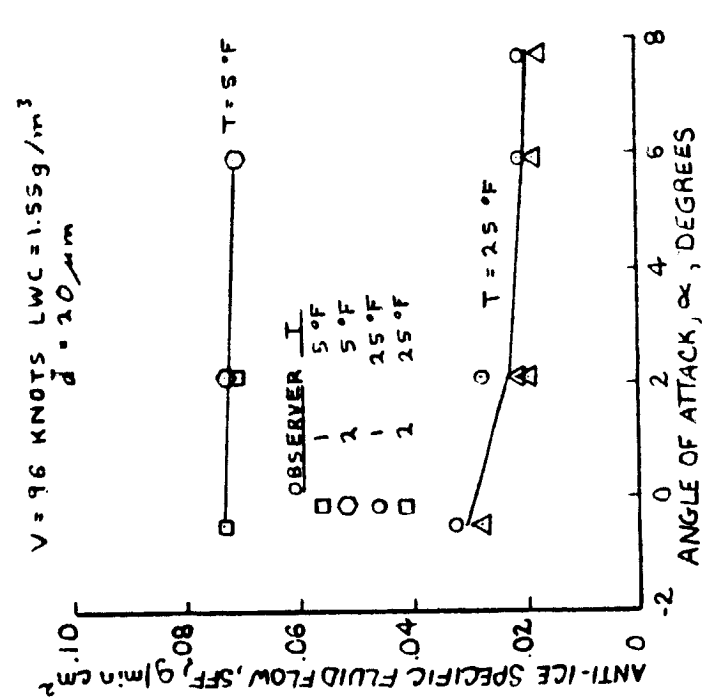


(a) V = 96 knots, LWC = 1.16 g/m<sup>3</sup>, d = 15 microns

Figure 4.2.9. - Minimum Anti-Ice Fluid Flow Rates Versus Angle of Attack on Wing Model A with Titanium Panel.

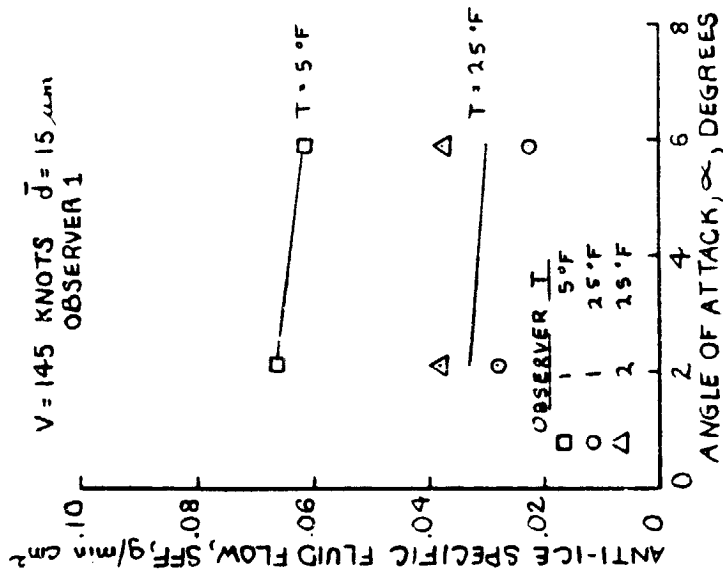


(d) V = 96 Knots, LWC = 2.40 g/m<sup>3</sup>, d = 20 microns, Observer 2

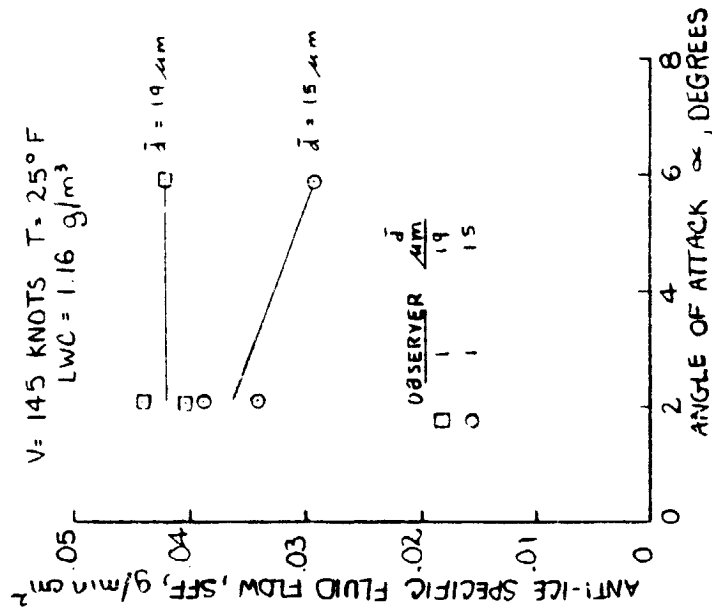


(c) V = 96 Knots, LWC = 1.55 g/m<sup>3</sup>, d = 20 microns

Figure 4.2.9. - (Continued.)

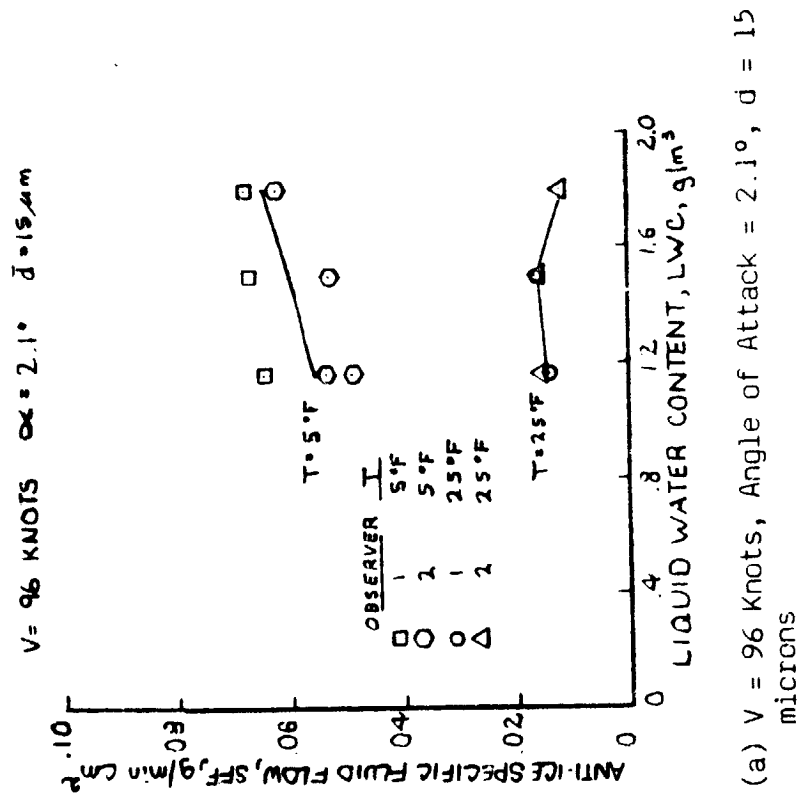
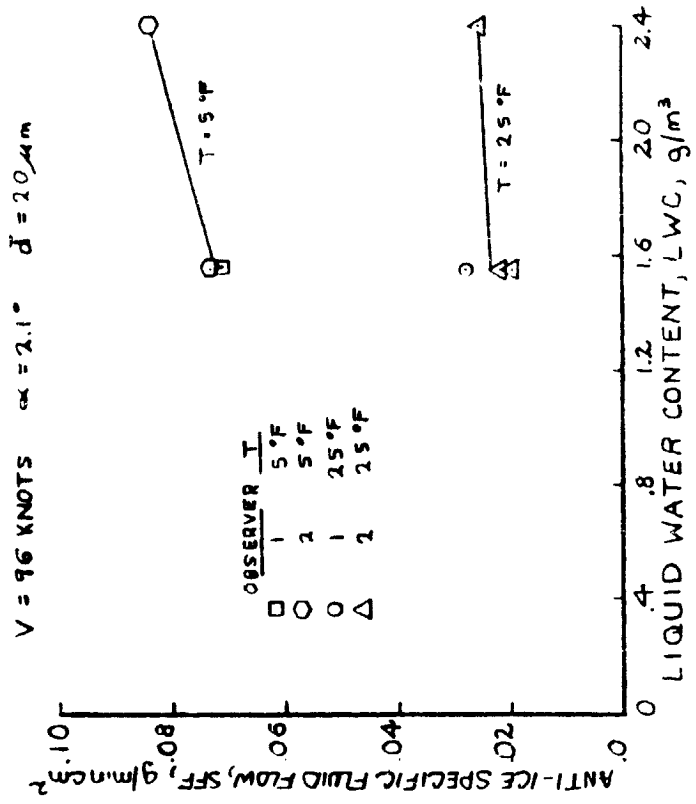


(e) V = 145 Knots, d = 15 microns, Observer 1



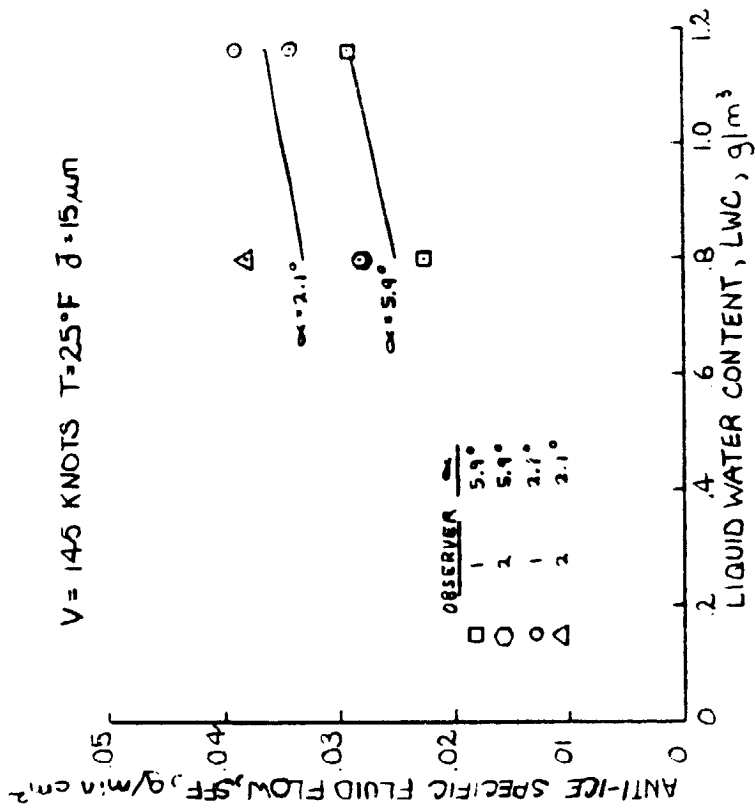
(f) V = 145 Knots, T = 25°F, LWC = 1.16 g/m<sup>3</sup>

Figure 4.2.9. (Continued.)



(a) V = 96 Knots, Angle of Attack =  $2.1^\circ$ ,  $d = 15$  microns  
 (b) V = 96 Knots, Angle of Attack =  $2.1^\circ$ ,  $d = 20$  microns

Figure 4.2.10. - Minimum Anti-Ice Fluid Flow Rates Versus Liquid Water Content on Wing Model A with Titanium Panel.



(c) V = 145 knots, T = 25° F, d = 15 microns

Figure 4.2.10. - (Continued.)

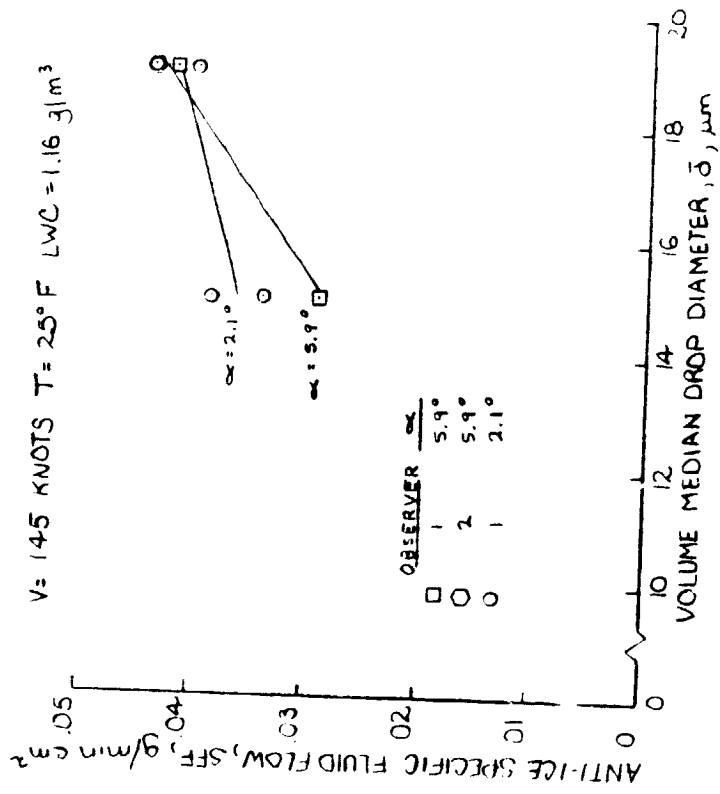


Figure 4.2.11. - Minimum Anti-Ice Fluid Flow Rates Versus Volume Median Drop Diameter on Wing Model A with Titanium Panel at V = 145 Knots, T = 25° F, LWC = 1.16 g/m<sup>3</sup>.

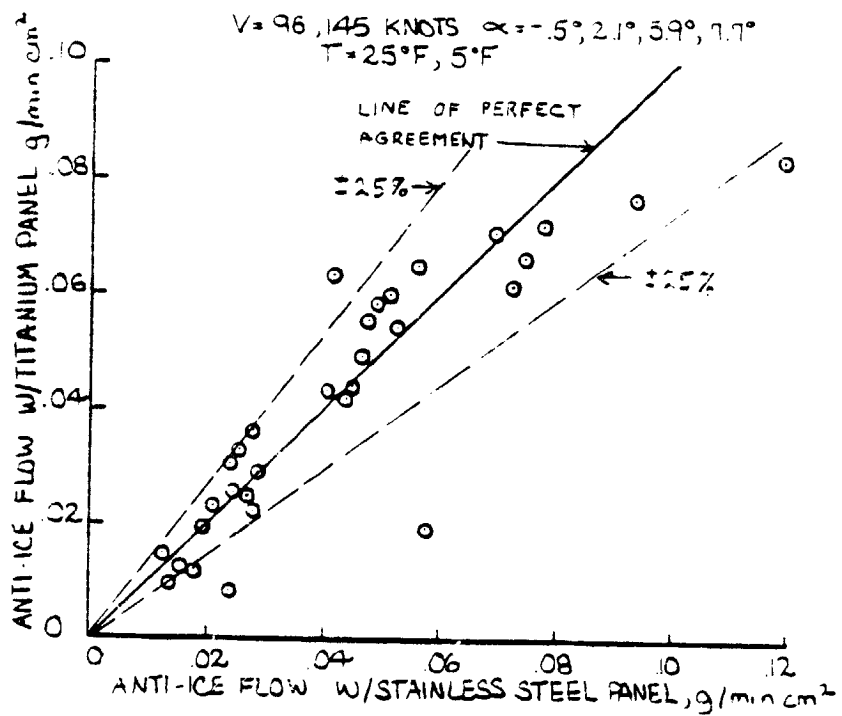


Figure 4.2.12. - Comparison of Anti-Ice Flow Rates Between Stainless Steel Mesh Panel and Titanium Panel on Wing Model A.

#### 4.2.3 Composite

A composite panel was also tested on Wing Model B. However, after only two days of evaluation, the wind tunnel tests were cancelled. Overall, the results obtained agreed with those from the original composite panel tests as reported in ref. 4. The flow rates required for anti-icing were two to three times higher than those required when using the stainless steel or titanium panel.

These higher flow rates were the result of the net porosity of the panel being insufficient to distribute the flow of glycol uniformly in a chordwise direction. As the porosity of a distributing panel increases, the internal back pressure decreases. With low pressurization, the flow of glycol does not exude uniformly in a chordwise direction against an external aerodynamic pressure gradient. While the required glycol flow rate is the highest near the stagnation location, the actual glycol flow rate was the lowest there.

Several other problems were also experienced with the composite panel. First, significant differences were noted between each of three independent sections. At a given setting, the resulting back pressure of each section was different. Second, the glycol flow rate varied from one region to the next within the same section. At one location, the flow rate was high, but at another location the flow rate was much lower. Third, the flow of glycol was able to

leak internally from one section to the next. Since the wing section was mounted vertically in the wind tunnel, a portion of the glycol pumped to the top panel section would slowly drain internally to a lower section before exuding. The combination of these problems caused the test series to be cancelled.

It is believed that most of these problems are not a result of the external skin being a composite. Instead, it is felt that the problems are associated with the design, manufacturing, and quality control of the porosity of the panel which is primarily controlled by the internal filter material, polyvinyl flouride. Because of the significant weight savings and special applications for a composite, a further effort should be undertaken to develop a usable composite panel.

#### 4.3 Deice

Deicing is an alternative operating mode for the fluid ice protection system. This mode would be required if ice were to form prior to turning the system on. Results of deicing tests on Wing Model A with the stainless steel mesh panel are shown in Figures 4.3.1 a and b. These tests were conducted at a velocity of 145 knots, angle of attack of 2.1 degrees, and after a 5 minute icing spray. The elapsed times required to shed the accreted ice cap are plotted versus the flow of glycol in terms of the percent of anti-

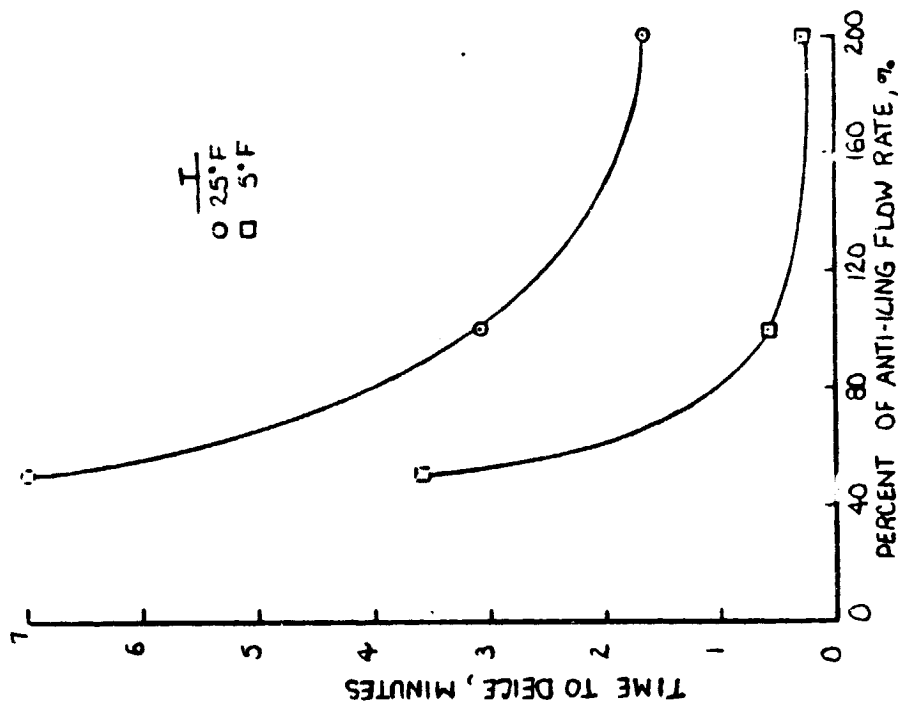
icing flow required at the respective icing condition.

An ice accretion formed at 5 degrees F required less time to shed than an accretion formed at 25 degrees F. This is especially prominent in Figure 4.3.1a with a LWC =  $0.80 \text{ g/m}^3$  and drop size = 11 microns. An explanation is that at 25 degrees F glaze ice is formed, which is accompanied by runback icing, thus a wide ice cap. At 5 degrees F, the ice freezes on impact with the wing, resulting in a narrower ice cap. The wider the ice cap, the more ice at the interface which must be melted before a shed is likely.

At a glycol flow rate of 50 % of that required for anti-icing it was necessary to make a small change in the angle of attack to facilitate a shed at the elapsed times shown in Figure 4.3.1. Shed times of three minutes or less are possible for the icing conditions shown with a flow rate equal to that required for anti-icing. Only marginal improvement in shed times are realized as the flow is increased to 200% of the anti-ice flow.

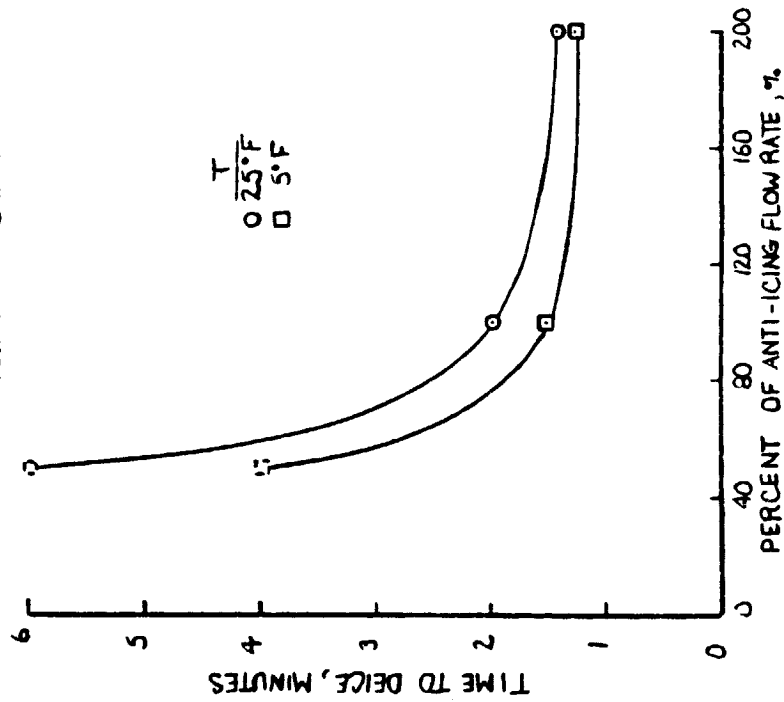
Figure 4.3.2 is a sequence of photographs from ref. 1 showing the progressive shedding of a typical ice cap. Note that by the time the leading edge ice is shed, the runback of glycol along the wing surface has substantially removed the frost and ice particles behind the active portion of the leading edge. Operating in a deice mode may not be feasible if the aircraft can not tolerate the possible increase in drag and decrease in lift associated with the accreted ice prior to shedding.

V = 145 KNOTS  $\alpha = 2.1^\circ$  LWC = 0.80 g/m<sup>3</sup>  $\bar{d} = 11 \mu\text{m}$   
 ICING TIME = 5 min.



(a) LWC = 0.80 g/m<sup>3</sup>, d = 11 microns

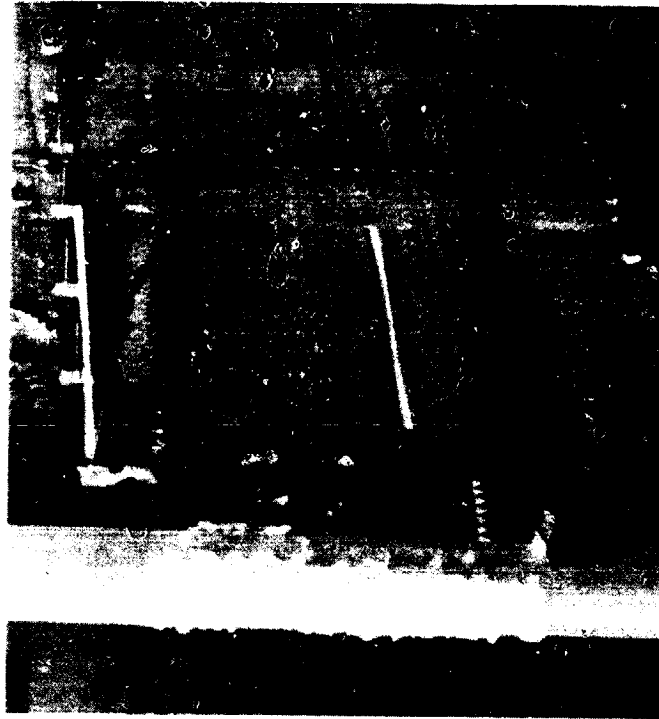
V = 145 KNOTS  $\alpha = 2.1^\circ$  LWC = 1.16 g/m<sup>3</sup>  $\bar{d} = 15 \mu\text{m}$   
 ICING TIME = 5 min.



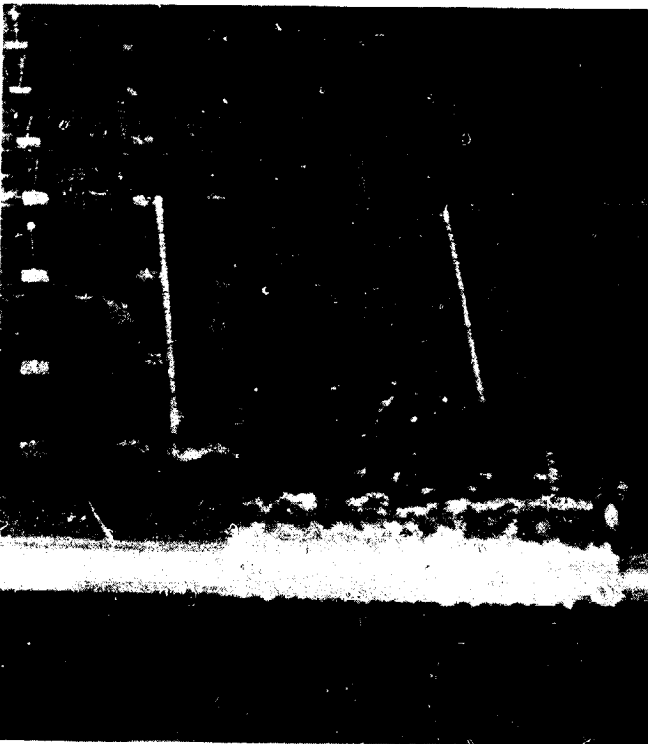
(b) LWC = 0.80 g/m<sup>3</sup>, d = 15 microns.

Figure 4.3.1. - Effect of Fluid Flow on Time to Deice at V = 145 Knots, Angle of Attack = 2.1°, Icing Time = 5 min.

ORIGINAL PAGE IS  
OF POOR QUALITY



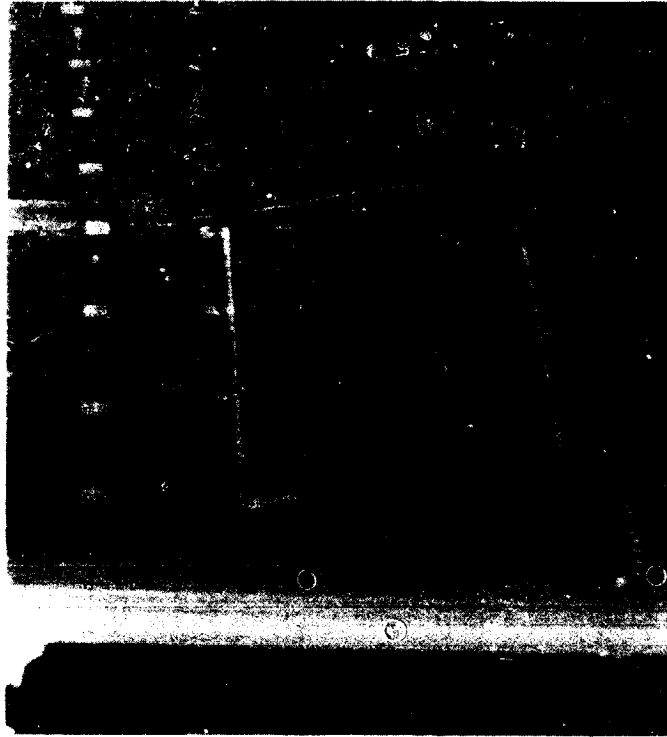
(a) After 0 Minutes of Deicing



(b) After 2 Minutes of Deicing

Figure 4.3.2. - Deice Time Sequence for an Ice Accretion Formed at  $V = 96$  Knots,  $LWC = 2.40 \text{ g/m}^3$ ,  
Angle of Attack =  $7.8^\circ$ ,  $T = 25^\circ \text{ F}$ , and Icing Time = 10 Minutes.

ORIGINAL PAGE IS  
OF POOR QUALITY



(d) After 4 Minutes of Deicing



(c) After 3 Minutes of Deicing

Figure 4.3.2. - (Continued.)

#### 4.4 Fluid Type Comparison

Since two fluids are commercially available for use with the fluid ice protection system, it was felt desirable to test both fluids during part of the research to determine any differences in required flow rates for anti-icing. Both fluids, AL5 and TKS80, were tested on Wing Model A with the stainless steel mesh panel. Thirty four icing conditions, at 5 and 25 degrees F, were tested using both fluids. The fluid flow required for anti-icing using the AL5 fluid,  $SFF_1$ , was compared with the fluid flow required when using the TKS80 fluid,  $SFF_2$ , as presented in Table III.

The results indicate that at the warm temperature, 25 degrees F, there is little difference between the two fluids over the 19 runs compared at 96 and 145 knots. However, at the cold temperature of 5 degrees F, approximately 20 percent higher flow rate is required when using the TKS80 fluid compared to the AL5 fluid. This occurs at both 96 and 145 knots. This difference cannot be directly explained by observing the freezing temperature profiles of the two fluids shown in Figure 2.8. Both fluids appear to have nearly identical freezing temperature characteristics.

Table III: Comparison of Glycol Based Freezing Depressant Solutions

V Knots	T deg. F	Runs Compared (runs)	$\frac{(SFF_2 - SFF_1)100}{(SFF_1)(\text{no. of runs})}$
96 & 145	25	19	21
96 & 145	5	15	1

## 5.0 Anti-Ice Flow Rate Prediction Techniques

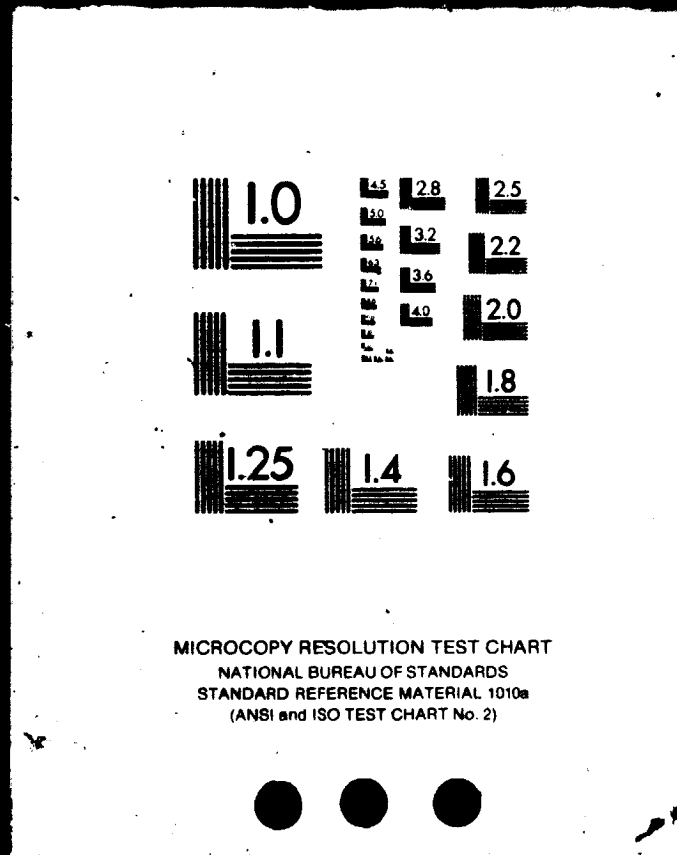
### 5.1 ADS-4 Method

Prior to 1983, the only published method of predicting anti-ice flow rates was that found in "The Engineering Summary of Airframe Icing Technical Data (ADS-4)" (ref. 6). This empirical method is based on the calculation of a glycol flow rate from the entire porous panel sufficient to lower the overall collection of water to a temperature equal to what is referred to as the datum temperature. This method does not take into account the distribution of the local impingement efficiency. The datum temperature has been used to represent the temperature of an unheated surface in icing. This method was not developed specifically for wing sections with porous leading edge panels. In fact, ref. 6 compares the predicted flow rates with experimental flow rates from wind tunnel tests using a

2 OF 2

N86-27186

UNCLAS



spray nozzle to distribute glycol on a radome (ref. 7).

As mentioned, this empirical method is based on the calculation of the overall collection efficiency,  $E_m$ . This collection is defined as the ratio of water collected to the maximum possible water catch. This is computed by the equation  $E_m = (Y_u - Y_l)/h$  where  $Y_u$  is the starting ordinate of the upper water droplet tangent trajectory to the airfoil,  $Y_l$  the starting ordinate of the lower tangent trajectory, and  $h$  is the projected height of the airfoil.

In reference 6  $E_m$ ,  $Y_u$ , and  $Y_l$  are graphically correlated with a dimensionless inertia parameter,  $Ko$ , for a variety of airfoil sections. However, only a small portion of the airfoils in use today are included. Thus, a matching procedure is necessary to find an airfoil section that has been correlated that closely matches the airfoil of interest. It is often necessary to make extrapolations and assumptions when determining the values of  $E_m$ ,  $Y_l$ , and  $Y_u$  throughout the procedure listed in ref. 6. These approximations will in turn affect the accuracy of the predicted anti-ice flow rate.

Since the publication date of ref. 6, computer codes have become available for computing limiting tangent trajectories, overall collection efficiencies, and the local impingement efficiency distribution (Fig. 5.1). A program developed by Ohio State University under a grant from NASA LeRC (ref. 8) was used to calculate the values of  $E_m$ ,  $Y_l$ ,  $Y_u$ , and  $h/c$ . This modified prediction

method, as outlined below, will be referred to as the ADS-4 method. Appendix D contains a listing of the computer program used to calculate the ADS-4 predicted flow rates presented in this report.

Step 1: Calculate the overall collection efficiency factor,  $E_m$ , as a function of

- (1) airfoil shape
- (2) airspeed
- (3) air density
- (4) drop diameter
- (5) angle of attack

using a 2-D water droplet trajectory code.

Step 2: Calculate the rate of water impingement on the airfoil from the equation

$$M_w = .0031 \frac{(V)(LWC)(E_m)(h/c)}{(S_u - S_l)} \quad (1)$$

with LWC in  $g/m^3$ , V in knots, and  $M_w$  in  $g/min \text{ cm}^2$ .

Step 3: Determine the glycol mass fraction, G, required to produce a solution with a freezing temperature equal to the datum temperature. The datum temperature, as defined in ref. 6, represents the temperature of an unheated surface in icing, described as the "wet air boundary layer" temperature. This temperature is a function of

airspeed, ambient temperature, and altitude. Reference 6 contains several plots at various altitudes showing the relationship between the datum temperature with the ambient temperature and velocity.

Step 4: Calculate the fluid flow required to achieve the glycol mass fraction,  $G$ , given the water catch rate,  $M_w$ , by the equation

$$SFFe = \frac{(G)(M_w)}{(X - G)} \quad (2)$$

where  $X$  is the initial glycol plus propanol mass fraction of the solution as it is pumped through the porous panel.

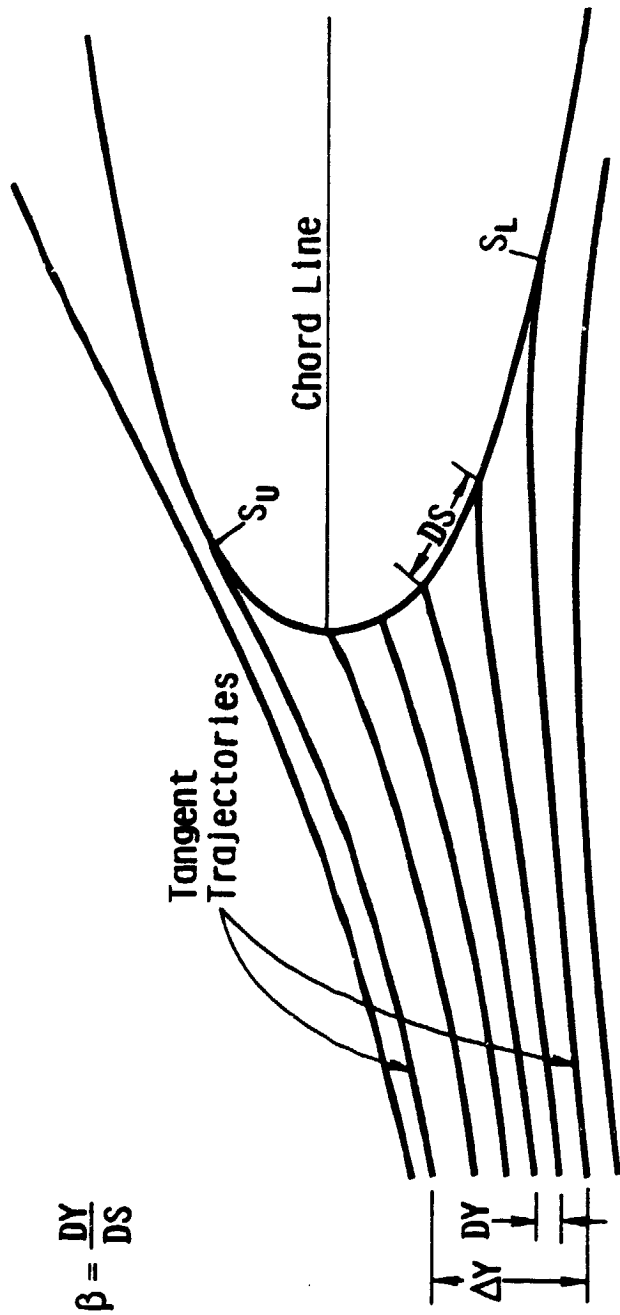


Figure 5.1. - Computer Simulation of Water Droplet Trajectories Impacting Airfoil.

## 5.2 Analytical Method

An analytical method of predicting anti-ice flow rates was first presented in reference 9. This method was developed after the original IRT tests in 1980 (ref. 1) of the fluid system using the stainless steel mesh panel on Wing Model B. A basic assumption of this method is that the minimum glycol fluid flow rate required for anti-icing results in a freezing temperature of the glycol water mixture equal to the average temperature between ambient and total temperature at the location of the maximum impingement efficiency. This average temperature is an arbitrary, empirical assumption applicable when testing at velocities less than 175 knots. Further research is needed to determine if this assumption is valid at velocities above 175 knots. The local impingement efficiency (rate of water catch) varies in a chordwise direction, with the maximum efficiency located close to the stagnation location. This assumption was verified experimentally by noting that as the glycol flow rate is reduced from a flow rate in excess of that required for anti-icing, ice particles first begin to form at the stagnation location. However, at an angle of attack with a stagnation location close to the edge of the porous region this assumption is no longer valid.

Any reasonably accurate 2-D water droplet trajectory program can be used to calculate the local maximum impingement efficiency,

$e_{\max}$ . However, the calculation of  $\beta_{\max}$  is not as straight forward as the calculation of  $E_m$  used in the ADS-4 method. The value of  $\beta_{\max}$  is determined from the maximum slope of a curve fit to the final water drop trajectory positions, S and Y, on the airfoil as shown in Figures C.1 - C.3 of Appendix C. These Figures present the trajectory positions and the local impingement efficiency distribution for three different icing conditions with a different number of impacting trajectories at each condition. The range of  $\beta_{\max}$  for different numbers of trajectories varies from one icing condition to the next.

The analytical method is presented here in a step-by-step procedure. Appendix D contains a listing of a computer program used to predict the analytical flow rates presented in this report.

Step 1: Calculate the maximum local collection efficiency factor,  $\beta_{\max}$  as a function of;

- (1) airfoil shape
- (2) airspeed
- (3) air density
- (4) drop diameter
- (5) angle of attack

using any reasonably accurate 2-D water droplet trajectory computer code.

Step 2: Calculate the water catch rate,  $M_w$ , by the equation

$$M_w = .0031 * 3_{\max} (LWC)(V) \quad (3)$$

with LWC in  $g/m^3$ ,  $V$  in knots, and  $M_w$  in  $g/min\ cm^2$ .

Step 3: Determine the glycol mass fraction,  $G$ , required to produce a solution with a freezing temperature equal to the average between the ambient and the stagnation temperatures. Normally this average temperature is within 2 degrees F of the datum temperature used in the ADS-4 method.

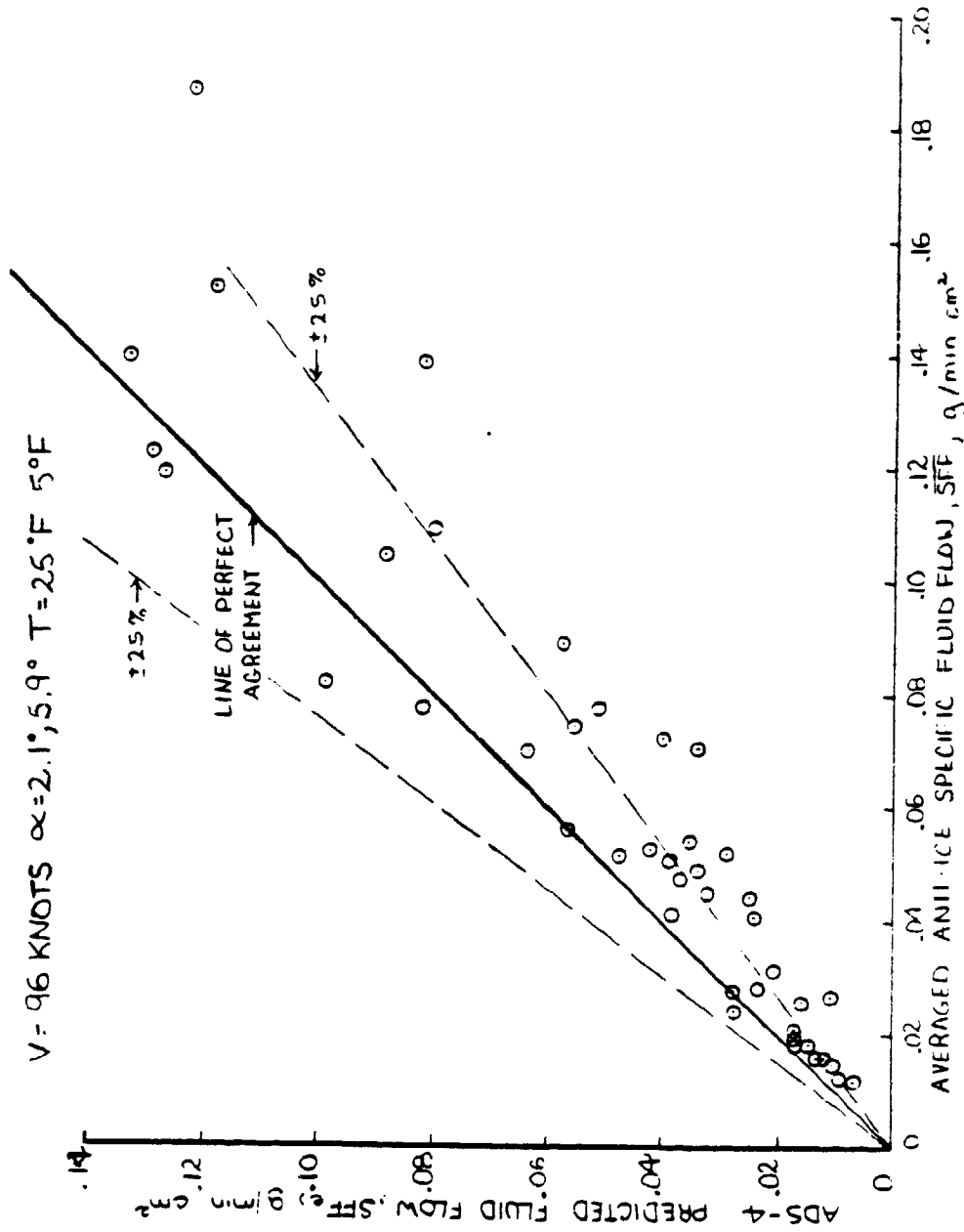
Step 4: Calculate the fluid flow required to achieve the glycol plus propanol mass fraction,  $G$ , given a water catch rate,  $M_w$ , by the equation

$$SFFa = \frac{(G)(M_w)}{(X - G)} \quad (4)$$

where  $X$  is the initial glycol plus propanol mass fraction of the glycol solution that is supplied to the panel.

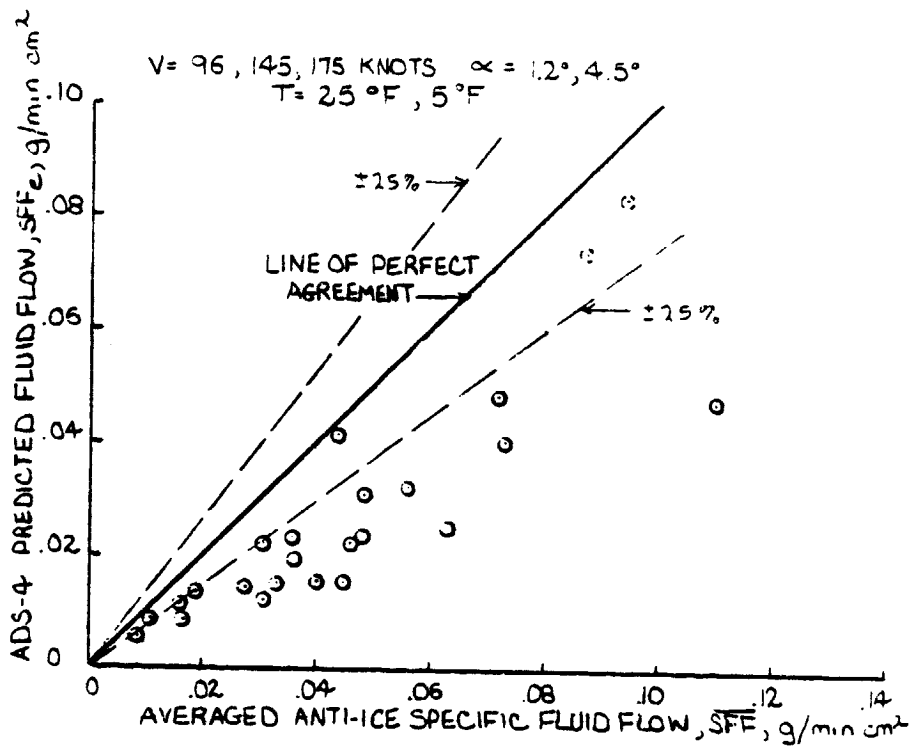
### 5.3 Comparison with Experimental Data

Appendix B contains tables of the anti-ice averaged experimental flow rates and the corresponding ADS-4 and analytical predicted flow rates. Included in the tables are the airfoil projected height, tangent trajectory limits, overall collection efficiency, and the maximum impingement efficiency. Predicted flow rates were computed for most, but not all the icing conditions. Also, only conditions at angles of attack between 1 and 6 degrees were computed. Table B.1 presents the flow rates with the stainless steel panel on Wing Model A. Table B.2 presents the flow rates with the stainless steel panel on Wing Model B. Table B.3 presents the flow rates with the titanium panel on Wing Model A. Figure 5.2 presents the comparison between the experimental and ADS-4 predicted flow rates with (a) stainless steel panel on Wing Model A, (b) stainless steel panel on Wing Model B, and (c) titanium panel on Wing Model A. Figure 5.3 presents the same comparison between the experimental and analytical predicted flow rates.



(a) Wing Model A, Stainless Steel Mesh Panel

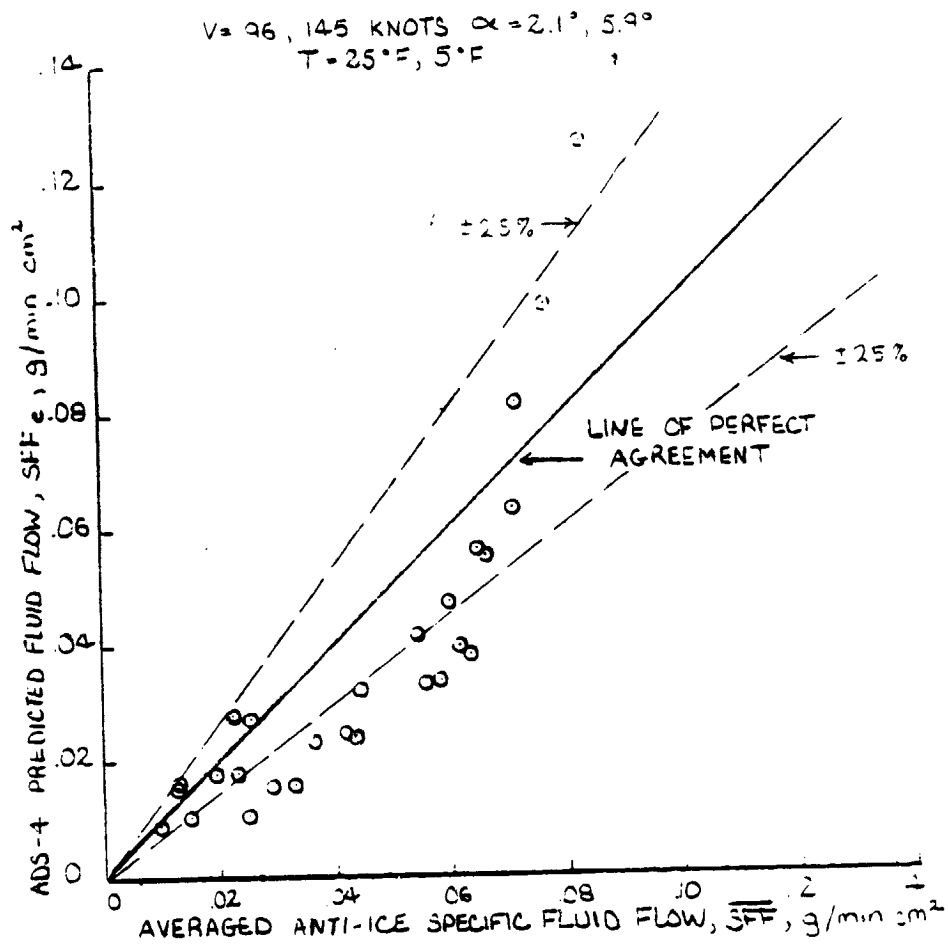
Figure 5.2. - Comparison of Averaged Experimental and ADS-4 Predicted Anti-Ice Fluid Flow Rates.



(b) Wing Model B, Stainless Steel Mesh Panel

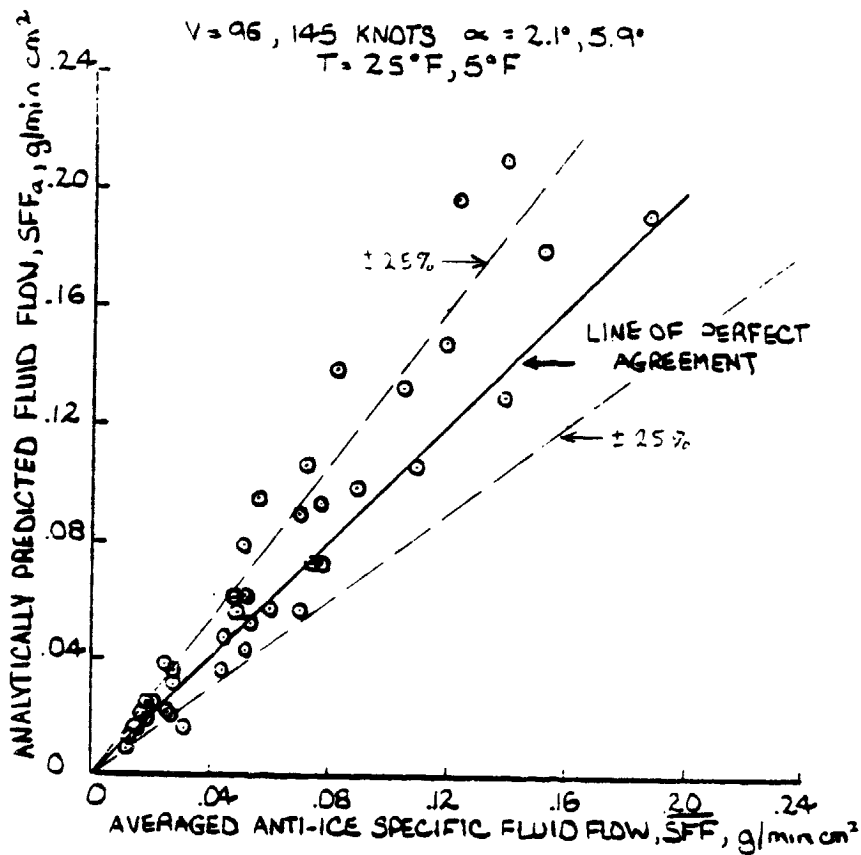
Figure 5.2. - (Continued.)

ORIGINAL PAGE IS  
OF POOR QUALITY



(c) Wing Model A, Titanium Panel

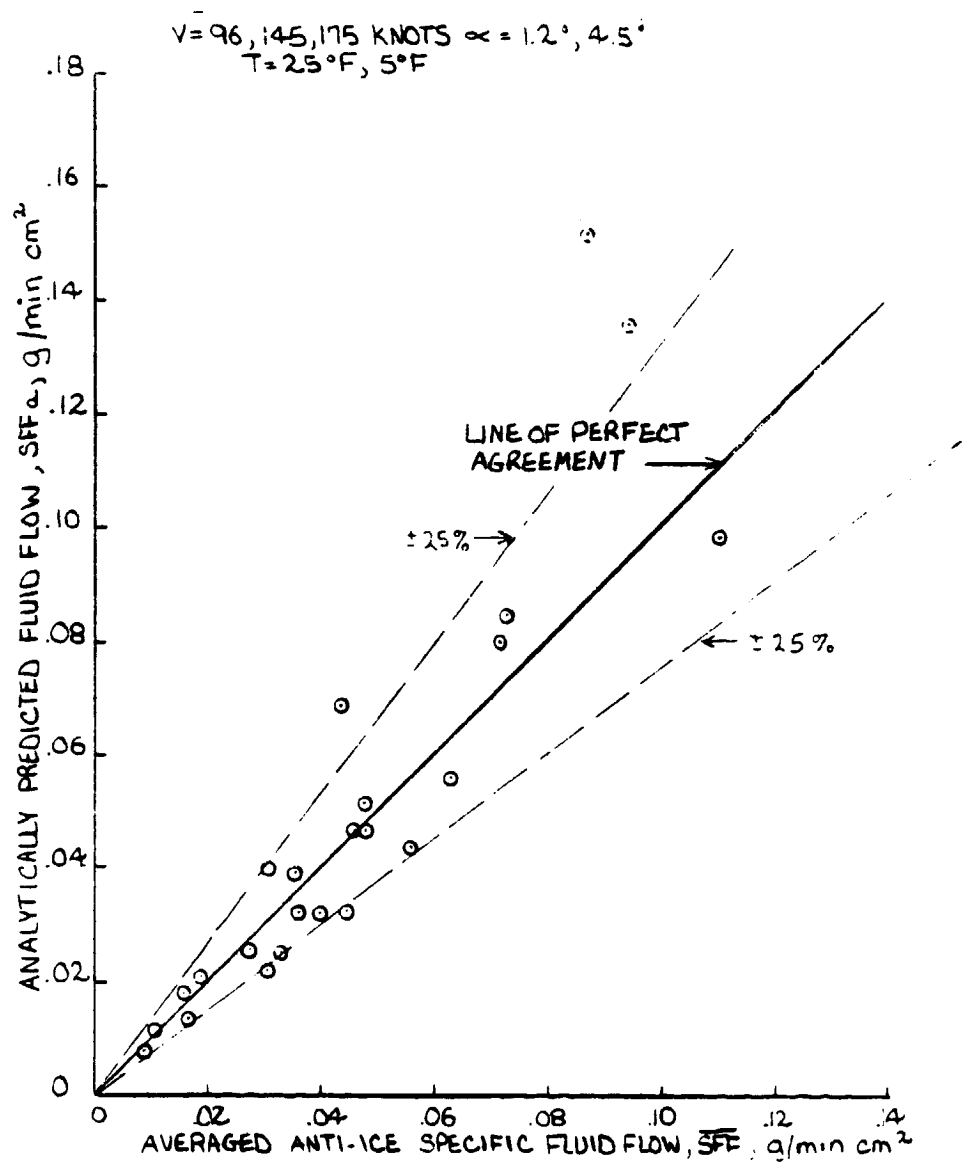
Figure 5.2. - (Continued.)



(a) Wing Model A, Stainless Steel Mesh Panel

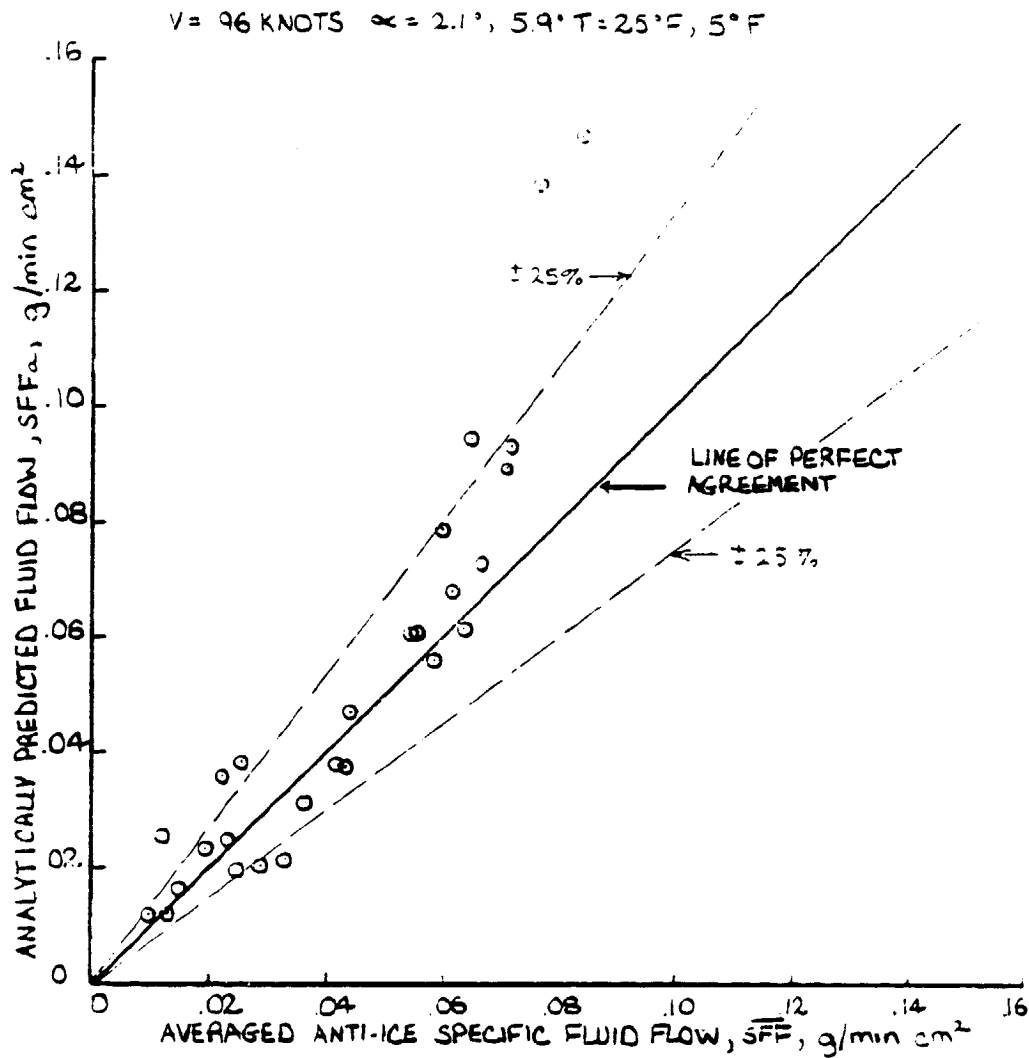
Figure 5.3. - Comparison of Averaged Experimental and Analytically Predicted Anti-Ice Fluid Flow Rates.

ORIGINAL PAGE IS  
OF POOR QUALITY



(b) Wing Model B, Stainless Steel Mesh Panel

Figure 5.3. - (Continued.)



(c) Wing Model A, Titanium Panel

Figure 5.3. - (Continued.)

To analyze the comparison statistically, a general purpose statistical computing program (Minitab) was used. Table IV presents the results of the analysis. This analysis was done using all the flow rates except the two high flow rate conditions shown on Figures 5.2 and 5.3 b and c, shown by the dashed symbols. These conditions, at  $V = 96$  knots,  $T = 5$  degrees F,  $LWC = 2.4 \text{ g/m}^3$ , and  $d = 20$  microns, were tested only one time, and are significantly higher than the Continuous Maximum envelope conditions. It is felt that the large influence these points could have on the statistical analysis is not warranted by the uncertainty associated with these points.

The correlation coefficient is an indication of the association between the experimental and predicted flow rates, with a value of 1.0 representing a perfect correlation. The correlation coefficients are quite high, with the lowest coefficient of .852. The highest correlation coefficient, .947, occurs with the stainless steel panel on the Wing Model A when comparing the analytical predicted to the experimental flow rates. Comparing the correlation coefficients for each wing-panel configuration, the analytical method is better correlated with the experimental results than the ADS-4 method.

Also included in Table IV are the linear term coefficients determined through a least squares regression, while forcing the regression line through the origin (0,0). The predicted flow rate

was treated as the independent variable, and the experimental flow rate as the dependent variable as shown in equation 5.

$$\text{Coefficient} * (\text{Predicted Flow}) = \text{Experimental Flow} \quad (5)$$

Thus, a coefficient of greater than 1.0 means the method predicts flow rates less than the actual flow rates. Opposing trends, as illustrated in Figures 5.2 and 5.3, are quickly noticed. The ADS-4 method consistently predicts values less than the experimental flow rates, with coefficients ranging from 1.22 to 1.77. The analytical method consistently predicts values more conservative (higher) than the experimental flow rate, with coefficients ranging from .78 to .98, a much narrower range. The fact that the analytical method appears to be more consistent from one configuration to the next is surprising since the calculation of  $\beta_{\max}$  is less certain than the calculation of  $E_m$ , used in the ADS-4 method. The fact that the analytical method tends to over predict the actual flow rates up to 25 percent could be advantageous from a design and safety standpoint. The analytical method also has the important advantage of being more consistent from one wing-panel configuration to the next. It is felt that the analytical method is superior to the ads-4 method for calculating anti-ice flow rates for a fluid ice protection system.

Table IV: Comparison of Experimental and Predicted Anti-Ice  
Fluid Flow Rates.

	<u>ADS-4 Method</u>	
	<u>Linear Term Coefficient</u>	<u>Correlation Coefficient</u>
Wing Model A, Stainless Steel Panel	1.16	.935
Wing Model B, Stainless Steel Panel	1.77	.867
Wing Model A, Titanium Panel	1.22	.880

	<u>Analytical Method</u>	
	<u>Linear Term Coefficient</u>	<u>Correlation Coefficient</u>
Wing Model A, Stainless Steel Panel	.78	.947
Wing Model B, Stainless Steel Panel	.98	.931
Wing Model A, Titanium Panel	.86	.934

#### 5.4 Sensitivity Analysis

The following examination of the possible areas of uncertainty in the data is necessary to appreciate the accuracy of the experimental and predicted flow rates.

- (1) Accuracy of setting and measuring the glycol fluid flow rate,  $\pm .001 \text{ g/min cm}^2$
- (2) Variability of liquid water content in tunnel icing cloud, approximately  $\pm 20\%$
- (3) Variation of air temperature in tunnel test section,  $\pm 1 \text{ degrees F}$
- (4) Variability in computing the overall collection efficiency  $E_m$ , approximately  $\pm 1\%$
- (5) Variability in computing the local maximum impingement efficiency  $\beta_{max}$ , approximately  $\pm 10\%$
- (6) Repeatability of judging anti-ice flow rates, as high as 100%, but generally less than  $\pm 25 \%$ .

#### 6.0 General Comments

Several comments can be made concerning the operation of the fluid ice protection system, and how the results can be applied to other situations.

1. Injecting a small amount of unfiltered glycol fluid through the titanium panel created a partial clogging of the porous region. This limited the amount of anti-ice data obtained at the end of the test plan, and did not allow reliable deice data to be acquired. A similar amount of unfiltered fluid did not affect the stainless steel panel.

2. Often a flow rate of 25% lower than the anti-ice flow rate will still provide adequate protection while not allowing a permanent accretion of ice on the leading edge.

3. Because of the subjectiveness in determining the actual anti-ice flow rates, the actual flow rate values should not be over emphasized. Even the calculated averaged flow rates should be used cautiously since not all icing conditions were repeated enough to obtain a flow rate with a high degree of repeatability.

4. A disadvantage of the icing conditions (LWC and d) available for testing in the IRT is that they do not directly correspond with the FAR Continuous Maximum and Intermittent Maximum Envelopes used for certification of ice protection systems. The glycol flow rates presented in this report, depending on the icing condition, may be several orders of magnitude higher than the flow rate for an icing condition within the FAR Part 25 Envelopes.

5. The flow rates presented in this report are typical of large leading edge radii general aviation airfoils only. The actual flow rates presented in this report cannot be generalized to other wing sections.

## 7.0 Conclusions

As a result of the tests presented in this report, the following conclusions have been made:

1. Anti-ice flow rates are unaffected by angle of attack as long as the stagnation location is within the center 50 to 75 percent of the active porous region of the leading edge panel.
2. As expected, the anti-ice flow rate increases with an increase in liquid water content and drop diameter.
3. A new laser drilled titanium panel tested for the first time in the NASA LeRC IRT proved successful. No significant difference in required anti-ice flow rates between it and the stainless steel panel were noticed.
4. The composite panel tested suffered from excessive porosity, causing the flow rates for anti-icing to be much higher than those required for the stainless steel panel.
5. Deice shed times of three minutes or less are possible using a glycol fluid flow rate equal to the anti-ice flow rate.
6. At 25 degrees F there is little difference between the TKS80 and AL5 glycol-water solutions. However, at 5 degrees F a higher flow

rate by approximately 20 percent is required when using the TKS80 fluid compared with that required when using the AL5 fluid.

7. An empirical method, ADS-4, predicts anti-ice flow rates less than the actual flow rates. This underprediction varied from one wing and panel configuration to the next.

8. An analytical method developed under a NASA grant predicts flow rates up to 25 percent above the actual flow rates. This method was more consistent in its prediction for three different wing and panel configurations.

#### 8.0 Recommendations

Additional icing wind tunnel tests are planned using a titanium and a composite panel, similar to those discussed in this report, on a new natural laminar flow airfoil. Several recommendations for further evaluation of the fluid ice protection system are as follows.

1. Determine anti-ice flow rates at lower liquid water contents. These icing conditions are now possible due to recent modifications to the IRT spray nozzle system, and will more closely match the FAR Part 25 Continuous Maximum conditions.

2. Determine the best leading edge temperature to be used in the analytical prediction technique, especially at velocities over 200 knots.
3. Test the fluid ice protection system on an aircraft in natural icing. This may be accomplished using the NASA LeRC Twin-Otter Icing Aircraft or with a Cessna 206. The anti-ice, deice, and pump characteristics should be compared to those obtained during the wind tunnel tests. The anti-icing flow rates should be used to verify the prediction techniques to natural icing conditions.
4. Further evaluate the deice characteristics through additional icing tunnel tests. Examine any differences in shed times depending if the system had been turned on temporarily prior to the ice accretion, with a minimal flow of glycol during the ice accretion, and with the system turned off prior to and during the ice accretion.
5. Conduct wind tunnel tests with airfoils and airspeeds typical of high performance aircraft.
6. Develop instrumentation to more objectively determine the minimum required anti-ice flow rates.

7. Examine the feasibility of a panel with chordwise varying porosity to direct a higher concentration of glycol to the stagnation region where the requirement for the glycol is the greatest.
8. Compare the stagnation point locations determined experimentally to those predicted analytically.

10. References

1. Kohlman, David L., Schweikhard, William G., Albright, Alan E., "Icing Tunnel Tests of a Glycol-Exuding Porous Leading Edge Ice Protection System on a General Aviation Airfoil," NASA CR 16544, September 1981.
2. Szelazek, C.A., and Hicks, R.M., "Upper-Surface Modifications for  $C_{1max}$  Improvement of Selected NACA 6-Series Airfoils," NASA TM 78603, August 1979.
3. Hicks, R.M., and Schairer, E.F., "Effects of Upper Surface Modification on the Aerodynamic Characteristics of the NACA 63<sub>2</sub>-215 Airfoil Section," NASA TM 78503, January 1979.
4. Kohlman, David L., "Icing Tunnel Tests of a Composite Porous Leading Edge for Use With a Liquid Anti-Ice System," KU-FRL-464-3, September 1981.

5. Federal Aviation Regulations, Part 25, Appendix C - Airworthiness Standards: Transport Category Airplanes, Department of Transportation, Federal Aviation Administration, Washington, D.C., June 1974.
6. Bowden, Gensemer, and Skeen, "Engineering Summary of Airframe Icing Technical Data," FAA Technical Report ADS-4, December 1963.
7. Lewis, James P., Blade, Robert J., "Experimental Investigation of Radome Icing and Icing Protection," NASA RM E52J31, January 1953.
8. Bragg, Michael B., "Rime Ice Accretion and Its Effect on Airfoil Performance," NASA CR 165599, March 1982.
9. Kohlman, David L., Albright, Alan E., "A Method of Predicting Flow Rates Required to Achieve Anti-Icing Performance with a Porous Leading Edge Ice Protection System," NASA CR 168213, August 1983.

Appendix A

Summary of Anti-Ice Wind Tunnel Results

Table A.1: Summary of Anti-Ice Flow Rates on Wing Model A, Stainless Steel Mesh Panel, ALS Fluid.

<u>V</u>	<u>T</u>	<u>Alpha</u>	<u>LWC</u>	<u>d</u>	<u>SFF<sub>x</sub></u>
Knots	°F	degrees	g/m <sup>3</sup>	microns	g/min cm <sup>2</sup>
96	25	-0.5	1.16	11	.0145
96	25	2.1	1.16	11	.0145
96	25	2.1	1.16	11	.0106
96	25	5.9	1.16	11	.0094
96	25	7.7	1.16	11	.0149
96	25	2.1	1.16	13	.0110
96	25	2.1	1.16	13	.0152
96	25	5.9	1.16	13	.0164
96	25	5.9	1.16	13	.0106
96	25	5.9	1.16	13	.0086
96	25	-2.0	1.16	15	.0489
96	25	-0.5	1.16	15	.0196
96	25	2.1	1.16	15	.0133
96	25	2.1	1.16	15	.0133
96	25	2.1	1.16	15	.0184
96	25	5.9	1.16	15	.0135
96	25	5.9	1.16	15	.0115
96	25	7.7	1.16	15	.0239
96	25	9.5	1.16	15	.0346
96	25	2.1	1.50	15	.0156
96	25	2.1	1.50	15	.0172
96	25	2.1	1.50	15	.0153
96	25	5.9	1.50	15	.0188
96	25	5.9	1.50	15	.0160
96	25	5.9	1.50	15	.0125
96	25	9.5	1.16	11	.0669
96	25	2.1	1.80	15	.0196
96	25	2.1	1.80	15	.0172
96	25	5.9	1.80	15	.0156
96	25	5.9	1.80	15	.0215
96	25	-0.5	1.55	20	.0297
96	25	-0.5	1.55	20	.0239
96	25	0.5	1.55	20	.0203
96	25	2.1	1.55	20	.0160
96	25	2.1	1.55	20	.0258
96	25	5.9	1.55	20	.0180
96	25	5.9	1.55	20	.0215
96	25	5.9	1.55	20	.0219
96	25	5.9	1.55	20	.0160
96	25	7.7	1.55	20	.0786
96	25	7.7	1.55	20	.0368
96	25	9.5	1.55	20	.0223
96	25	2.1	2.40	20	.0246
96	25	5.9	2.40	20	.0305

V	T	Alpha	LWC	d	SFF <sub>x</sub>
Knots	°F	degrees	g/m <sup>3</sup>	microns	g/min cm <sup>2</sup>
96	25	5.9	2.40	20	.0321
96	25	5.9	2.40	20	.0215
96	5	-0.5	1.16	11	.0332
96	5	-0.5	1.16	11	.0309
96	5	2.1	1.16	11	.0372
96	5	2.1	1.16	11	.0282
96	5	5.9	1.16	11	.0458
96	5	5.9	1.16	11	.0270
96	5	5.9	1.16	11	.0254
96	5	7.7	1.16	11	.0317
96	5	7.7	1.16	11	.0258
96	5	9.5	1.16	11	.0645
96	5	5.9	1.16	13	.0407
96	5	5.9	1.16	13	.0387
96	5	5.9	1.16	13	.0282
96	5	-0.5	1.16	15	.0571
96	5	-0.5	1.16	15	.0415
96	5	-0.5	1.16	15	.0630
96	5	-0.5	1.16	15	.0461
96	5	2.1	1.16	15	.0618
96	5	2.1	1.16	15	.0407
96	5	2.1	1.16	15	.0477
96	5	2.1	1.16	15	.0403
96	5	5.9	1.16	15	.0587
96	5	5.9	1.16	15	.0461
96	5	5.9	1.16	15	.0352
96	5	5.9	1.16	15	.0403
96	5	7.7	1.16	15	.0540
96	5	7.7	1.16	15	.0280
96	5	7.7	1.16	15	.0540
96	5	7.7	1.16	15	.0501
96	5	2.1	1.50	15	.0512
96	5	5.9	1.50	15	.0610
96	5	5.9	1.50	15	.0567
96	5	5.9	1.50	15	.0391
96	5	2.1	1.80	15	.0559
96	5	5.9	1.80	15	.0774
96	5	2.1	1.55	20	.0763
96	5	2.1	1.55	20	.0786
96	5	5.9	1.55	20	.0696
96	5	7.7	1.55	20	.0829
96	5	2.1	2.40	20	.1189
96	5	5.9	2.40	20	.0962
96	5	5.9	2.40	20	.0481
96	5	5.9	2.40	20	.0919
96	5	5.9	2.40	20	.0915
96	-10	5.9	1.16	11	.0598

V Knots	T °F	Alpha degrees	LWC g/m <sup>3</sup>	d microns	SFF <sub>x</sub> g/min cm <sup>2</sup>
96	-10	5.9	1.16	15	.0888
96	-10	5.9	1.50	15	.1146
145	25	-0.5	0.80	11	.0168
145	25	2.1	0.80	11	.0133
145	25	2.1	0.80	11	.0149
145	25	5.9	0.80	11	.0117
145	25	7.7	0.80	11	.0375
145	25	7.7	0.80	11	.0395
145	25	9.5	0.80	11	.0946
145	25	2.1	0.80	15	.0242
145	25	2.1	0.80	15	.0282
145	25	5.9	0.80	15	.0203
145	25	5.9	0.80	15	.0336
145	25	-0.5	1.16	15	.0774
145	25	-0.5	1.16	15	.0418
145	25	0.5	1.16	15	.0336
145	25	2.1	1.16	15	.0262
145	25	2.1	1.16	15	.0289
145	25	2.1	1.16	15	.0270
145	25	5.9	1.16	15	.0340
145	25	5.9	1.16	15	.0286
145	25	7.7	1.16	15	.0650
145	25	7.7	1.16	15	.0571
145	25	7.7	1.16	15	.0594
145	25	2.1	1.16	19	.0442
145	25	5.9	1.16	19	.0430
145	25	5.9	1.16	19	.0383
145	25	2.1	1.55	20	.0493
145	25	2.1	1.55	20	.0489
145	25	5.9	1.55	20	.0540
145	25	7.7	1.55	20	.0391
145	25	7.7	1.55	20	.0544
145	25	2.1	1.70	20	.0415
145	25	5.9	1.70	20	.0505
145	5	-0.5	0.80	11	.0798
145	5	2.1	0.80	11	.0704
145	5	5.9	0.80	11	.0508
145	5	5.9	0.80	11	.0469
145	5	5.9	0.80	11	.0579
145	5	2.1	0.80	15	.0743
145	5	5.9	0.80	15	.0681
145	5	5.9	0.80	15	.0763
145	5	-0.5	1.16	15	.1134
145	5	2.1	1.16	15	.1048
145	5	2.1	1.16	15	.1134
145	5	5.9	1.16	15	.0915
145	5	5.9	1.16	15	.0860

<u>V</u> Knots	<u>T</u> °F	<u>Alpha</u> degrees	<u>LWC</u> g/m <sup>3</sup>	<u>d</u> microns	<u>SFF<sub>x</sub></u> g/min cm <sup>2</sup>
145	5	7.7	1.16	15	.0892
145	5	7.7	1.16	15	.1033
145	5	2.1	1.16	19	.1044
145	5	5.9	1.16	19	.1384
145	5	2.1	1.55	20	.1867
145	5	2.1	1.55	20	.1862
145	5	5.9	1.55	20	.1560
145	5	5.9	1.55	20	.1474
145	5	7.7	1.55	20	.1760
145	5	2.1	1.70	20	.1392
145	5	5.9	1.70	20	.1224
145	-10	5.9	0.80	11	.0857
145	-10	5.9	0.80	15	.1115
145	-10	5.9	1.16	15	.1295

Table A.2: Summary of Anti-Ice Flow Rates on Wing Model A, Stainless Steel Mesh Panel, TKS80 Fluid.

V	T	Alpha	LWC	d	SFF <sub>y</sub>
Knots	°F	degrees	g/m <sup>3</sup>	microns	g/min cm <sup>2</sup>
96	25	2.1	1.16	11	.0117
96	25	5.9	1.16	11	.0090
96	25	2.1	1.16	15	.0176
96	25	5.9	1.16	15	.0145
96	25	2.1	1.50	15	.0211
96	25	5.9	1.50	15	.0368
96	25	5.9	1.50	15	.0297
96	25	5.9	1.50	15	.0196
96	25	2.1	1.80	15	.0227
96	25	5.9	1.80	15	.0278
96	25	5.9	1.80	15	.0168
96	25	5.9	1.80	15	.0336
96	25	2.1	1.55	20	.0258
96	25	2.1	1.55	20	.0278
96	25	5.9	1.55	20	.0203
96	25	5.9	1.55	20	.0254
96	5	2.1	1.16	11	.0375
96	5	5.9	1.16	11	.0372
96	5	2.1	1.16	15	.0583
96	5	5.9	1.16	15	.0438
96	5	2.1	1.50	15	.0489
96	5	5.9	1.50	15	.0559
96	5	5.9	1.50	15	.0415
96	5	2.1	1.80	15	.0626
96	5	5.9	1.80	15	.0532
96	5	5.9	1.80	15	.0579
96	-10	5.9	1.16	15	.1205
96	-10	5.9	1.16	15	.0845
96	-10	5.9	1.50	15	.1228
96	-10	5.9	1.50	15	.0849
145	25	2.1	0.80	11	.0211
145	25	2.1	0.80	11	.0203
145	25	5.9	0.80	11	.0203
145	25	5.9	0.80	11	.0235
145	25	5.9	0.80	11	.0235
145	25	2.1	0.80	15	.0254
145	25	5.9	0.80	15	.0223
145	25	5.9	0.80	15	.0282
145	25	5.9	0.80	15	.0282
145	25	2.1	1.16	15	.0344
145	25	2.1	1.16	15	.0360
145	25	5.9	1.16	15	.0375
145	25	5.9	1.16	15	.0293
145	25	2.1	1.55	20	.0508

<u>V</u>	<u>T</u>	<u>Alpha</u>	<u>LWC</u>	<u>d</u>	<u>SFF<sub>y</sub></u>
<u>Knots</u>	<u>°F</u>	<u>degrees</u>	<u>g/m<sup>3</sup></u>	<u>microns</u>	<u>g/min cm<sup>2</sup></u>
145	25	5.9	1.55	20	.0684
145	25	2.1	1.70	20	.0516
145	25	5.9	1.70	20	.0360
145	5	2.1	0.80	11	.0763
145	5	2.1	0.80	11	.0571
145	5	5.9	0.80	11	.0618
145	5	5.9	0.80	15	.0626
145	5	5.9	0.80	15	.0724
145	5	2.1	1.16	15	.1119
145	5	2.1	1.16	15	.1087
145	5	5.9	1.16	15	.0829
145	5	5.9	1.16	15	.1138
145	5	2.1	1.55	20	.1572
145	5	5.9	1.55	20	.1435
145	-10	2.1	0.80	11	.1095
145	-10	5.9	0.80	11	.0845
145	-10	5.9	0.80	11	.0927
145	-10	5.9	1.16	15	.1416

Table A.3: Summary of Anti-Ice Flow Rates on Wing Model B, Stainless Steel Mesh Panel, Observer 1.

V	T	Alpha	LWC	d	SFF <sub>1</sub>
Knots	°F	degrees	g/m <sup>3</sup>	microns	g/min cm <sup>2</sup>
96	25	7.8	1.16	11	.0068
96	25	4.5	1.16	11	.0055
96	25	1.2	1.16	11	.0086
96	25	12.0	1.16	15	.0126
96	25	7.8	1.16	15	.0102
96	25	4.5	1.16	15	.0138
96	25	1.2	1.16	15	.0108
96	25	4.5	1.55	15	.0138
96	25	4.5	1.80	15	.0194
96	25	4.5	1.55	20	.0200
96	25	7.8	2.40	20	.0305
96	25	4.5	2.40	20	.0272
96	25	1.2	2.40	20	.0317
96	9	4.5	2.17	17	.0690
96	9	4.5	2.40	20	.0805
96	5	12.0	1.16	11	.0487
96	5	7.8	1.16	11	.0253
96	5	4.5	1.16	11	.0349
96	5	1.2	1.16	11	.0302
96	5	4.5	2.40	20	.0869
96	5	1.2	2.40	20	.0940
145	25	1.2	1.16	15	.0388
175	25	7.8	0.80	11	.0346
175	25	4.5	0.80	11	.0355
175	25	1.2	0.80	11	.0376
175	25	7.8	1.16	15	.0635

Table A.4: Summary of Anti-Ice Flow Rates on Wing Model B, Stainless Steel Mesh Panel, Observer 2.

<u>V</u>	<u>T</u>	<u>Alpha</u>	<u>LWC</u>	<u>d</u>	<u>SFF<sub>2</sub></u>
<u>Knots</u>	<u>°F</u>	<u>degrees</u>	<u>g/m<sup>3</sup></u>	<u>microns</u>	<u>g/min cm<sup>2</sup></u>
96	25	7.8	1.16	11	.0120
96	25	4.5	1.16	11	.0117
96	25	12.0	1.16	15	.0346
96	25	7.8	1.16	15	.0269
96	25	4.5	1.16	15	.0219
96	25	4.5	1.16	15	.0135
96	25	4.5	1.55	15	.0182
96	25	4.5	1.80	15	.0185
96	25	4.5	1.55	20	.0426
96	25	4.5	1.55	20	.0200
96	25	1.2	1.55	20	.0416
96	25	1.2	1.55	20	.0247
96	25	7.8	2.40	20	.0292
96	25	4.5	2.40	20	.0336
96	25	1.2	2.40	20	.0394
96	5	7.8	1.16	11	.0200
96	5	7.8	1.16	11	.0450
96	5	4.5	1.16	11	.0370
96	5	1.2	1.16	11	.0379
96	5	7.8	1.16	15	.0484
96	5	7.8	1.16	15	.0475
96	5	4.5	1.16	15	.0379
96	5	4.5	1.16	15	.0577
96	5	4.5	1.16	15	.0465
96	5	1.2	1.16	15	.0426
96	5	1.2	1.16	15	.0699
96	5	4.5	1.55	15	.0435
96	5	4.5	1.80	15	.0715
96	5	4.5	1.55	20	.1097
145	25	1.2	1.16	15	.0542
145	25	1.2	1.16	15	.0265
145	25	1.2	1.55	20	.0629
175	25	7.8	0.80	11	.0209
175	25	4.5	0.80	11	.0256
175	25	1.2	0.80	11	.0327
175	25	4.5	0.80	15	.0443
175	25	7.8	1.16	15	.0404
175	25	4.5	1.16	15	.0349
175	25	4.5	1.16	15	.0567
175	25	1.2	1.16	15	.0479
175	25	4.5	1.16	19	.0675
175	25	4.5	1.16	19	.0706
175	25	1.2	1.55	20	.0641
175	25	1.2	1.55	20	.0817

Table A.5: Summary of Anti-Ice Flow Rates on Wing Model A, Titanium Panel, Observer 1.

<u>V</u> Knots	<u>T</u> °F	<u>Alpha</u> degrees	<u>LWC</u> g/m <sup>3</sup>	<u>d</u> microns	<u>SFF<sub>1</sub></u> g/min cm <sup>2</sup>
96	25	-2.0	1.16	15	.0204
96	25	-.5	1.16	15	.0194
96	25	2.1	1.16	15	.0146
96	25	5.9	1.16	15	.0094
96	25	7.7	1.16	15	.0090
96	25	2.1	1.50	15	.0166
96	25	5.9	1.50	15	.0152
96	25	-.5	1.55	20	.0329
96	25	2.1	1.55	20	.0281
96	25	5.9	1.55	20	.0211
96	25	7.7	1.55	20	.0211
96	5	-2.0	1.16	15	.0745
96	5	-.5	1.16	15	.0759
96	5	2.1	1.16	15	.0648
96	5	5.9	1.16	15	.0551
96	5	7.7	1.16	15	.0492
96	5	2.1	1.50	15	.0672
96	5	5.9	1.50	15	.0575
96	5	-.5	1.55	20	.0735
96	5	2.1	1.55	20	.0710
96	5	2.1	1.80	15	.0679
145	25	2.1	0.80	15	.0281
145	25	5.9	0.80	15	.0225
145	25	2.1	1.16	15	.0388
145	25	2.1	1.16	15	.0340
145	25	5.9	1.16	15	.0291
145	25	2.1	1.16	19	.0440
145	25	2.1	1.16	19	.0402
145	25	5.9	1.16	19	.0423
145	25	2.1	1.55	20	.0627
145	25	2.1	1.55	20	.0541
145	25	2.1	1.70	20	.0683
145	25	2.1	1.70	20	.0582
145	5	2.1	0.80	15	.0665
145	5	5.9	0.80	15	.0617

Table A.6: Summary of Anti-Ice Flow Rates on Wing Model A, Titanium Panel, Observer 2.

<u>V</u> Knots	<u>T</u> °F	<u>Alpha</u> degrees	<u>LWC</u> g/m <sup>3</sup>	<u>d</u> microns	<u>SFF<sub>2</sub></u> g/min cm <sup>2</sup>
96	25	-2.0	1.16	15	.0374
96	25	-2.0	1.16	15	.0166
96	25	-.5	1.16	15	.0159
96	25	2.1	1.16	15	.0152
96	25	5.9	1.16	15	.0101
96	25	7.7	1.16	15	.0076
96	25	2.1	1.50	15	.0159
96	25	5.9	1.50	15	.0104
96	25	-.5	1.55	20	.0280
96	25	2.1	1.55	20	.0198
96	25	2.1	1.55	20	.0218
96	25	5.9	1.55	20	.0184
96	25	7.7	1.55	20	.0180
96	25	2.1	1.80	15	.0121
96	25	2.1	2.40	20	.0256
96	25	5.9	2.40	20	.0222
96	5	-.5	1.16	15	.0520
96	5	2.1	1.16	15	.0490
96	5	2.1	1.16	15	.0534
96	5	5.9	1.16	15	.0336
96	5	5.9	1.16	15	.0460
96	5	7.7	1.16	15	.0492
96	5	7.7	1.16	15	.0500
96	5	2.1	1.50	15	.0530
96	5	5.9	1.50	15	.0515
96	5	2.1	1.55	20	.0730
96	5	5.9	1.55	20	.0710
96	5	2.1	1.80	15	.0621
96	5	2.1	2.40	20	.0841
96	5	5.9	2.40	20	.0770
145	25	2.1	0.80	15	.0381
145	25	5.9	0.80	15	.0277
145	25	5.9	1.16	19	.0444

Appendix B

Averaged Experimental and Predicted  
Anti-Ice Fluid Flow Rates

Table B:1: Averaged Experimental and Predicted Flow Rates on Wing Model A with Stainless Steel Mesh Panel.

V knots	T of	Alpha degrees	LMC g/m <sup>3</sup>	d microns	SFE <sub>A</sub>	Anti-Ice Flow Rates g/min cm <sup>2</sup>			h/c	S <sub>u-Sl</sub>	E <sub>m</sub>	β <sub>max</sub>
						SFE <sub>E</sub>	SFE <sub>A</sub>	SFE <sub>Y</sub>				
9b	25	-1.5	1.16	11	.0145							
9c	25	2.1	1.16	11	.0126							
9d	25	5.9	1.16	11	.0094		.0117					
9e	25	7.7	1.16	11	.0149							
9f	25	9.5	1.16	11	.0069							
9g	25	2.1	1.16	13	.0131							
9h	25	5.9	1.16	13	.0119	.0072	.0092	.1472	.01762	.01540		.171
9i	25	-2.0	1.16	13	.0489							
9j	25	-1.5	1.16	13	.0196							
9k	25	2.1	1.16	15	.0150	.0107	.0163	.1209	.02981	.04690		.303
9l	25	5.9	1.16	15	.0125	.0094	.0120	.1472	.02353	.02660		.224
9m	25	7.7	1.16	15	.0239							
9n	25	9.5	1.16	15	.0146							
9o	25	2.1	1.50	15	.0160	.0138	.0210	.1209	.02981	.04690		.303
9p	25	5.9	1.50	15	.0158	.0122	.0156	.1472	.02353	.02660		.224
9q	25	2.1	1.80	15	.0184	.0168	.0252	.1209	.02981	.04690		.303
9r	25	5.9	1.80	15	.0186	.0147	.0187	.1472	.02353	.02660		.224
9s	25	-0.5	1.55	20	.0168							
9t	25	0.5	1.55	20	.0203	.0181	.0248	.1209	.04554	.0895		.397
9u	25	2.1	1.55	20	.0209	.0181	.0232	.1472	.04441	.07210		.323
9v	25	5.9	1.55	20	.0194							
9w	25	7.7	1.55	20	.0577							
9x	25	9.5	1.55	20	.0223							
9y	25	2.1	2.40	20	.0246	.0278	.0384	.1209	.04554	.0895		.397
9z	25	5.9	2.40	20	.0280	.0280	.0359	.1472	.04441	.07210		.323
9aa	5	-1.5	1.16	11	.0321							
9ab	5	2.1	1.16	11	.0327			.0375				
9ac	5	5.9	1.16	11	.0327			.0372				
9ad	5	7.7	1.16	11	.0288							
9ae	5	9.5	1.16	11	.0645							
9af	5	5.9	1.16	13	.0359							
9ag	5	-1.5	1.16	15	.0519							
9ah	5	2.1	1.16	15	.0476	.0366	.0610	.1209	.03093	.04830		.297
9ai	5	5.9	1.16	15	.0451	.0326	.0471	.1472	.02410	.02750		.225
9aj	5	7.7	1.16	15	.0465							
9ak	5	2.1	1.50	15	.0512	.0473	.0789	.1209	.03093	.04830		.297
9al	5	5.9	1.50	15	.0523	.0421	.0608	.1472	.02410	.02750		.229
9am	5	2.1	1.80	15	.0559	.0583	.0947	.1209	.03093	.04830		.297
9an	5	5.9	1.80	15	.0774	.0514	.0730	.1472	.02410	.02750		.229
9ao	5	2.1	1.55	20	.0775	.0819	.0935	.1209	.03372	.09267		.348

ORIGINAL PAGE IS  
OF POOR QUALITY

Table B.1: (Continued.)

V knots	T of	Alpha degrees	LWC g/m <sup>3</sup>	d microns	Anti-Ice Flow Rates g/min cm <sup>2</sup>				h/c	Su-Sl	E <sub>m</sub>	F <sub>max</sub>
					SFF <sub>e</sub>	SFF <sub>g</sub>	SFF <sub>y</sub>	SFF <sub>x</sub>				
96	5	5.9	1.55	20	.0633	.0897			.1472	.04467	.327	
96	5	7.7	1.55	20	.0829							
96	5	2.1	2.40	20	.1189	.1479			.1209	.03572	.348	
96	5	5.9	2.40	20	.0819	.1390			.1472	.04467	.327	
96	-10	5.9	1.16	11	.0598							
96	-10	5.9	1.16	15	.0888		.1025					
96	-10	5.9	1.50	15	.1146		.1039					
145	25	-5	0.80	11	.0168							
145	25	2.1	0.80	11	.0141		.0207		.1209			
145	25	5.9	0.80	11	.0117		.0224					
145	25	7.7	0.80	11	.0185							
145	25	9.5	0.80	11	.0946							
145	25	2.1	0.80	15	.0262	.0216	.0254		.1209	.30014	.321	
145	25	5.9	0.80	15	.0270	.0197	.0270		.1472	.04162	.291	
145	25	-5	1.16	15	.0596							
145	25	-5	1.16	15	.0336							
145	25	2.1	1.16	15	.0274							
145	25	5.9	1.16	15	.0311	.0313	.0152		.1209	.30014	.321	
145	25	7.7	1.16	15	.0605	.0158	.0334		.1472	.04162	.291	
145	25	2.1	1.16	19	.0442	.0251	.0380		.1209	.05197	.418	
145	25	5.9	1.16	19	.0407	.0242	.0378		.1472	.05324	.388	
145	25	2.1	1.55	20	.0691	.0338	.0561	.0508	.1209	.05531	.431	
145	25	5.9	1.55	20	.0540	.0353	.0525	.0684	.1472	.05403	.403	
145	25	7.7	1.55	20	.0468							
145	25	2.1	1.70	20	.0415	.0382	.0616	.0516	.1209	.05531	.431	
145	25	5.9	1.70	20	.0505	.0386	.0376	.0360	.1472	.05403	.403	
145	5	-5	0.80	11	.0798							
145	5	2.1	0.80	11	.0704	.0340	.0565	.0667	.1209	.02677	.245	
145	5	5.9	0.80	11	.0519	.0290	.0424	.0618	.1472	.01864	.184	
145	5	2.1	0.80	15	.0743	.0552	.0730		.1209	.03295	.317	
145	5	5.9	0.80	15	.0722	.0397	.1060	.0625	.1472	.04037	.295	
145	5	-5	1.16	15	.1134							
145	5	2.1	1.16	15	.1091	.0798	.1060	.1103	.1209	.03295	.317	
145	5	5.9	1.16	15	.0888	.0575	.0986	.0984	.1472	.04037	.295	
145	5	7.7	1.16	15	.0963							
145	5	2.1	1.16	19	.1044	.0883	.1324		.1209	.05035	.396	
145	5	5.9	1.16	19	.1384	.0817	.1297		.1472	.05389	.388	
145	5	2.1	1.55	20	.1865	.1219	.1920	.1572	.1209	.05374	.430	
145	5	5.9	1.55	20	.1517	.1179	.1800	.1435	.1472	.05464	.407	
145	5	7.7	1.55	20	.1760							
145	5	2.1	1.70	20	.1392	.1130	.2106		.1209	.05374	.418	
145	5	5.9	1.70	20	.1224	.1290	.1974		.1472	.05464	.403	
145	-10	2.1	0.80	11	----			.1095				
145	-10	5.9	0.80	11	.0857			.0886				
145	10	5.9	0.80	15	.1115							

Table B.2: Averaged Experimental and Predicted Flow Rates on Wing Model B with Stainless Steel Mesh Panel.

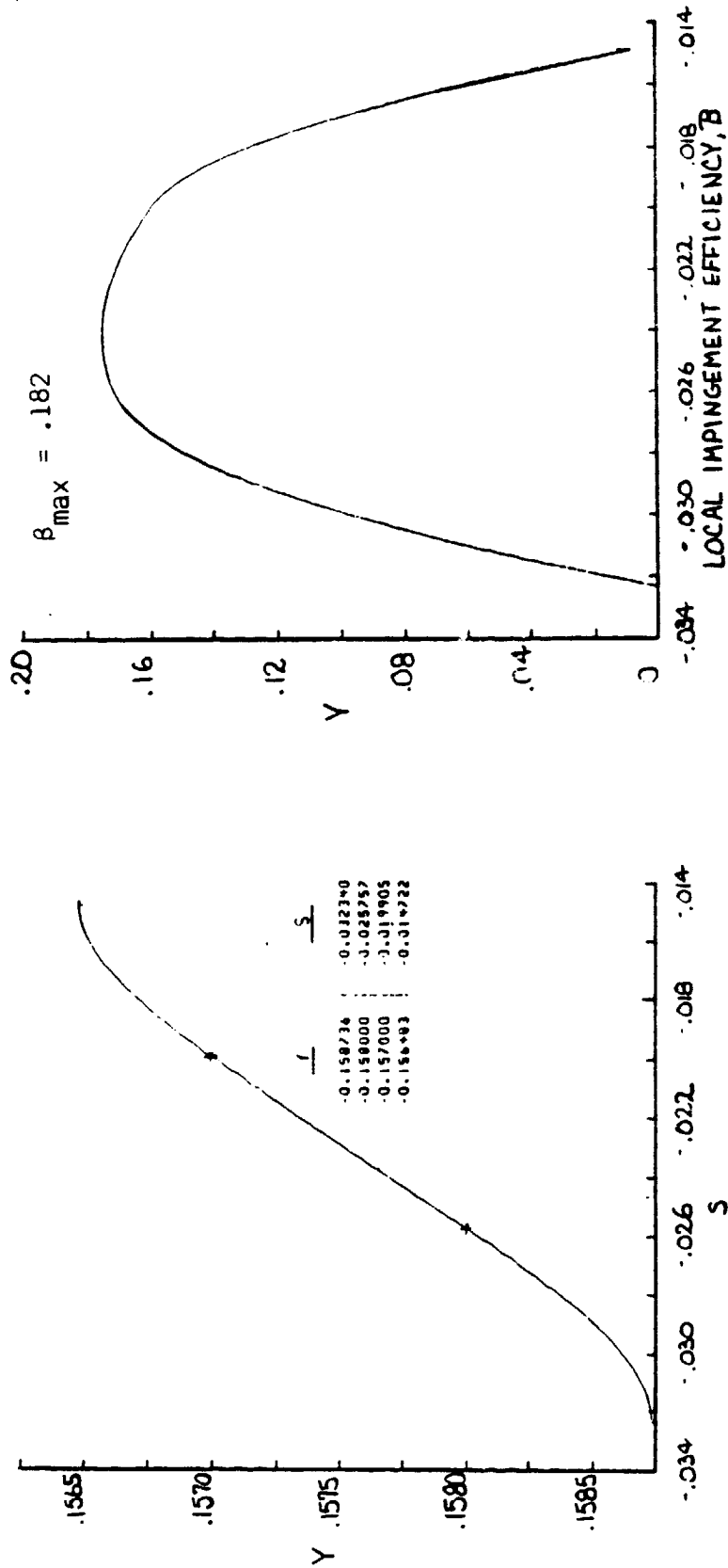
V Knots	T of	Alpha degrees	LWC g/m <sup>3</sup>	d microns	Anti-Ice Flow Rates g/min cm <sup>2</sup>		h/c	Su-Sl	Em	F <sub>max</sub>
					SFF	SFF <sub>e</sub>				
96	25	7.8	1.16	11	.0494					
96	25	4.5	1.16	11	.0497	.0056	.1709	.01365	.00803	.147
96	25	1.2	1.16	11	.0486					
96	25	12.0	1.16	15	.0236					
96	25	7.8	1.16	15	.0186					
96	25	4.5	1.16	15	.0165	.0188	.1709	.02405	.02200	.251
96	25	1.2	1.16	15	.0108	.0492	.1525	.02396	.02465	.215
96	25	4.5	1.55	15	.0160	.0118	.1709	.02405	.02200	.251
96	25	4.5	1.80	15	.0190	.0137	.1709	.02405	.02200	.251
96	25	4.5	1.55	20	.0275	.0144	.1709	.03986	.17087	.360
96	25	1.2	1.55	20	.0731	.0752	.1525	.04718	.06220	.351
96	25	7.8	2.40	20	.0299					
96	25	4.5	2.40	20	.0304	.0223	.1709	.03986	.04449	.360
96	25	1.2	2.40	20	.0156	.0235	.1525	.04718	.06220	.351
96	9	4.5	2.17	17	.0690					
96	9	4.5	2.40	20	.0805					
96	5	7.8	1.16	11	.0301					
96	5	4.5	1.16	11	.0360					
96	5	1.2	1.16	11	.0741	.0196	.1709	.01454	.00855	.156
96	5	7.8	1.16	15	.0679					
96	5	4.5	1.16	15	.0473					
96	5	1.2	1.16	15	.0562	.0311	.1709	.02448	.02290	.251
96	5	4.5	1.55	15	.0435	.0324	.1525	.02346	.02558	.213
96	5	4.5	1.80	15	.0715	.0416	.1709	.02448	.02290	.251
96	5	4.5	1.55	20	.1097	.0483	.1709	.02448	.02290	.251
96	5	4.5	2.40	20	.0869	.0474	.1709	.04308	.04590	.358
96	5	1.2	2.40	20	.0940	.0737	.1709	.04308	.04590	.358
145	25	1.2	1.16	15	.0399	.0815	.1525	.04719	.06382	.320
145	25	1.2	1.55	20	.0629	.0156	.1525	.03755	.06142	.324
175	25	7.8	0.80	11	.0278	.0252	.1525	.05871	.08892	.422
175	25	4.5	0.80	11	.0305	.0122	.1709	.02251	.10927	.232
175	25	1.2	0.80	11	.0352					
175	25	4.5	0.80	15	.0443	.0156	.1709	.03685	.04040	.337
175	25	7.8	1.16	15	.0520					
175	25	4.5	1.16	15	.0458	.0226	.1709	.03685	.04040	.337
175	25	1.2	1.16	15	.0479	.0234	.1525	.04303	.05460	.336
175	25	4.5	1.16	19	.0690					
175	25	1.2	1.55	20	.0729	.0403	.1525	.06379	.10446	.458

Table B.3: Averaged Experimental and Predicted Flow Rates on Wing Model A with Titanium Panel.

V Knots	I of	Alpha degrees	LWC g/m <sup>3</sup>	d microns	Anti-ice Flow Rates g/min cm <sup>2</sup>			h/c	S <sub>U-5</sub>	ε <sub>m</sub>	ε <sub>max</sub>
					SFF	SFF <sub>e</sub>	SFF <sub>a</sub>				
96	25	-2.0	1.16	15	.0248						
96	25	-5	1.16	15	.0177						
96	25	2.1	1.16	15	.0149	.0107	.0163	.1209	.02981	.04690	.303
96	25	5.9	1.16	15	.0098	.0094	.0120	.1472	.02333	.02660	.224
96	25	7.7	1.16	15	.0083						
96	25	2.1	1.50	15	.0103						
96	25	5.9	1.50	15	.0128	.0156	.0122	.1472	.02353	.02660	.224
96	25	-5	1.55	20	.0305						
96	25	2.1	1.55	20	.0232	.0181	.0248	.1209	.04554	.0895	.397
96	25	5.9	1.55	20	.0198	.0181	.0232	.1472	.04441	.0721	.323
96	25	7.7	1.55	20	.0196						
96	25	2.1	1.80	15	.0121	.0168	.0252	.1209	.02981	.04690	.303
96	25	2.1	2.40	20	.0256	.0278	.0364	.1209	.04554	.0895	.397
96	25	5.9	2.40	20	.0222	.0280	.0359	.1472	.04441	.07210	.323
96	5	-2.0	1.16	15	.0745						
96	5	-5	1.16	15	.0640						
96	5	2.1	1.16	15	.0557	.0366	.0610	.1209	.03093	.04830	.297
96	5	5.9	1.16	15	.0464	.0326	.0471	.1472	.02410	.02750	.229
96	5	7.7	1.16	15	.0495						
96	5	2.1	1.50	15	.0601	.0473	.0789	.1209	.03043	.04830	.297
96	5	-5	1.55	20	.0735	.0421	.0608	.1472	.02410	.02750	.229
96	5	2.1	1.55	20	.0720	.0819	.0935	.1209	.03572	.09267	.348
96	5	5.9	1.55	20	.0710	.0633	.0897	.1472	.04467	.07413	.327
96	5	2.1	1.80	15	.0650	.0563	.0947	.1209	.03093	.04830	.297
96	5	2.1	2.40	20	.0841	.1268	.1471	.1209	.03572	.09267	.348
96	5	5.9	2.40	20	.0770	.0989	.1390	.1472	.04467	.07413	.327
145	25	2.1	0.80	15	.0331	.0161	.0216	.1209	.00104	.06792	.321
145	25	5.9	0.80	15	.0251	.0108	.0197	.1472	.04162	.04770	.293
145	25	2.1	1.16	15	.0364	.0233	.0313	.1209	.00104	.06792	.321
145	25	5.9	1.16	15	.0291	.0206	.0266	.1472	.04162	.04770	.293
145	25	2.1	1.16	19	.0421	.0251	.0380	.1209	.05197	.11506	.418
145	25	5.9	1.16	19	.0434	.0242	.0378	.1472	.05324	.09423	.388
145	25	2.1	1.55	20	.0584	.0338	.0561	.1209	.05531	.12750	.431
145	25	2.1	1.70	20	.0633	.0382	.0616	.1209	.05531	.12750	.431
145	5	2.1	0.80	15	.0665	.0552	.0730	.1209	.03295	.06918	.317
145	5	5.9	0.80	15	.0617	.0397	.0480	.1472	.04037	.05052	.295

Appendix C

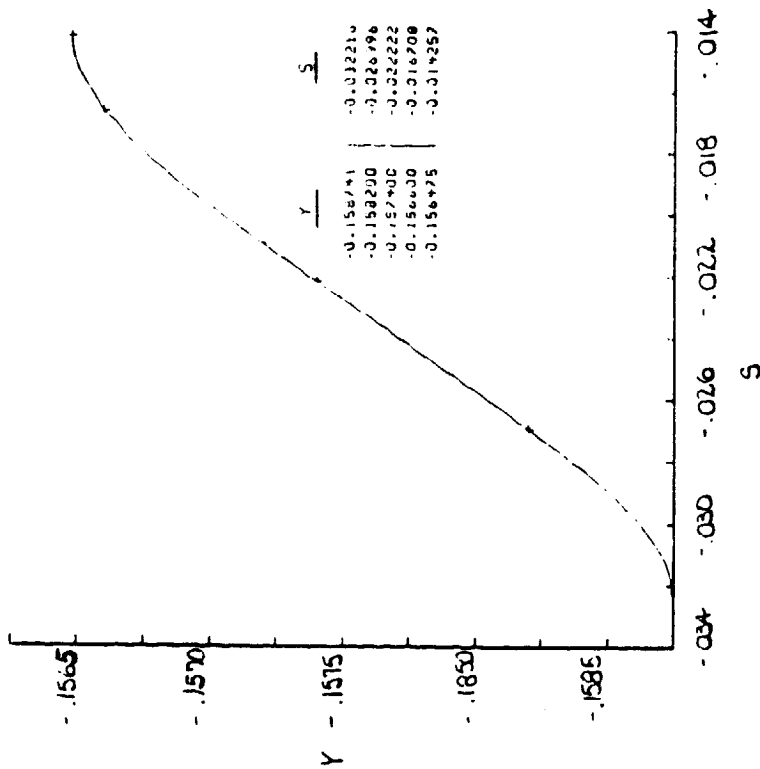
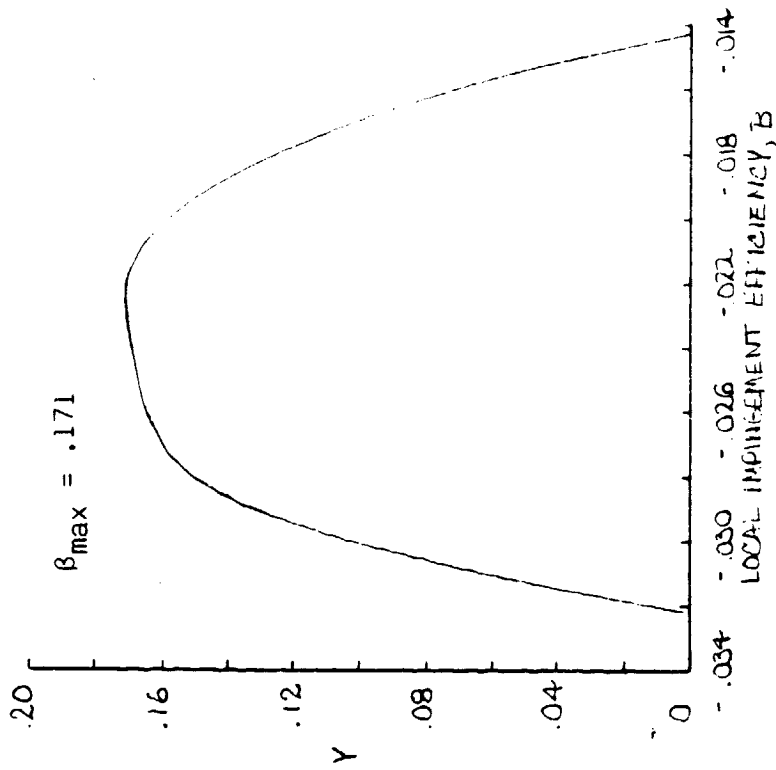
Water Droplet Impingement Efficiency Distributions



(a) With 4 Trajectories Impacting Airfoil

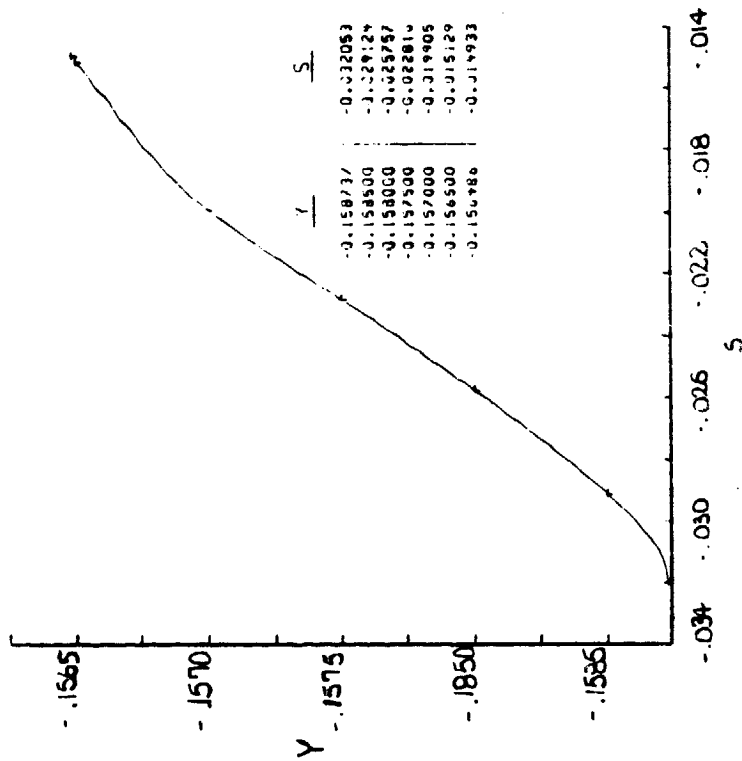
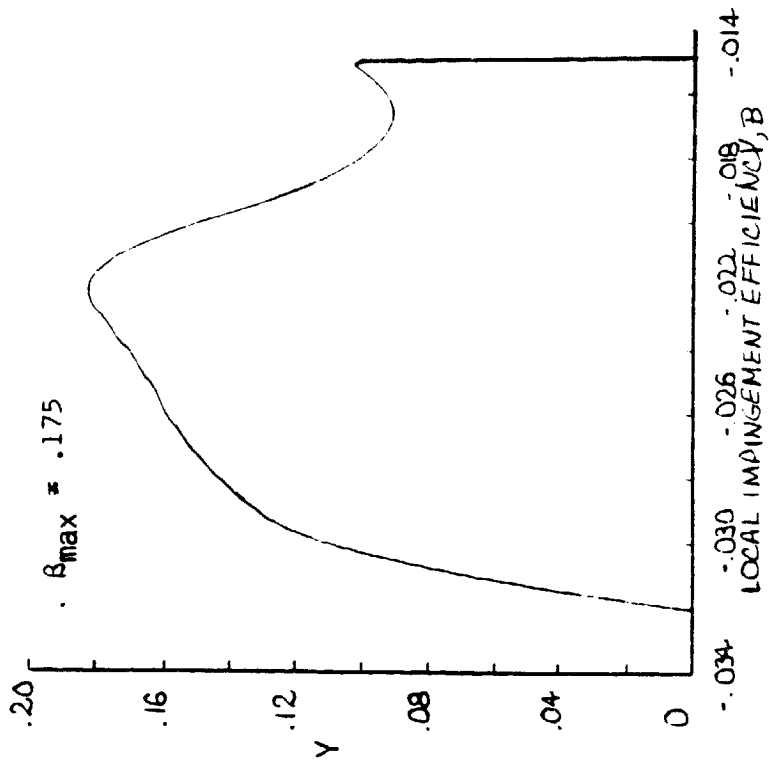
Figure C.1. - Local Impingement Efficiency Distributions at  $V = 96$  Knots,  $T = 25^\circ F$ , Angle of Attack =  $5.9^\circ$ , and  $d = 13$  microns.

ORIGINAL PAGE IS  
OF POOR QUALITY



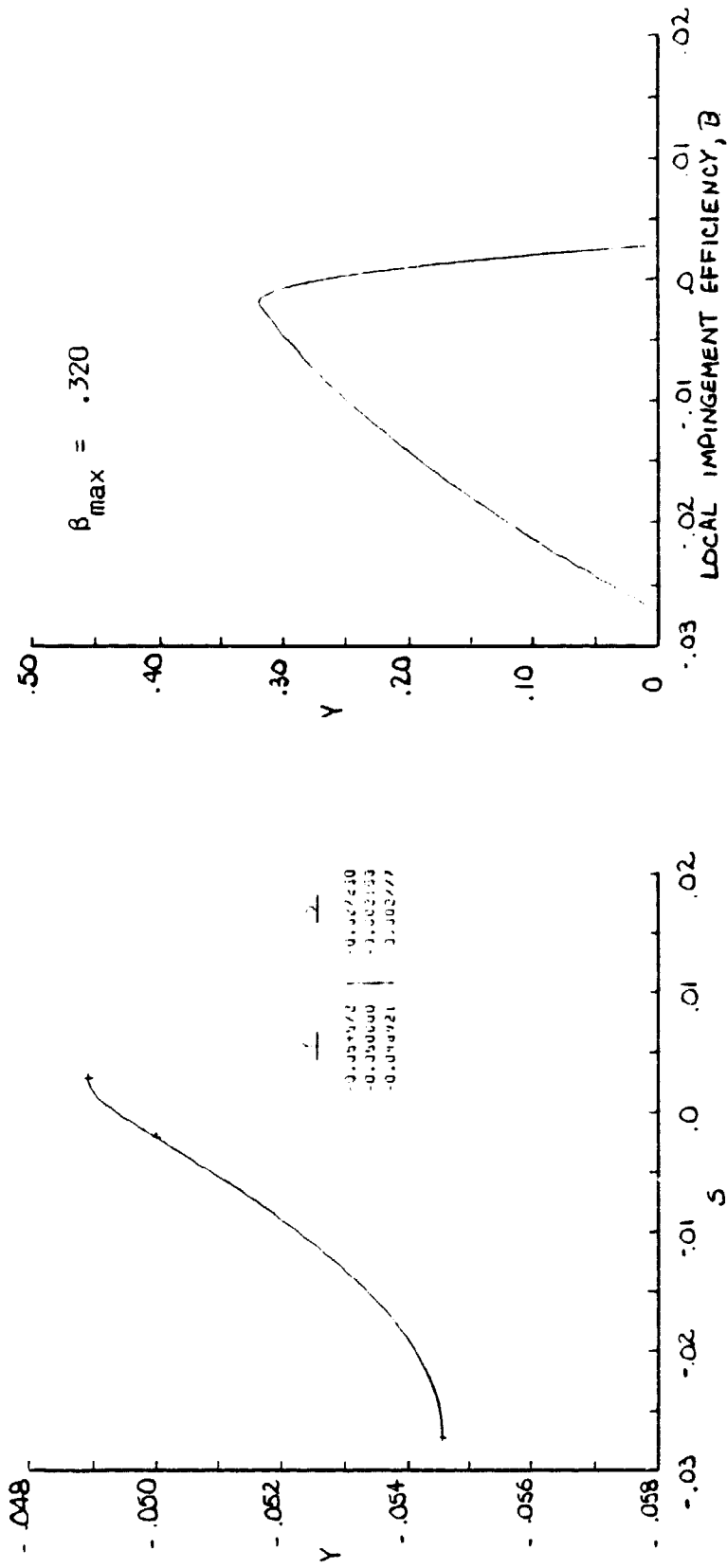
(b) with 5 Trajectories Impacting Airfoil

Figure C.1. - (Continued.)



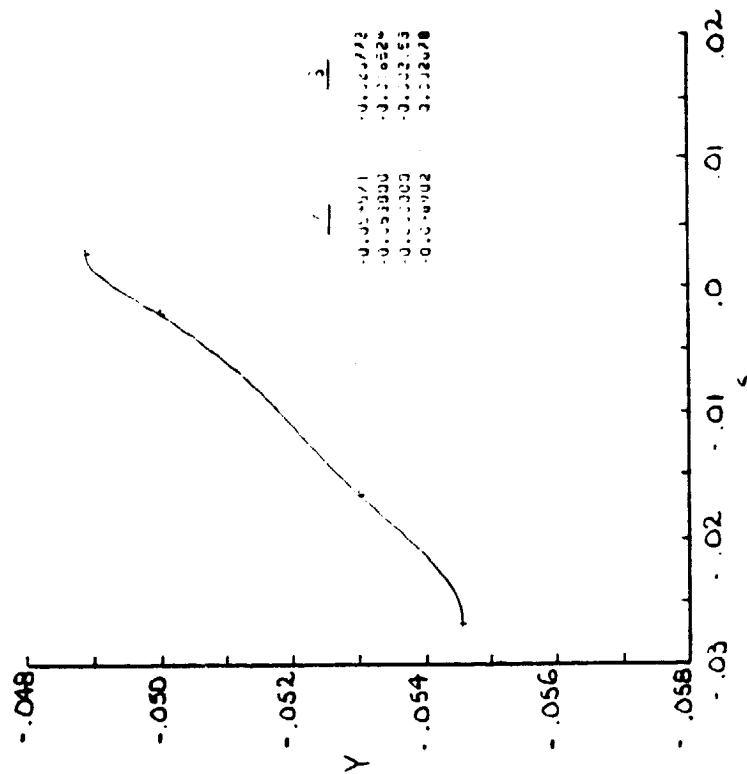
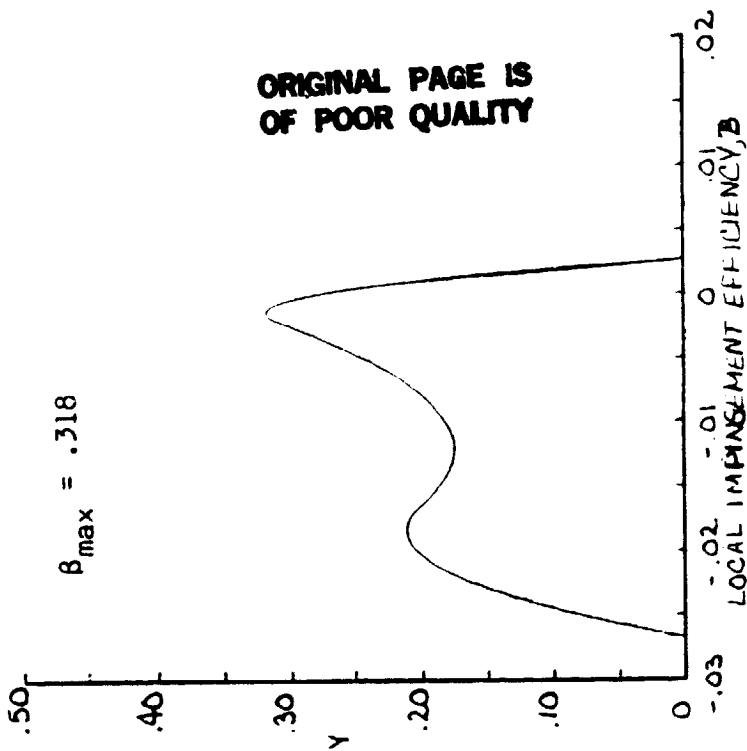
(c) With 7 Trajectories Impacting Airfoil

Figure C.1. - (Continued.)



(a) With 3 Trajectories Impacting Airfoil

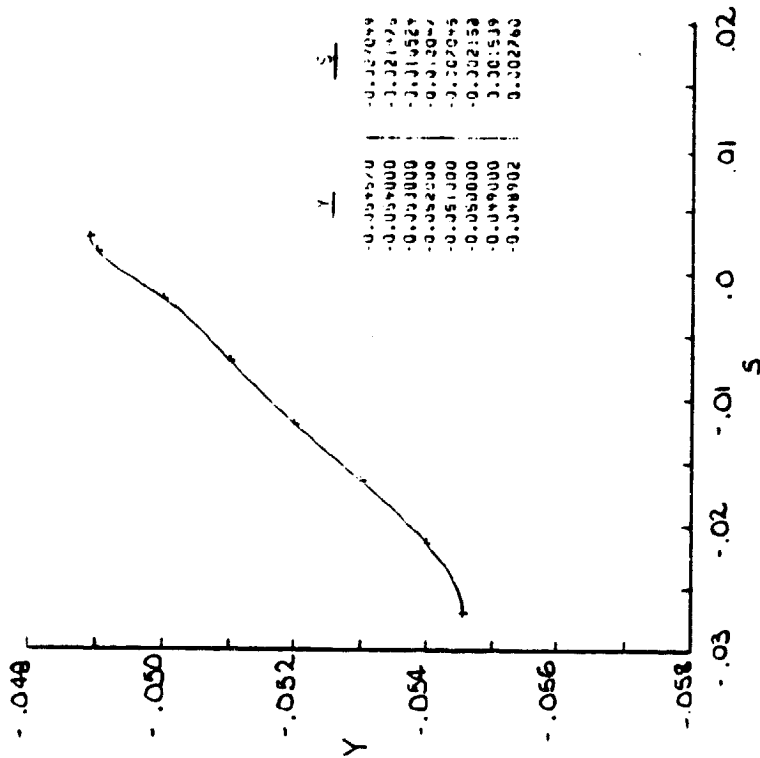
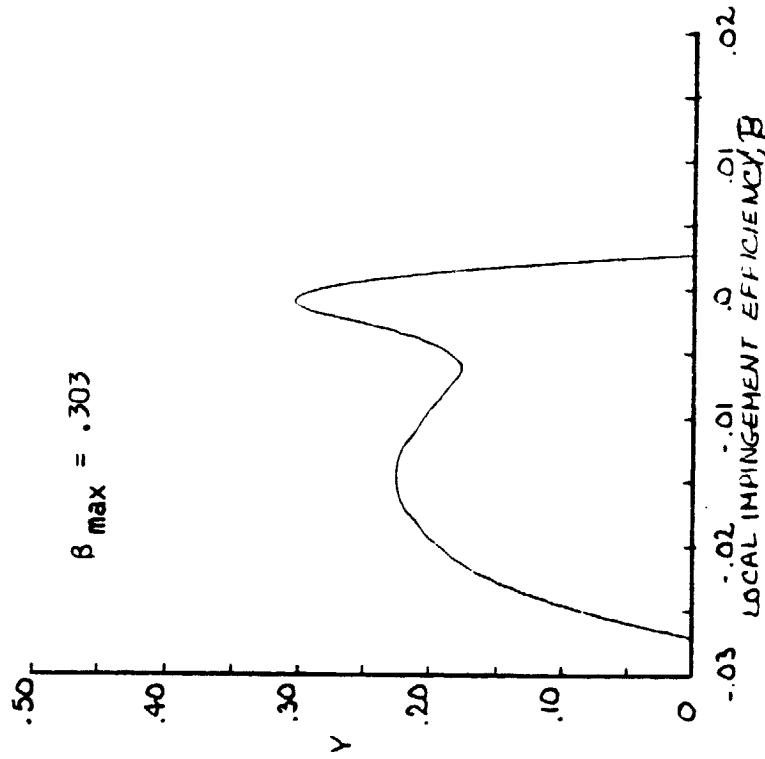
Figure C.2. - Local Impingement Efficiency Distributions at  $V = 96$  Knots  
 $T = 25^\circ F$ , Angle of Attack =  $2.1^\circ$ , and  $d = 15$  microns.



(b) With 4 Trajectories Impacting Airfoil

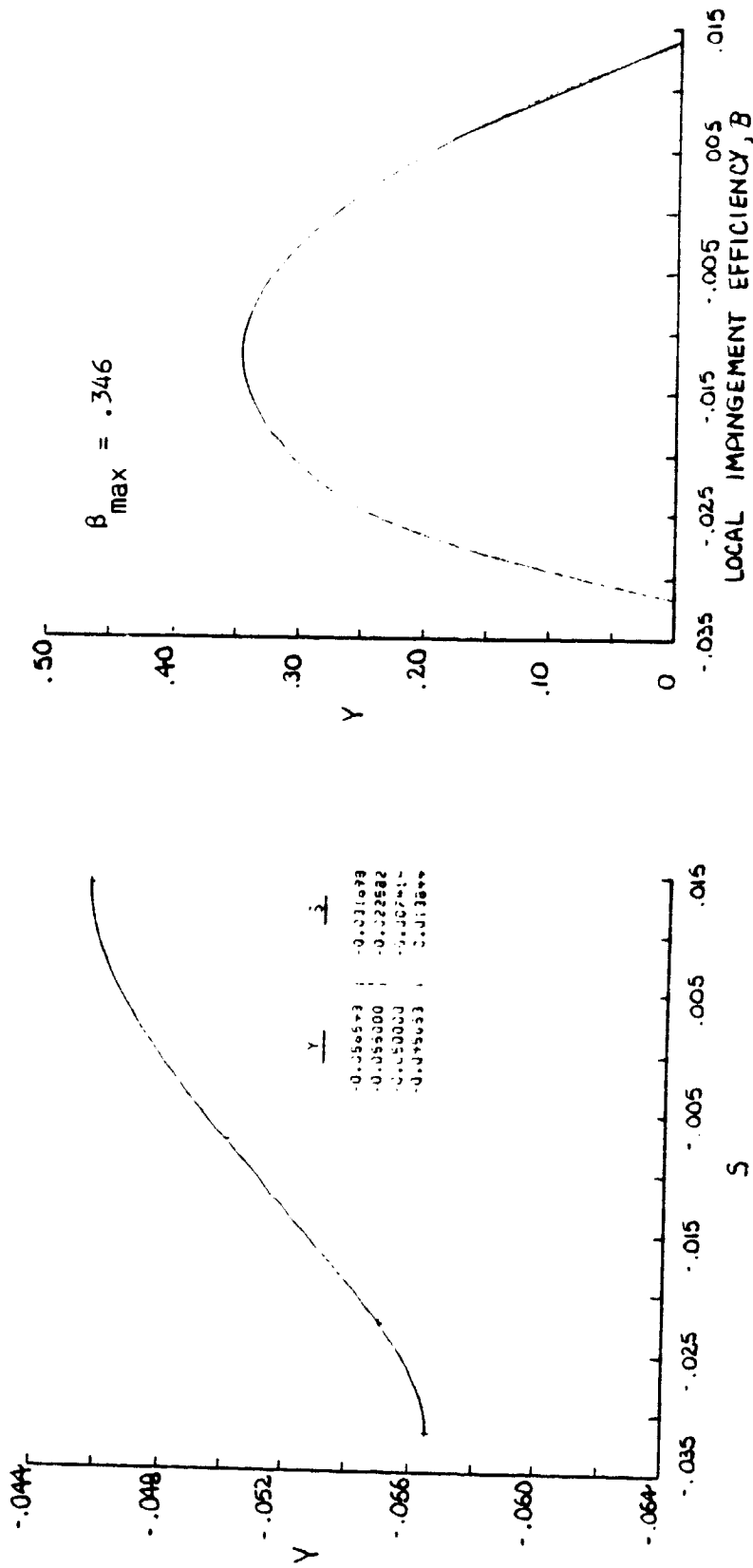
Figure C.2. - (Continued.)

ORIGINAL PAGE IS  
OF POOR QUALITY



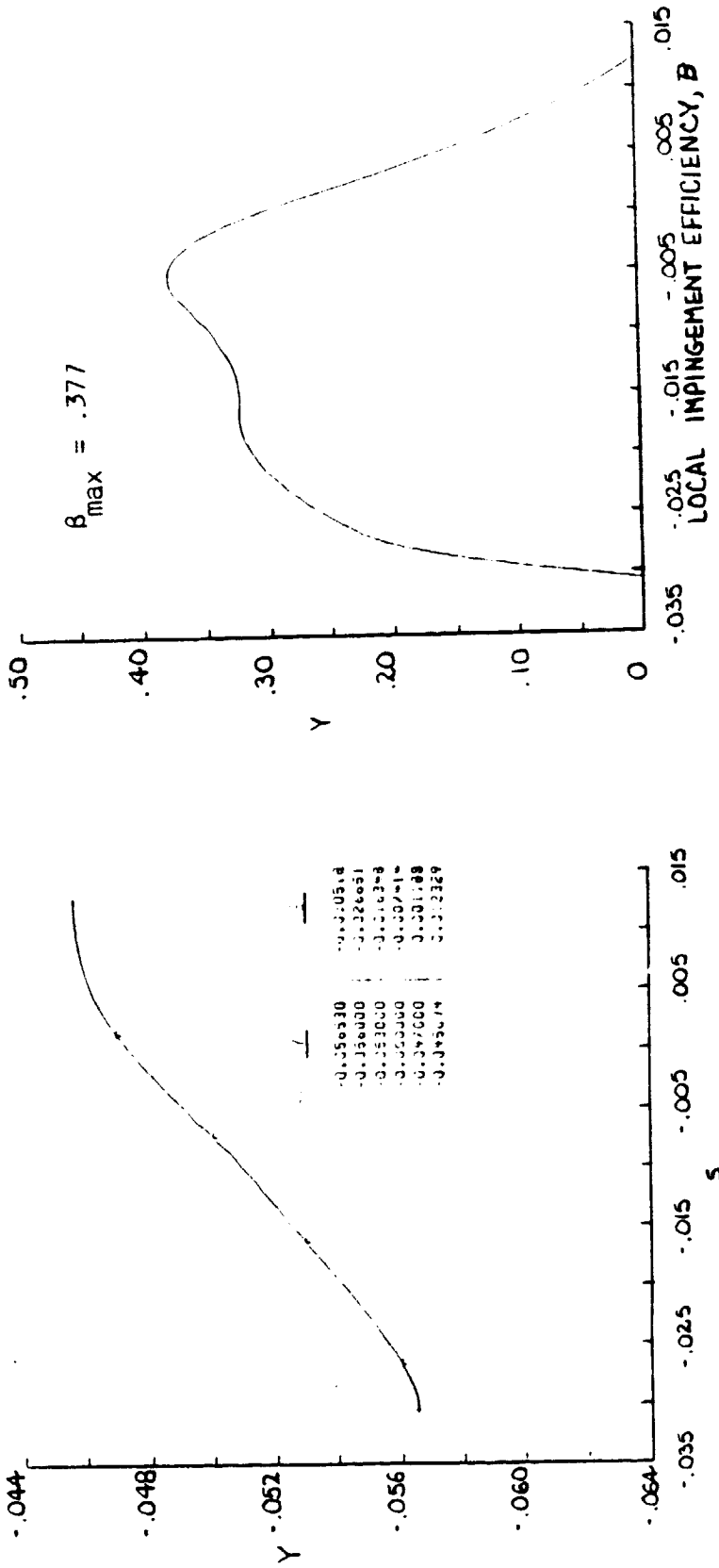
(c) With 8 Trajectories Impacting Airfoil

Figure C.2. - (Continued.)



(a) With 4 Trajectories Impacting Airfoil

Figure C.3. - Local Impingement Efficiency Distributions at  $V = 96$  knots  
 $T = 25^\circ F$ , Angle of Attack =  $2.1^\circ$ , and  $d = 20$  microns.



(b) With 6 Trajectories Impacting Airfoil

Figure C.3. - (Continued.)

Appendix D

Computer Program Listing of Prediction Methods

```
100 REM ADS-4 Prediction of Minimum Required Anti-Ice Flow Rates
110 REM for a Fluid Ice Protection System
120 REM Enter the Following Values
130 PRINT "Wing Chord Length ?";
140 INPUT C
150 PRINT "Liquid Water Content, LWC (g/m3) ?";
160 INPUT LWC
170 PRINT "True Velocity, Vt (Knots) ?";
180 INPUT VKTS
190 PRINT "Datum Temperature, Tok (deg. F) ?";
200 INPUT TDAT
210 PRINT "Overall Water Collection Efficiency, Em ?";
220 INPUT Em
230 PRINT "Which Glycol Solution (1 = AL5 or 2 =TKS80) ?";
240 INPUT FLUID
250 PRINT "Chordwise Impingement Extent, Su - S1 ?";
260 INPUT SUSL
270 PRINT "Airfoil Projected Height, h/c ?";
280 INPUT HC
```

```
290 REM Computation Section
300 Rem Compute Overall Water Catch Rate
310 MW = .379*VTKS*LWC*C*HC*EM/(SUSL - C)
320 IF FLUID = 1 THEN X = 87.8:G = 36.698-.69*TDAT-.014*TDAT*TDAT
330 IF FLUID = 2 THEN X = 81.2:G = 36.565-.67*TDAT-.013*TDAT*TDAT
340 REM Compute Predicted Anti-Ice Fluid Flow
350 SFPE = ((MW*G)/(X - G))*0.00856
360 PRINT "Predicted Anti-Ice Fluid Flow ";SFPE
370 STOP
380 END
```

## Appendix D.2

### Listing of Computer Program in BASIC of Analytical Prediction Method

```
100 REM Analytical Prediction of Minimum Required Anti-Ice
110 REM Flow Rates for a Fluid Ice Protection System
120 REM Enter the following values
130 PRINT "Wing Chord Length, C (ft) ?";
140 INPUT C
150 PRINT "Liquid Water Content, LWC (g/m3) ?";
160 INPUT LWC
170 PRINT "True Velocity, Vt (Knots) ?";
180 INPUT VKTS
190 PRINT "Total Temperature, T (deg. F) ?";
200 INPUT TTOT
210 PRINT "Max. Local Water Collection Efficiency, Bmax ?";
220 INPUT BETAMAX
230 PRINT "Which Glycol Solution (1 = AL5 or 2= TKS80) ?";
240 INPUT FLUID
250 REM Computation Section
260 REM Convert velocity to cm/min
270 VCM = VKTS*3088.84
280 REM Compute local water catch rate
```

```
290 WATER = VCM*LWC*BETAMAX/1003
300 REM Compute Average Temperature
310 TSTAT = TTOT-((VCM/1828.82)2/12020)
320 TAVG = (TSTAT+TTOT)/2
330 IF FLUID = 1 THEN X = 87.8:G = 36.698-.69*TAVG-.014*TAVG*TAVG
340 IF FLUID = 2 THEN X = 81.2:G = 36.565-.67*TAVG-.013*TAVG*TAVG
350 REM Compute Predicted Anti-Ice Fluid Flow
360 SFFA = (WATER*G)(X-G)
370 PRINT "Predicted Fluid Flow = ";SFFA
380 STOP
390 END
```

1. Report No. NASA CR-174758		2. Government Accession No.		3. Recipient's Catalog No.	
4. Title and Subtitle Experimental and Analytical Investigation of a Freezing Point Depressant Fluid Ice Protection System				5. Report Date September 1984	
				6. Performing Organization Code	
7. Author(s) Alan E. Albright				8. Performing Organization Report No. None	
				10. Work Unit No.	
9. Performing Organization Name and Address University of Kansas Dept. of Aerospace Engineering Lawrence, Kansas				11. Contract or Grant No. NAG 3-273	
				13. Type of Report and Period Covered Contractor Report	
12. Sponsoring Agency Name and Address National Aeronautics and Space Administration Washington, D.C. 20546				14. Sponsoring Agency Code 505-45-02	
15. Supplementary Notes Final report. Project Manager, Robert J. Shaw, Propulsion Systems Division, NASA Lewis Research Center, Cleveland, Ohio 44135. This report was submitted as a thesis in partial fulfillment of the requirements for the degree of Master of Engineering to the University of Kansas, Lawrence, Kansas.					
16. Abstract A glycol-exuding porous leading edge ice protection system was tested in the NASA Icing Research Tunnel. Stainless steel mesh, laser drilled titanium, and composite panels were tested on two general aviation wing sections. Two different glycol-water solutions were evaluated. Minimum glycol flow rates required for anti-icing were obtained as a function of angle of attack, liquid water content, volume median drop diameter, temperature, and velocity. Ice accretions formed after five minutes of icing were shed in three minutes or less using a glycol fluid flow equal to the anti-ice flow rate. Two methods of predicting anti-ice flow rates are presented and compared with a large experimental data base of anti-ice flow rates over a wide range of icing conditions. The first method, presented in the ADS-4 document, typically predicts flow rates lower than the experimental flow rates. The second method, originally published in 1983, typically predicts flow rates up to 25 percent higher than the experimental flow rates. This method proved to be more consistent between wing-panel configurations. Significant correlation coefficients between the predicted flow rates and the experimental flow rates ranged from .867 to .947.					
17. Key Words (Suggested by Author(s)) Aircraft icing Ice protection systems Fluid freezing point depressant system Icing wind tunnel tests				18. Distribution Statement Unclassified - unlimited STAR Category 02	
19. Security Classif. (of this report) Unclassified		20. Security Classif. (of this page) Unclassified		21. No. of pages 147	22. Price* A07

**END**

**DATE**

**FILMED**

AUG 22 1986